Neutron diffraction studies of magnetic ordering in superconducting ErNi2B2C and TmNi2B2C in an applied magnetic field

Toft, Katrine Nørgaard

Publication date:
2004

Document Version
Publisher's PDF, also known as Version of record

Risø–R–1440(EN)

Neutron diffraction studies of magnetic ordering in superconducting $ErNi_2B_2C$ and $TmNi_2B_2C$ in an applied magnetic field

Katrine Nørgaard Toft

Risø National Laboratory, Roskilde
Faculty of Science, University of Copenhagen
January 2004

Abstract

This thesis describes neutron diffraction studies of the long-range magnetic ordering of superconducting $ErNi_2B_2C$ and $TmNi_2B_2C$ in an applied magnetic field. The magnetic structures in an applied field are especially interesting because the field suppresses the superconducting order parameter and therefore the magnetic properties can be studied while varying the strength of superconductivity.

$ErNi_2B_2C$:

For magnetic fields along all three symmetry directions, the observed magnetic structures have a period corresponding to the Fermi surface nesting structure. The phase diagrams present all the observed magnetic structures, and the spin configuration of the structures are well understood in the context of the mean field model by Jensen *et al.* [1]. However, two results remain unresolved: 1. When applying the magnetic field along [010], the minority domain ($\mathbf{Q}_{\mathrm{N}}^{\mathrm{B}}= (0, Q, 0)$ with moments perpendicular to the field) shows no signs of hysteresis. I expected it to be a meta stable state which would be gradually suppressed by a magnetic field, and when decreasing the field it would not reappear until some small field comparable to the demagnetization field of 0.1 T. 2. When the field is applied along [110], the magnetic structure rotates a small angle of 0.5^{o} away from the symmetry direction.

$TmNi_2B_2C$:

A magnetic field applied in the [100] direction suppresses the zero field magnetic structure $\mathbf{Q}_{\mathrm{F}} = (0.094, 0.094, 0)$ ($T_{\mathrm{N}} = 1.6$ K), in favor of the Fermi surface nesting structure $\mathbf{Q}_{\mathrm{N}} = (0.483, 0, 0)$. The appearance of the $\mathbf{Q}_{\mathrm{N}}$ phase was initially believed to be caused by the suppression of superconductivity. This suppression should make it energetically favorable to create a magnetic order with a Q-vector determined by the maximum in the magnetic susceptibility at the Fermi surface nesting vector $\mathbf{Q}_{\mathrm{N}}$. The phase diagram for the magnetic structures is presented, however several properties of the $\mathbf{Q}_{\mathrm{N}}$ magnetic structure cannot be explained within any known models. Quadrupolar ordering is suggested as a possible candidate for explaining several features of the $\mathbf{Q}_{\mathrm{N}}$ structure: The Nèel temperature of $\mathbf{Q}_{\mathrm{N}}$ increases steadily up to the maximum examined field of 6 T, the $\mathbf{Q}_{\mathrm{N}}$ structure appears only parallel to the applied field, not perpendicular to it, and last the $\mathbf{Q}_{\mathrm{N}}$ phase has a low intensity tail extending to temperatures as high as 15 K at 6 T.

It should be noted that part of the work for this thesis has been carried out in collaboration with fellow researchers. In general, I have initiated all the neutron diffraction and scattering experiments, and performed most of them myself. Some of them have been performed while I was either pregnant or on maternity leave, by A. B. Abrahamsen, A. Jensen and N. H. Andersen. The results for $ErNi_2B_2C$ with the field along [001] are presented in section 5.5, note that the experiment and data analysis for this field direction is done by A. Jensen. The remaining data analysis presented in chapters 5 and 6 was done by myself. The model work on the magnetic structures, described in sections 2.4, 2.5, and 2.6 was done by J. Jensen [1, 2].

Many of the results presented in this thesis are also included in the following publications:

K. Nørgaard, M.R. Eskildsen, N.H. Andersen, J. Jensen, P. Hedegård, S.N. Klausen, and P.C. Canfield, Interdependence of Magnetism and Superconductivity in the Borocarbide $TmNi_2B_2C$, *Phys. Rev. Lett.* **84**, 4982-4985, 2000.

M.R. Eskildsen, K. Nørgaard, A. B. Abrahamsen, N. H. Andersen, K. Mortensen, P. L. Gammel, D. Lopez, D. J. Bishop, P. Vorderwisch, M. Meissner, and P. C. Canfield, Neutron scattering studies of the flux line lattice and magnetic ordering in $TmNi_2B_2C$, pp. 333-340 in Rare Earth Transition Metal Borocarbides (Nitrides), Kluwer Academic Publishers, 2001.

K. Nørgaard Toft, A. B. Abrahamsen, N. H. Andersen, D. F. McMorrow, A. Jensen, J. Jensen, P. Hedegård, J. Klenke, K. Prokes, P. Smeibidl, S. Danilkin, V. Sikolenko, M. R. Eskildsen, and P. C. Canfield, The Magnetic state of $ErNi_2B_2C$ in an in-plane field, pp. 14-15 in Superconductivity and Magnetism: Materials Properties and Developments, 24th Risø International Symposium on Materials Science 2003.

A. Jensen, K. Nørgaard Toft, A. B. Abrahamsen, D. F. McMorrow, M. R. Eskildsen, N. H. Andersen, J. Jensen, P. Hedegård, J. Klenke, S. Danilkin, K. Prokes, V. Sikolenko, P. Smeibidl, S. L. Budko, and P. C. Canfield, Field-induced magnetic phases in the normal and superconducting states of $ErNi_2B_2C$. *Accepted for publication in Phys. Rev. B.* Present version attached to this thesis.

K. Nørgaard Toft, A. B. Abrahamsen, M. R. Eskildsen, K. Lefmann, N. H. Andersen, P. Vorderwisch, P. Smeibidl, M. Meissner, and P. C. Canfield, A Neutron Diffraction Study of the Anomalous High Field Magnetic Phases in $TmNi_2B_2C$, *Submitted to Phys. Rev. B.* Present version attached to this thesis.

This thesis is submitted in partial fulfilment of the requirements for a ph.d. degree at the University of Copenhagen. The work has been carried out at Risø National Laboratory in the Condensed Matter Physics and Chemistry Department and in the Materials Research Department. The supervisors were Niels Hessel Andersen, Risø and Jens Jensen, University of Copenhagen.

ISBN 87–550–3286–9; 87–550–3287–7 (Internet)
ISSN 0106–2840

Print: Pitney Bowes Management Services Denmark A/S · 2004

Contents

1 Introduction

Superconductivity and long range magnetic order are two basic properties of solid state materials which have been studied intensively for many years. Magnetism is by now well understood and the basic mechanisms have been unravelled throughout the last forty years. Superconductivity on the other hand, is not yet well understood. Some of the basic features were explained in the fifties by Ginzburg and Landau, and by Bardeen, Cooper and Schrieffer, but the basic mechanism of the High-T_c materials is a mystery yet to be solved. One question that needs answering is whether the attractive coupling in the Cooper pairs is magnetic in origin. Thus, the interaction between superconductivity and magnetism is studied not only because they are competing states, but also because it may resolve a fundamental problem in superconductivity physics.

In this thesis the magnetic structures of $ErNi_2B_2C$ and $TmNi_2B_2C$ are studied in an applied magnetic field. The idea of the experiments was to study the magnetic structures while suppressing superconductivity, and this was done by applying a magnetic field. The magnetic field modifies the superconducting order parameter, which means that in principle we can study the magnetic order while gradually changing the strength of superconductivity.

The problem at hand is that the magnetic field also affects the magnetic structures directly, and the hard part of this thesis has been to separate whether it was a reduced strength of superconductivity or an effect of the magnetic field applied, which was the driving factor for the observed changes of magnetic structure.

This chapter introduces the problem at hand, and gives an overview of the history of the interaction between superconductivity and magnetism. Chapter 2 presents the basic theoretical mechanisms for the magnetic ordering in the rare earth nickel borocarbides, and specifically the model work on $ErNi_2B_2C$. Chapter 3 contains a short presentation of the superconducting properties relevant for this thesis. Chapter 4 gives a detailed treatment of neutron diffraction of magnetic structures. Chapters 5 and 6 contain the experimental results, and finally chapter 7 summarizes the results, and offers an outlook to future experiments. Appendix A accounts for the detailed calculation of the scaling of the $\mathbf{Q}_F$ intensity to $\mathbf{Q}_N$ equivalents, which is used in chapter 6.

1.1 Superconductivity and magnetism - historically

In the 1950s and 1960s, the interaction between magnetism and superconductivity was studied by substituting magnetic impurities into a superconductor, with a fast suppression of superconductivity as a result [3]. This was understood in terms of the spin scattering of the impurity spins which disrupts the Cooper pair formation [4]. Typically, a 1 % substitution was enough to extinguish the superconducting state. Such a low concentration of magnetic ions means that a cooperative magnetic state does not form, a state which would otherwise compete with the superconducting order parameter.

The 1970s offered the first examples of true long range magnetic order coexisting with superconductivity, namely the Chevrel phase superconductors with chemical formula RMo_6S_8, and the related RRh_4B_4 compounds. In these materials there is a separate, fully occupied rare earth sublattice. The fact that these materials were

superconducting at all implied that the magnetic ions and the superconducting electrons belonged to different, isolated sublattices, and thereby the conventional Abrikosov-Gorkov spin-depairing mechanism was suppressed. The magnetic ordering temperatures are all low, approximately 1 K, and thus it was argued that electromagnetic dipolar interactions dominates the energetics of the magnetic system. In cases where these interactions favor antiferromagnetism, the magnetization averages to zero on the length scale of the coherence length, resulting in a weak influence on the superconducting order parameter. In the interesting case of a ferromagnetic state like e.g. $HoMo_6Se_8$[5], there is a strong coupling to the superconducting state that originates from the internally generated magnetic field. The competition with the superconducting order parameter gives rise to long wavelength oscillatory magnetic states and/or reentrant superconductivity.

In the late 1980s all attention was given to the high-T_c cuprate compounds, where interesting aspects of the interaction between superconductivity and magnetism were presented. Interestingly, there is magnetism associated with the Cu ions, while the Cu-O layers are also responsible for the superconducting pairing. The undoped cuprates are antiferromagnetic insulators where the $S = \frac{1}{2}$ Cu spins order at high temperatures. With doping, the materials loose the Cu long range magnetic order and become high-T_c superconductors. The Cu moments and energetics are still present, though, and these quantum spin fluctuations are believed to play an essential role in the formation of the d-wave electron pairing.

The rare earth nickel borocarbides were discovered in 1994, with long range magnetic ordering occurring at relatively high temperatures ($\approx$ 10 K), thereby ensuring that exchange interactions control the magnetic system. Also the superconducting ordering temperatures are in the range of 10 K, with a strong electron-phonon interaction. The combined magnetic and superconducting properties, with comparable energy scales make these materials model systems for investigating the interaction between these two cooperative phenomena.

2 Magnetism

The rare earth nickel borocarbides, with the chemical stoichiometry RNi_2B_2C, belong to the quaternary intermetallic superconductors. Superconductivity in a number of these materials was first reported in 1994 by Nagarajan *et al.* [6] and Cava *et al.* [7]. The crystal structure, which is shown in figure 1 was determined by Siegrist *et al.* [8], and is body centered tetragonal (symmetry group I4/*mmm*).

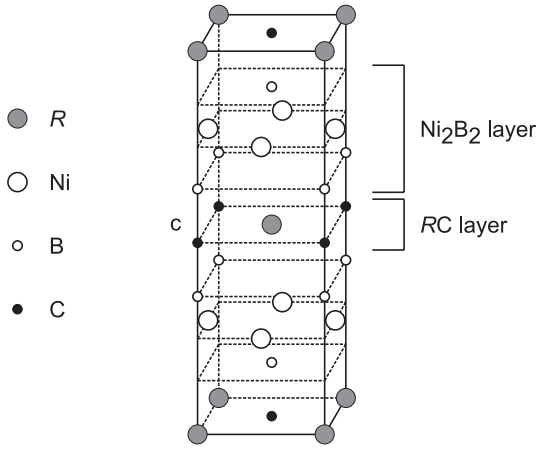

Figure 1. Crystal structure of RNi_2B_2C, the crystalline parameters varies slightly through the series from a = 3.637 Å in $GdNi_2B_2C$ to a = 3.478 Å in $YbNi_2B_2C$, and c = 10.227 Å in $GdNi_2B_2C$ increasing to c = 10.607 Å in $YbNi_2B_2C$.

The magnetism in these materials arises from ordering of the magnetic moment on the rare earth ion. A Hamiltonian describing the magnetism consists of terms including the crystalline electric field, dipole and exchange couplings. Also magnetoelastic and quadrupolar terms are relevant for $ErNi_2B_2C$. On the other hand for $TmNi_2B_2C$, no specific model has been presented in the literature. We discuss the above mentioned terms in the model for $ErNi_2B_2C$, and also the basic theory for a quadrupolar/magnetoelastic coupling. This may be relevant in $TmNi_2B_2C$.

2.1 Hund´s rules

The electron configuration of a single rare earth atom follows the general scheme of the rare earth atoms. It is characterized by the filling of the $4f$ shell with 0 to 14 electrons, and the configuration of an individual atom can be calculated by means of local density theory. As a result, it is seen that the $4f$ electrons are close to the nuclei, well shielded by the $5d$ and $6s$ electrons [9].
The spin and orbital angular momenta of the ion are determined by Hund´s rules:

1. Maximize S.
   This minimizes the energy contribution due to the exchange interaction by letting the spins point in the same direction.

2. Maximize L within the constrains of rule 1.
   This minimizes the energy contribution from the Coulomb interaction between the electrons, since the electrons tend in average to be further away from each other if they rotate in the same direction.

3. $J = |L \mp S|$ with the sign changing at half filling.
   This minimizes the energy contribution from the spin-orbit coupling. The sign change appears because for a single electron the energy is lowest when

the spin is antiparallel to the orbital angular momentum, whereas for a more than half filled shell the low energy states are used up, and by the exclusion principle, the lowest energy is obtained if the spin is parallel to the orbit.

A free Er^{3+} ion has 11 $4f$ electrons, hence using Hund's rules gives $S = \frac{3}{2}$, $L = 6$, and $J = \frac{15}{2}$. Tm^{3+} has 12 $4f$ electrons giving $S = 1$, $L = 5$, and $J = 6$.

The magnetic moment is given by

$$\boldsymbol{\mu} = g_{\mathrm{S}}\mu_{\mathrm{B}}\mathbf{S} + g_{\mathrm{L}}\mu_{\mathrm{B}}\mathbf{L} \tag{1}$$

where $g_{\mathrm{S}} = 2$ and $g_{\mathrm{L}} = 1$ are the gyromagnetic factors for the spin and orbital angular momentum. Inserting this gives:

$$\boldsymbol{\mu} = \mu_{\mathrm{B}}(2\mathbf{S} + \mathbf{L}) = \mu_{\mathrm{B}}(\mathbf{S} + \mathbf{J}) \tag{2}$$

The magnetic moment precesses around $\mathbf{J}$, and only the projection of the magnetic moment on $\mathbf{J}$ is conserved. The component of $\mathbf{S}$ parallel to $\mathbf{J}$ is:

$$\mathbf{S}_{\parallel} = \frac{\mathbf{J}\cdot\mathbf{S}}{\mathbf{J}^2}\mathbf{J} = \frac{1}{2}\frac{\mathbf{J}^2 + \mathbf{S}^2 - \mathbf{L}^2}{\mathbf{J}^2}\mathbf{J} \tag{3}$$

Inserting this, the magnetic moment is:

$$\boldsymbol{\mu} = -\mu_{\mathrm{B}}(\mathbf{S}_{\parallel} + \mathbf{J}) = -g_{\mathrm{J}}\mu_{\mathrm{B}}\mathbf{J} \tag{4}$$

where

$$g_{\mathrm{J}} = 1 + \frac{J(J+1) + S(S+1) - L(L+1)}{2J(J+1)} \tag{5}$$

is the Landé g-value. For a free Er ion we obtain a g_{J} value of $\frac{6}{5}$, resulting in a magnetic moment of $9\mu_{\mathrm{B}}$, and similarly for Tm^{3+} $g_{\mathrm{J}} = \frac{7}{6}$ and the magnetic moment is $7\mu_{\mathrm{B}}$.

2.2 Crystal electric field

The magnetism of the rare earth ions is due to the unfilled $4f$ shell, whose electrons are close to the core. The consequence is a spin-orbit coupling so strong that even if the electrons are perturbed by a crystal field, the ground state of the ion is found among those picked by the spin-orbit coupling. The exact configuration of the lowest lying rare earth states are controlled by the crystal electric field, and will be summarized in the following. The symmetry of the rare earth nickel borocarbides leads to a Hamiltonian for the crystalline electric field defined in terms of five parameters:

$$\mathcal{H}_{CF} = \sum_{l=2,4,6} B_l^0 O_l^0 + \sum_{l=4,6} B_l^4 O_l^4, \tag{6}$$

where O_l^m are the Stevens operators [9]. The Stevens parameters B_l^m may be determined from inelastic neutronscattering [10], in combination with paramagnetic susceptibility and heat capacity measurements. This was done by Gasser *et al.* [10], and the results for $ErNi_2B_2C$ and $TmNi_2B_2C$ are presented in table 1.

In the case with $TmNi_2B_2C$, the crystal field creates a doublet ground state with only J_z components, the next states appear approximately 3 meV above and they are nearly degenerate. Notice that 3 meV corresponds to 33 K so the magnetic properties with $T_{\mathrm{N}} = 1.6$ K are determined by the doublet ground state yielding an Ising-like system with the c-axis being the easy axis. The observed magnetic

	B_2^0	B_4^0	B_4^4	B_6^0	B_6^4
$ErNi_2B_2C$	-0.0173	$0.147 \cdot 10^{-3}$	$-3.3 \cdot 10^{-3}$	$-0.122 \cdot 10^{-5}$	$2.16 \cdot 10^{-5}$
$TmNi_2B_2C$	-0.12	$0.33 \cdot 10^{-3}$	-0.01	$0.7 \cdot 10^{-5}$	$-1.16 \cdot 10^{-4}$

Table 1. The Stevens operator parameters (meV). From references [1, 10].

moment of the Tm ion in $TmNi_2B_2C$ is $4\mu_B$, compared to the free ion moment of $7\mu_B$.

The ground state of the Er^{3+} ion in $ErNi_2B_2C$ is a doublet, with an exited doublet lying only 0.6-0.7 meV above the ground state. This leads to a 'double-Ising' system, the so-called four-state clock behavior. The moments are hard to magnetize along the *c*-direction, but they are easily magnetized along the [100] or equivalently the [010] directions, and when the field is applied in the *ab*-plane, the magnetization measurements show a $\cos\theta$ dependence [11]. The observed magnetic moment of the Er ion in $ErNi_2B_2C$ is $7.8\mu_B$, compared to the free ion moment of $9\mu_B$, and magnetic ordering appears at $T_N = 6.8$ K.

2.3 Heisenberg exchange coupling

The exchange interaction between the conduction electrons and the localized $4f$ electrons leads to an indirect coupling between the spins of the rare earth ions. It is therefore the susceptibility of the electron gas and the overlap between the $4f$ and the conduction electrons that determine the nature of this coupling.

The effective Heisenberg interaction between the spins of the rare earth ions is given by:

$$\mathcal{H}_{\mathrm{RKKY}} = -\mathcal{J} \sum_{i,j} \chi(\mathrm{R}_i - \mathrm{R}_j)\, \mathrm{S}_i \cdot \mathrm{S}_i \tag{7}$$

here $\mathcal{J}$ is the constant value of the exchange integral, $\mathcal{J}(\mathbf{q})$, which represents the overlap between the $4f$ electrons and the conduction electrons. Experimentally this is known as the form factor of the $4f$ electrons. Since the $4f$ electrons are close to the ion core, the electron density may be approximated by a delta function, yielding a constant exchange integral, $\mathcal{J}$. $\chi(\mathrm{R}_i - \mathrm{R}_j)$ is the susceptibility of the conduction electrons. Only the projection of the spin on the total angular moment J is conserved, and the Landé g-value may be used, as in equations (3) and (5), and $\mathbf{S}_\parallel = (g_J - 1)\mathbf{J}$. In reciprocal space the RKKY interaction may now be written as:

$$\mathcal{H}_{\mathrm{RKKY}} = -\mathcal{J} \sum_{\mathbf{Q}} \chi(\mathbf{Q})\, \mathrm{J}_{\mathbf{Q}} \cdot \mathrm{J}_{-\mathbf{Q}} \tag{8}$$

where the factor $(g_J - 1)$ is hidden in the prefactor $\mathcal{J}$. The susceptibility is given by

$$\chi(\mathbf{Q}) = \frac{1}{N} \sum_{\mathbf{k}} \frac{f_{k-Q} - f_k}{\epsilon_k - \epsilon_{k-Q}} \tag{9}$$

where $f_k = 1/(e^{\beta(\epsilon_k - \mu)})$ is the Fermi-Dirac distribution function which gives the average occupation of the electron state with energy ϵ_k. In general it is the maximum of the product $\chi(\mathbf{Q})\mathcal{J}(\mathbf{Q})$, which determines the magnetic structure, but

often the variation of $\mathcal{J}(\mathbf{Q})$ is slow compared to that of $\chi(\mathbf{Q})$, and in the following section the susceptibility will be discussed.

Susceptibility and superconductivity

Figure 2 presents a schematic representation of the Q dependence of the conduction-electron susceptibility for the normal and superconducting state, calculated by Ramakrishnan and Varma in 1981 [12]. In the top panel the susceptibility is calculated for a metal with a spherical Fermi surface, and in the bottom panel for a metal with a Fermi surface with nesting near $Q = G$.

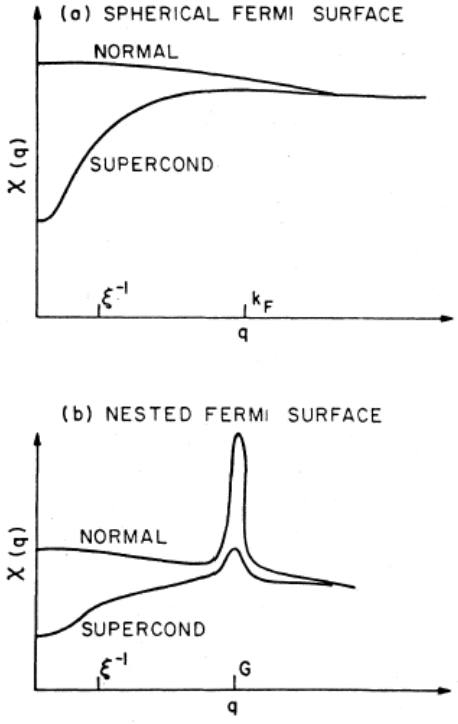

Figure 2. The susceptibility of the conduction electrons in a normal and superconducting phase, for a spherical Fermi surface (top panel) and a nested Fermi surface with nesting vector $\mathbf{Q} = \mathbf{G}$. *From reference [12].*

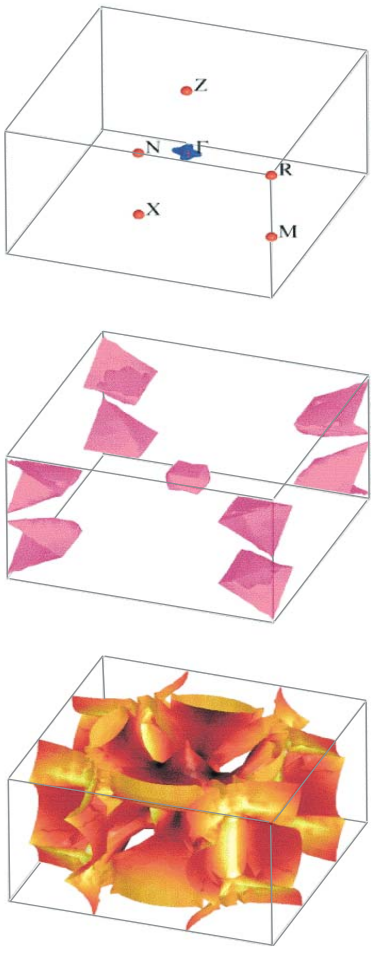

Figure 3. The three sheets of the FS of $LuNi_2B_2C$, *shown within the simple tetragonal BZ, with its usual symmetry points labelled. The use of color is simply to increase clarity. From reference [13].*

The susceptibility of the normal metallic phase is proportional to the Lindhard function, which has a maximum for $Q = 0$ giving a ferromagnetic ground state. In the superconducting phase the conduction electrons are bound in Cooper pairs,

consisting of a spin up and a spin down electron. The Cooper pairs are coherent only for small distances, typically the coherence length in the RNi_2B_2C is approximately 100 Å, and therefore the mediation of the RKKY interaction is cut-off for distances larger than the coherence length. In reciprocal space this yields a cut-off in the susceptibility for $Q < 1/\xi$, which can be seen in the top panel of figure 2. For finite temperatures excited quasi particles emerge, which are able to mediate the RKKY interaction over larger distances, and gradually the normal state susceptibility is obtained at $T = T_c$. As early as in 1959 Anderson and Suhl examined the case of superconductivity introduced in a ferromagnetic state, and they found that the appearance of a minimum at $Q = 0$ creates a maximum in the susceptibility for some small wave vector $Q \propto 1/\xi$, the so-called crypto-ferromagnetic state [14].

The bottom panel of figure 2 presents the susceptibility of the conduction electrons in a normal and superconducting phase in the case of a nested Fermi surface. Fermi surface nesting can be understood if we consider the susceptibility in equation (9). The largest terms in the sum will be terms with a small energy difference between the states k and $k - Q$. Scattering from one of the states to the other requires that one state is occupied and the other is empty. This means that the electrons at the Fermi surface contributes significantly to the susceptibility, because here we can find states which are close in energy and where it is likely that one is empty and the other is occupied. If there exists parallel regions separated by some vector $\mathbf{G}$ of the Fermi surface with high density of states, there will be many states fulfilling the above mentioned condition, and a maximum will appear in the susceptibility at this nesting vector.

Notice in figure 3 that the nesting wave vector is suppressed in the superconducting state, due to the joint density of states with the magnetic phase [12].

Fermi surface nesting in RNi_2B_2C

The generalized susceptibility of the RNi_2B_2C was first calculated by Rhee and co-workers, using the energy band structure for $LuNi_2B_2C$. They found a maximum for $\mathbf{Q} \approx (0.6, 0, 0)$, and this was later confirmed by Dugdale *et al.* in electron-positron annihilation measurements of the Fermi surface topology [13]. They found a nesting feature with $\mathbf{Q} \approx (0.6, 0, 0)$, as shown in figures 3 and 4 . The identification of a nesting feature cannot be done by looking at parallel regions of the Fermi surface topology alone, only regions of high density of states are able to create a true nesting feature.

The importance of this nesting wavevector is realized when considering that magnetic ordering with a wave vector $\mathbf{Q} \approx (0.55,0,0)$ has been observed in the RNi_2B_2C compounds with R = Gd,

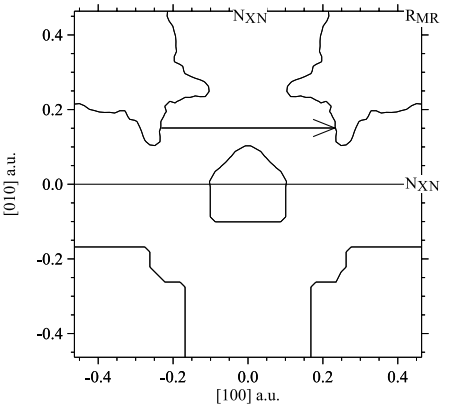

Figure 4. The experimental (upper half) and calculated (lower half) FS topology of $LuNi_2B_2C$. The calculation is of the FS in the third band in the (001) plane through the Γ point. The arrow indicates the nesting feature. From reference [13].

Tb, Ho, and Er in zero applied magnetic field [15, 16, 17, 18, 19], and for R = Tm, Ho and possibly Dy in a finite applied field [20, 21, 22].

2.4 Quadrupolar coupling

In an attempt to understand the strange features of the magnetic structure in $TmNi_2B_2C$ which are presented in chapter 6, the idea of possible quadrupolar ordering may be considered, but also in $ErNi_2B_2C$ a small quadrupolar term is included in the model.

The terms in the Hamiltonian describing the magnetoelastic and quadrupolar coupling in tetragonal $TmNi_2B_2C$ may be written as [2]:

$$\begin{aligned}\mathcal{H}_Q = & - \frac{1}{2}\sum_{ij}\left[K_1(ij)O_2^1(i)O_2^1(j) + K_2(ij)O_2^{-1}(i)O_2^{-1}(j)\right] \\ & - \sum_i B_{13}\left[\epsilon_{13}(i)O_2^1(i) + \epsilon_{23}(i)O_2^{-1}(i)\right] \\ & + \frac{1}{2}\sum_{\mathbf{Q}} c_{13}(\mathbf{Q})\left[\epsilon_{13}^2(\mathbf{Q}) + \epsilon_{23}^2(\mathbf{Q})\right] \end{aligned} \quad (10)$$

where the first line is the ion-ion quadrupolar coupling with O_2^1 defined as $O_2^1 = \frac{1}{2}(J_xJ_z + J_zJ_x)$, and O_2^{-1} is defined in a similar way with x replaced by y, notice $K_1 = K_2$ because the crystal is tetragonal. The second line describes the coupling between the quadrupolar moments and the strain, $\epsilon_{13}(\mathbf{Q})$ is the generalized strain, with $\mathbf{Q}$ along the first axis (x) and the translation along the third axis (z). The third line represents the strain energy, and c_{13} is the elastic force constant.

Any distribution of charges can be written as a multipole sum, and if the charge distribution has a symmetry lower than dipolar, then quadrupolar terms may appear. Since the exact distribution of charges in the crystal is highly dependent on the crystal symmetry, it is not surprising that strain may create an electrical field which can give rise to an effective quadrupolar term.

$\mathcal{H}_Q$ may give rise to an effective quadrupolar coupling. Therefore, we may consider in $TmNi_2B_2C$ a pure quadrupolar coupling induced by the magnetic field, or a pure magnetoelastic strain described by a wavevector $\mathbf{Q}_N$ with a displacement of the Tm ions in the c direction, or a combination of both.

In the $LuNi_2B_2C$ and YNi_2B_2C systems a phonon mode has been observed at $\mathbf{Q}_N = (0.55, 0, 0)$ which is softened at T_c. The mode corresponds to a transversal translation of the Tm moments in the c direction. Since this phonon mode obviously couples to superconductivity it is possible that it also exists in $TmNi_2B_2C$. In that case a softening of this mode would stabilize a quadrupolar like phase. The existence of this phonon mode should be examined both in zero and in an applied field, and in elastic and in-elastic modes, since it may or may not be static.

Some properties of the magnetic phase in $TmNi_2B_2C$ (for details see chapter 6) have so far been considered to be strange features, which we could not explain, like the steadily increasing T_N and fact that the magnetic structure appears only parallel and not perpendicular to the magnetic field. These features may be explained if a quadrupolar coupling is present either in zero or non-zero field, which I will explain in the following.

Firstly, we need to consider whether a magnetic field applied along the a axis can induce a c axis moment modulated with a period along the field direction. If we have a quadrupolar ordered phase, then we can write:

$$\langle O_2^1(i)\rangle = \langle O_2^1(\mathbf{Q}_\mathrm{N})\rangle \cos(\mathbf{Q}_\mathrm{N}\cdot\mathbf{R}_i). \tag{11}$$

Applying a magnetic field corresponds to $\langle J_x(i)\rangle$ being a constant different from zero, and since

$$\langle O_2^1(i)\rangle \approx \langle J_x(i)\rangle\langle J_z(i)\rangle = const\cdot\langle J_z(i)\rangle \tag{12}$$

then combining equations (11) and (12) we get that $\langle J_z(i)\rangle$ is different from zero and modulated by $\cos(\mathbf{Q}_\mathrm{N}\cdot\mathbf{R}_i)$. In this way, the quadrupolar ordering may induce a $\mathbf{Q}_\mathrm{N}$ magnetic structure. The size of the modulation of $\langle J_z(i)\rangle$ is proportional to the applied field, which will explain the continuously rising T_N of the $\mathbf{Q}_\mathrm{N}$ structure in increasing fields.

Secondly, the observed asymmetry of the $\mathbf{Q}_\mathrm{N}$ structure, giving rise to scattering in the field direction, but not perpendicular to it, is understood within the idea of quadrupole ordering. When the field is applied along the a axis, the O_2^1 term will be proportional to $\langle J_x\rangle J_z$, and therefore contribute directly to the effective exchange coupling at $\mathbf{Q}_\mathrm{N}$. On the other hand the O_2^{-1} will only be affected to higher order. In this way, the quadrupolar term will stabilize the magnetic domain with a wavevector parallel to the applied field.

2.5 Mean field model of the magnetic states in $ErNi_2B_2C$

The magnetic structures of $ErNi_2B_2C$ emerge in a competition between the crystal electric field, the dipole coupling, and the exchange interaction. The crystalline electric field favors commensurate structures, and it aligns the magnetic moments along an easy axis of magnetization, and the dipole coupling favors transversely polarized structures. In contrast, the exchange interaction prefers incommensurate long wavelength structures. Reference [1] presents a mean-field model of the magnetic structures in $ErNi_2B_2C$ in zero field, and the field behavior will be presented in reference [23]. The basic principles behind the model are described in the following.

The mean field theory is used to calculate the free energies of different magnetic structures by an iteration procedure, and the more stable states are identified by finding the lowest energy states. The three most important contributions to the free energy are the crystal electric field (section 2.2), the exchange interaction (section 2.3) and from the classical dipole-dipole interaction. The magnetic field applied introduces a Zeeman term, and a small magneto-elastic term due to an orthorhombic distortion of the lattice is also included [24].

The exchange and dipole terms are combined in a single two-ion coupling. In these materials the dipole coupling is of the same order of magnitude as the exchange coupling. Furthermore, it is extremely long-range and anisotropic and may therefore have important consequences for the magnetic properties. Since all the structures are described by a wave vector $\mathbf{Q}$ along the a axis and consist of ferromagnetic sheets perpendicular to $\mathbf{Q}$, only the total couplings between the different ferromagnetic layers are important in the model, and the coupling may be split into components parallel, $\mathcal{J}_\parallel(\mathbf{Q})$, and perpendicular, $\mathcal{J}_\perp(\mathbf{Q})$, to $\mathbf{Q}$ within the ab plane. The Hamiltonian may be written as:

$$\mathcal{H} = -\frac{1}{2}\sum_{\mathbf{Q}} \mathcal{J}_{\perp\mathbf{Q}}\,\mathbf{J}_{\perp\mathbf{Q}}\cdot\mathbf{J}_{\perp-\mathbf{Q}} \; -\frac{1}{2}\sum_{\mathbf{Q}} \mathcal{J}_{\parallel\mathbf{Q}}\,\mathbf{J}_{\parallel\mathbf{Q}}\cdot\mathbf{J}_{\parallel-\mathbf{Q}} \tag{13}$$

n	0	1	2	3	4	5	6	9	LD
$\mathcal{J}_\perp(n)$	5.847	-3.816	-4.786	-0.650	1.500	-1.500		0.29	0.29
$\mathcal{J}_\parallel(n) - \mathcal{J}_\perp(n)$	-14.286	-3.024	3.106	-0.630	0.250	-0.084	0.03		

Table 2. The planar two-ion coupling parameters (μeV) from reference [1].

where $\mathbf{J}_{\perp,\parallel\mathbf{Q}}$ are the components of $\mathbf{J}_\mathbf{Q}$ perpendicular and parallel to $\mathbf{Q}$.

The interplanar coupling parameters in direct space are given by:

$$\mathcal{J}_{\parallel,\perp}(n) = \sum_{\mathbf{r}_j\cdot\mathbf{a}=na^2/2} [\mathcal{J}(0j) + \mathcal{J}_D D_{\parallel,\perp}(0j)] \tag{14}$$

where $\mathcal{J}(0j)$ is the direct coupling between the ferromagnetic layers with numbers 0 and j, $\mathcal{J}_D = 1.194$ μeV is the coupling strength of the dipole coupling, and $D_{\parallel,\perp}(0j)$ is the parallel and perpendicular parts of the dipole interaction, given by:

$$D_{\alpha\beta}(ij) = \frac{3(r_{i\alpha} - r_{j\alpha})(r_{i\beta} - r_{j\beta}) - |\mathbf{r}_i - \mathbf{r}_j|^2\delta_{\alpha\beta}}{N|\mathbf{r}_i - \mathbf{r}_j|^5} \tag{15}$$

The transverse interplanar coupling parameters in real space, $\mathcal{J}_\perp(n)$, may be derived by fitting to the experiments of the magnetic structure in zero field [25]. These values are fitted individually for $n = 0, 1, 2, ..., 5$ and 9. The nesting feature known to lie around $Q \approx 0.6$ is introduced by a long-distance coupling parameter modulated by the period of the nesting vector:

$$\mathcal{J}_\perp(n) = \mathcal{J}_\perp(\mathrm{LD})\cos(0.558n\pi) \qquad n = 10, 11, ..., 16. \tag{16}$$

where $Q \approx 0.558$ is chosen on the basis of the experiments by Choi and co-workers [25].

The dipole interaction can be calculated directly for both directions, and since the exchange interaction can be assumed to be isotropic within the *ab* plane, the two-ion coupling $\mathcal{J}_\parallel(n)$ can be calculated from the values of $\mathcal{J}_\perp(n)$.

The final real space values of the coupling parameters are given in Table 2. In order to visualize the meaning of the interplanar coupling parameters, the parameters in reciprocal space can be obtained by a Fourier transform of the values in table 2, and the result is presented in figure 5 taken from reference [1]. Notice that the contribution to the dipole sum from the surface of the sample results in a jump from $\mathcal{J}_\parallel(0) = -12\mu$eV to $\mathcal{J}_0(\mathbf{Q}) = -27\mu$eV. $\mathcal{J}_\perp(n)$ has a maximum for $Q = 0.558$ and there is a large difference between the size of $\mathcal{J}_\perp(n)$ and $\mathcal{J}_\parallel(n)$. The result is an antiferromagnetic structure with a transverse polarization of the moments and $Q = 0.558$.

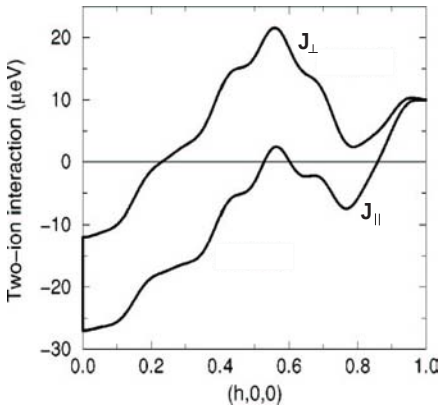

Figure 5. The parallel ($\mathcal{J}_\parallel(\mathbf{Q})$) and perpendicular ($\mathcal{J}_\perp(\mathbf{Q})$) components of the Fourier transform of the two-ion coupling in $ErNi_2B_2C$ along [100] *from reference [1]. The coupling is assumed to comprise an isotropic indirect-exchange contribution and the classical dipole-diploe interaction, which gives rise to the discontinuity at $Q = 0$, where the value of $\mathcal{J}_\parallel(0)$ jumps by 15 μeV.*

The model uses these parameters to calculate the energy of various magnetic structures in increasing magnetic fields, and in the following section these microscopic structures are presented.

2.6 Magnetic structures in $ErNi_2B_2C$

All the calculated structures are based on commensurable structures derived from the basic structure with $Q = \frac{1}{2}$. The moments are pointing either parallel (u) or antiparallel (d) to the b axis, and $\mathbf{Q} \parallel \mathbf{a}$. In the $Q = \frac{1}{2}$ structure the ferromagnetic layers perpendicular to the a axis are polarized subsequently $uudduudd$ along the a direction. Structures with larger values of Q are derived from this structure by a periodic replacement of one or more of the $uu(dd)$ double layers with a single $u(d)$ layer. In an experiment, it is observed that the period of the zero field structure changes slightly when decreasing temperature from 5 K to 3 K [25]. Theoretically this is understood in the following way: close to T_N only the first harmonic is present, and the structure is determined by the maximum in the susceptibility, whereas at lower temperatures the higher order odd harmonics appear and contribute to the calculated energy of the structure, which produces a shift of the ordering wave vector to a smaller value. The mean field model predicts that the zero field structures are:

$$d(4p)u(5p)u(4p)d(5p), \qquad \text{for } T > 2.3\text{K} \tag{17}$$

$$d(3p)d(5p)d(5p)d(5p), \qquad \text{for } T < 2.3\text{K} \tag{18}$$

where d(4p) is short for one spin down, and four pairs of up and down spins: $duudduudd$. Both structures have $Q = \frac{11}{20} = 0.550$. The high temperature structure has no net moment, whereas the low temperature structure has a total moment of $\frac{1}{10}$ spin up pr. Er ion. With a moment size of 7.9 μ_B this yields a net moment of 0.79 μ_B per Er ion. In reality not all moments have their full length, and the observed moment increases from 0.33 μ_B per Er at 2 K to 0.57 μ_B per Er 1.3 K. Other important zero field structures, which may blend with the $Q = \frac{11}{20}$ structure and the combination of which may vary from one sample to another, are:

$$d(4p)u(4p), \qquad \text{for } Q = \frac{5}{9} = 0.555 \tag{19}$$

$$d(3p)d(5p)d(5p), \qquad \text{for } Q = \frac{16}{29} = 0.552 \tag{20}$$

$$d(3p)d(5p)d(5p)d(5p)d(5p), \qquad \text{for } Q = \frac{28}{51} = 0.549 \tag{21}$$

The application of a magnetic field in $ErNi_2B_2C$ will stabilize structures with moments along the field direction, because the strong easy-axis anisotropy makes it more favorable to lengthen and shorten the moments than to rotate them. As the field is increased, the ferromagnetic component will tend to increase. At low temperatures, where the moments are nearly saturated, this may be accomplished by replacing some of the $d(5p)$ sequences with a $d(3p)$ sequence. The magnetic structure is going to consist of a combination of $d(3p)$ and $d(5p)$ sequences with an increasing content of $d(3p)$, until a transition to a pure $d(3p)$ structure is realized. The $d(3p)$ structure has a period of $\frac{4}{7} = 0.572$ and a net moment of $1u$ per 7 Er atoms. A further increase of the field introduces combinations of $d(3p)$ and $d(1p)$. A relevant example is the structure $d(1p)d(3p)d(3p)$ with $Q = \frac{10}{17} = 0.588$. The

next structure in this series $d(1p)d(3p)$ has $Q = \frac{3}{5} = 0.60$, and the even mixture of the two sequences, $d(1p)d(3p)d(3p)d(1p)d(3p)$, leads to $Q = \frac{16}{27} = 0.593$, close to the maximum Q value encountered in the experiments. Hence, the magnetic structure may gain Zeeman energy on the expense of exchange energy by this increase of Q. Note that sequences with an even number of pairs do not show up in these considerations, because they do not change the resulting value of the ferromagnetic component.

The magnetic system has another possibility for gaining Zeeman energy, namely by changing a double pair *dduu* into the sequence *duuu*, this could happen e.g. in the $\frac{10}{17}$ structure, where the spin configuration $d(1p)d(3p)d(3p)$ would change into a structure where the $d(3p) = duudduu$ parts are replaced by *duuduuu*. This modification does not alter Q, but the magnitude of the first harmonic in neutron diffraction is reduced, and a jump will appear in magnetization measurements due to the larger moment obtained by flipping a spin.

3 Superconductivity

Superconductivity was first observed in 1911 by H. Kamerlingh Onnes as the disappearance of resistivity in the metals mercury, lead and tin at a critical temperature, T_c. Hence, the first hallmark of superconductivity, and what gave rise to the name, was perfect conductivity. Later, in 1933, Meissner and Ochsenfeld discovered the second hallmark of superconductivity, namely perfect diamagnetism. This effect excludes an applied magnetic field from entering and expels already applied fields upon cooling through the superconducting transition at T_c.

Superconductivity, as explained in the BCS theory, is caused by a many body interaction between the electrons in the conduction band of solids resulting in the creation of electron or hole pairs [26]. The idea of the BCS theory is that one conduction electron interacts with the ionic lattice and creates an excitation in the form of a phonon. This phonon propagates through the lattice and causes a local change of the charge density which will attract another electron, whereby an indirect interaction is established. The great success of the BCS theory was to prove that the conduction electrons, collectively coupled in Cooper pairs by an attractive coupling (actually any attractive coupling, not necessarily phonon mediated), did indeed have a lower energy than the non-coupled electrons. It should be noted that the electrons in a Cooper pair have opposite spins and move in opposite directions, thus one may think of the condensate as a boson quasi particle state where the electrons are constantly changing partners.

The pair binding differs in some ways from the ordinary binding of an isolated pair of particles by an attractive force. In conventional superconductors at $T = 0$ the orbital state of the pair has a radius ξ_0 typically of order 10^{-6} m, so large that the individual pairs overlap strongly in space, and the binding turns out to be cooperative - the binding energy 2Δ of any one pair depends on how many other pairs have condensed.

One way to think of the superconducting and normal electrons in the solid, is to consider a two-fluid model. At zero temperature, all electrons are in the superconducting boson condensate state. As the temperature is increased, single-particle excitations with energy larger than the superconducting energy gap emerge. Here, it is important not to imagine that we have two completely independent interpenetrating fluids, because the properties of the single-particle excitations and the pairs interact with each other. For instance, the energy of the single-particle excitations depend on the binding energy of the pairs, while the binding energy of the pairs will depend on how many single-particle excitations are present.

The above introduces some of the basic principles of the theories of superconductivity which are important to keep in mind when reading this thesis. I will not go through an evaluation of the basic properties of superconductivity, simply because this thesis focusses mainly on the magnetic properties. However, some of the superconducting properties are important when regarding the interaction with magnetism and they will be introduced in the next section.

3.1 Superconducting parameters

The superconducting energy gap plays a role when considering the electrons at the Fermi surface, which mediate the magnetic coupling. In the weak SC coupling limit the energy gap Δ is much smaller than the Debye phonon energy $k\theta_D$, and the BCS coupling parameter NV, is required to be smaller than unity where N is

the number of one-electron states per energy range at the Fermi level, and V is the BCS coupling constant describing the attraction between electrons. The energy gap at zero temperature can be evaluated in the weak coupling limit [26]:

$$\Delta(T=0) = 1.14k\theta_D e^{-1/NV} \tag{22}$$

This isotropic gap at the Fermi surface may interfere with the magnetic superzone gaps, created by the Fermi surface nesting structure.

The critical temperature of superconductivity T_c is evaluated as the temperature where $\Delta(T)$ is zero:

$$\Delta(T=0) = 1.76kT_c \tag{23}$$

T_c is suppressed when magnetic ions appear in the solid, the history of which is described in section 1.1, and the details of T_c in the RNi_2B_2C is examined in section 3.2.

The coherence length is a measure for the distance over which the two electrons in the Cooper pairs are correlated, given by:

$$\xi \sim \frac{\hbar v_f}{\Delta_{BCS}(0)} \sqrt{\frac{T_c}{T_c - T}} \tag{24}$$

where the coherence length at zero temperature is calculated in the BCS approximation, and the temperature dependence may be obtained using Ginzburg-Landay theory. The coherence length is important in the relation to ordered magnetic structures since the magnetic field emerging from the antiferromagnetic structures will not affect the order parameter of superconductivity, if the modulation of magnetic moments is zero in average on the length scale of the coherence length. This is the case in RNi_2B_2C where ξ is of the order 100 Å.

The Ginzburg-Landau parameter $\kappa = \frac{\lambda}{\xi}$ determines whether the superconductor is type I or II. For $\kappa < \frac{1}{\sqrt{2}}$ the energy of the normal to superconducting region domain wall is positive, causing total screening of a magnetic field, and it is a type I superconductor. However, for $\kappa > \frac{1}{\sqrt{2}}$ the domain wall energy is negative when the applied magnetic field H is larger than the first critical magnetic field H_{c1}, thus making it favorable to create as many domain walls as possible. This means creating a maximum number of regions of one flux quantum in the type II superconductor in a magnetic field larger than H_{c1}. The RNi_2B_2C are type two superconductors with κ in the range of 5 - 10.

The penetration depth λ is defined as the length scale of the penetration of the magnetic field into the superconducting type II material: $B_i(x) = B_{applied}\ e^{(-x/\lambda)}$. The simple picture of a superconductor is that there are flux lines with high fields penetrating regions with zero field superconductivity. In the RNi_2B_2C the penetration depth is of the order 500 Å to 1000 Å, and hence the flux lines appearing in a moderate field will actually be closer spaced than the penetration depth. Therefore the picture to have in mind here is an almost constant field throughout the superconducting phase, penetrated by regions of zero superconductivity.

Superconductivity is suppressed in a type II superconductor at a field H_{c2} when the density of flux lines becomes so high that the normal cores are overlapping. The upper critical field is given by:

$$H_{c2} = \frac{\Phi_0}{2\pi\xi^2}. \tag{25}$$

As stated above in equation (24) the coherence length is inversely proportional to the energy gap, so the upper critical field is proportional to the square of the energy gap: $H_{c2} \propto \Delta^2$. As mentioned earlier in this section, the energy gap depends the density of states, i.e. on the effective number of Cooper pairs, N. Keeping equation (25) in mind it is clear that structures with nesting on the Fermi surface may effect the upper critical field of superconductivity.

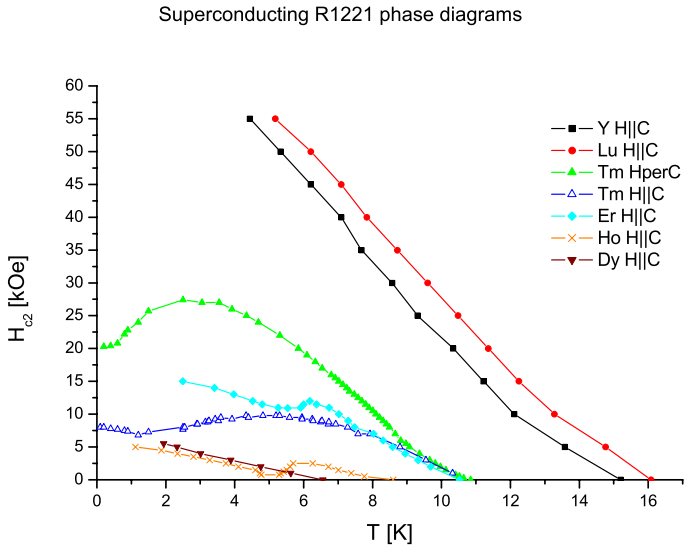

Figure 6. The upper critical field for superconductivity H_{c2} for the field applied along the c axis in the RNi_2B_2C. Additionally for $TmNi_2B_2C$, H_{c2} for a field in the a direction is presented. Data are taken from references [27], [28], [29], [30], [17], and [31].

The upper critical field for the RNi_2B_2C is presented in figure 6. Notice that H_{c2} is much larger for the non-magnetic compounds YNi_2B_2C and $LuNi_2B_2C$ ($\approx$ 6 T), than for the compounds containing magnetic ions ($\approx$ 1 T - 2 T). When introducing magnetic ions in the crystal the superconductivity is suppressed due to the spin disorder. These spins will cause a Zeeman shift in opposite directions of the energy of the spin up and spin down electrons in the Cooper pair. The resulting spin flipping can break the Cooper pairs and thereby cause a reduction of the superconducting order parameter. This spin-flip pair breaking effect reduces the upper critical field equally throughout the temperature range.

Another effect sets in at an antiferromagnetic ordering temperature, where the introduction of a new periodicity introduces a gap in the electron structure and reduces the available number of electrons on the Fermi surface, which decreases the upper critical field. For $ErNi_2B_2C$ and $HoNi_2B_2C$ this coherent effect causes a sharp cusp at 6 and 5 K, respectively. The smooth change in the c axis $TmNi_2B_2C$ case around 3 K is also due to the appearance of the nesting structure, which was presented in reference [20].

3.2 Understanding T_c: de Gennes scaling

Superconductivity appears in the RNi_2B_2C, for non-magnetic rare earths Y and Lu, but also compounds with magnetic ions Dy, Ho, Er, and Tm are superconducting. The transition temperature of these compounds may be understood in terms of de Gennes scaling, which will be discussed below.

The idea in de Gennes scaling for magnetic ions in a superconductor is that the superconducting transition temperature will increase linearly with the decrease of the magnetic ordering temperatures. This happens because the pair breaking effect of the magnetic ions is due to the exchange coupling with the conduction electrons rather than to the dipole coupling. The transition temperature to an ordered magnetic structure is given by

$$T_{\mathrm{N}} = \frac{\mathcal{J}(\mathbf{Q})J(J+1)}{3k_B} \tag{26}$$

where $\mathcal{J}(\mathbf{Q})$ is the value of the exchange interaction at the ordering vector $\mathbf{Q}$. Since the exchange interaction has its origin in the Coulomb interaction and the Pauli principle, we need to consider only the spin S, of the ion, and not the total angular momentum J, which means that $\mathcal{J}(\mathbf{Q})$ is proportional to $(g_{\mathrm{J}}-1)^2$, where g_{J} is defined in equation (5), on page 10. Intuitively one might expect the Nèel temperature to be proportional to the magnetic moment which would give a factor of g_J^2, but this would be wrong, since the exchange coupling between the magnetic ions originates in a coupling between the spins, whereas the orbital angular momentum couples via the dipole interaction.

All in all, the transition temperature is proportional to the de Gennes factor, which is defined as:

$$dG = (g_{\mathrm{J}}-1)^2\ J(J+1). \tag{27}$$

Similarly the superconducting transition temperature will be suppressed by the existence of magnetic moments in the solid. Since the pair breaking of the Cooper pairs by the magnetic ions takes place via the exchange coupling, the superconducting transition temperature may decrease linearly with the increase of the de Gennes factor. Table 3 presents the de Gennes factors and the superconducting transition temperatures of the RNi_2B_2C.

	Pr	Nd	Sm	Gd	Tb	Dy	Ho	Er	Tm	Yb	Lu
$4f$ e$^-$	2	3	5	7	8	9	10	11	12	13	14
S	1	$\frac{3}{2}$	$\frac{5}{2}$	$\frac{7}{2}$	3	$\frac{5}{2}$	2	$\frac{3}{2}$	1	$\frac{1}{2}$	0
L	5	6	5	0	3	5	6	6	5	3	0
J	4	$\frac{9}{2}$	$\frac{5}{2}$	$\frac{7}{2}$	6	$\frac{15}{2}$	8	$\frac{15}{2}$	6	$\frac{7}{2}$	0
g_J	$\frac{4}{5}$	$\frac{14}{11}$	$\frac{2}{7}$	2	$\frac{3}{2}$	$\frac{4}{3}$	$\frac{5}{4}$	$\frac{6}{5}$	$\frac{7}{6}$	$\frac{8}{7}$	0
dG	0.8	1.8	4.5	15.8	10.5	7.1	4.5	2.6	1.2	0.32	0
T_c (K)	-	-	-	-	-	6.4	8.0	10.5	11.0	-	16.6

Table 3. Summary of the magnetic properties: number of 4f electrons, the S-, L-, and J-quantum numbers, the Lande g_J factor, the de Gennes factor, and T_c. The compounds with R = Ce, Pm and Eu have never been examined in the literature, so therefore they are not discussed here. The superconducting transition temperatures have been taken from reference [32].

The de Gennes factor increases in the first part of the series, has a maximum for $GdNi_2B_2C$, and decreases gradually until it is zero for $LuNi_2B_2C$. Looking at the last part of table 3, it is clear that T_c is controlled by de Gennes scaling, T_c increases concomitantly with the decrease of the de Gennes factor from $DyNi_2B_2C$ to $LuNi_2B_2C$, and also the non-magnetic compound YNi_2B_2C has $T_c = 15.6$ K. The lack of superconductivity in $GdNi_2B_2C$ and $TbNi_2B_2C$ can be understood when considering the large de Gennes factor, however one would expect to see superconductivity in the first part of the series, where the de Gennes factor is similar to what is seen in the superconducting compounds in the last part of the series. The reason for the absence of superconductivity in the first part of the series lies in the density of states at the Fermi surface. Band structure calculations show that the density of states has a peak at the Fermi energy which arises mainly from the Ni - $3d$ electrons. This is generally believed to be responsible for superconductivity in these compounds [33, 34, 35]. This peak is not observed for the compounds in the first part of the series, probably because the density of states $N(E_F)$ and the shape of the density of states depend strongly on the value of $\frac{c}{a}$ [34]. Note that the $PrNi_2B_2C$ and $YbNi_2B_2C$ compounds are heavy fermion compounds [36, 37].

3.3 How magnetism affects the SC properties

Nesting wave vector in RNi_2B_2C

There is magnetic ordering with $\mathbf{Q} \approx (0.55,0,0)$ for the rare earths Gd, Tb, Ho, and Er in zero applied magnetic field [15, 16, 17, 18, 19] and for Tm, Ho and possibly Dy in a finite applied field [20, 21, 22].

A direct evidence of the interaction with superconductivity is the observation of a phonon softening at T_c at the wave vector $\mathbf{Q} \approx (0.55,0,0)$, which so far has been observed in YNi_2B_2C, $LuNi_2B_2C$, and $HoNi_2B_2C$ [38, 39, 40].

A more indirect example of the interaction with superconductivity appears in $HoNi_2B_2C$ where superconductivity is suppressed at temperatures and fields where a wave vector $\mathbf{Q} \approx (0.58,0,0)$ appears [21]. At T = 8 K superconductivity appears and at 6 K the $\mathbf{Q} \approx (0.58,0,0)$ phase appears concurrently with a suppression of superconductivity. Around 5 K, the magnetic phase changes in to a $(00\frac{2}{3})$ ordered state, which is almost immediately replaced by a (001) commensurate structure. Around 5 K superconductivity reappears. Neutron diffraction studies on Lu and Dy doped $HoNi_2B_2C$ show that it is indeed the a axis modulated structure which is responsible for the suppression of superconductivity [41]. Applying a magnetic field in the [100] axis of pure $HoNi_2B_2C$ yields the same behavior in field as in temperature, the (001) structure changes into the $(00\frac{2}{3})$ phase after which the $(0.58, 0, 0)$ phase persists up to a field of approx 1.5 T where the field-induced ferromagnetic state sets in [21]. No theoretical work has been performed on $HoNi_2B_2C$ but the experiments indicate that the $\mathbf{Q} \approx (0.58,0,0)$ phase may be the $\frac{4}{7}$ phase, which we have observed in $ErNi_2B_2C$.

CEF anisotropy

An extreme magnetic anisotropy holds the local moments of the magnetic ions in specific directions dependent on the details of the crystalline electric field. For $TbNi_2B_2C$, $DyNi_2B_2C$, $HoNi_2B_2C$, and $ErNi_2B_2C$ the moments are confined to the ab plane for temperatures below approximately 100 K, and at even lower

temperatures a four clock behavior emerges which confines the moments for either the (110) direction ($DyNi_2B_2C$ and $HoNi_2B_2C$) or the (100) direction ($TbNi_2B_2C$ and $ErNi_2B_2C$). $TmNi_2B_2C$ and $YbNi_2B_2C$ have moments along the c axis [10]. For $GdNi_2B_2C$ the magnetic ion has 7 electrons giving a zero orbital moment which means there is no CEF splitting, and an isotropic paramagnetic moment is observed [42].

The CEF anisotropy results in an anisotropy in the upper critical field of superconductivity.

4 Neutron Diffraction

The neutron is an excellent probe for studying both nuclear and magnetic structures. First of all the neutron has no charge, therefore it can penetrate the material and auxiliary facilities. Further more, it interacts directly with the nucleus and not with the electron cloud as is the case for X-ray diffraction, which means that also the lighter elements can be studied with neutrons. Secondly, it has a magnetic moment which interacts with the magnetic moment of the atom, so magnetic structures will also be visible with neutrons. Thirdly, the energy of the neutron is in the range of crystalline and magnetic excitations which means that phonons, magnons, and other excitations of the spin system can be studied. In this thesis I focus on the study of the magnetic structures with neutron diffraction. In order to examine the crystalline or magnetic structure of a material, the amount of elastically scattered neutrons in a particular area of space dS is analyzed. If φ_{i} and φ_{f} are the incoming and final wave function of neutrons, the differential scattering cross section is defined as:

$$\frac{d\sigma}{d\Omega} \equiv \frac{(\sharp \text{ scattered neutrons in the solid angle } d\Omega \text{ per second})}{(\text{incoming flux})\, d\Omega} \tag{28}$$

$$= \frac{v|\varphi_{\mathrm{f}}|^2 dS}{v|\varphi_{\mathrm{i}}|^2 d\Omega} = \frac{|\varphi_{\mathrm{f}}|^2}{|\varphi_{\mathrm{i}}|^2} \cdot r^2, \tag{29}$$

here v is the speed of the neutrons, $d\Omega$ is the solid angle in which we have scattering, and $dS = r^2 d\Omega$. The differential scattering cross section is a sum of nuclear and magnetic scattering. Neutron scattering arises from scattering of neutrons by the nuclear or electron spin density. The periodicity of the crystalline lattice, or of the magnetic moment vectors located on the atoms, causes the scattering to be concentrated at certain directions in space.

4.1 Nuclear Diffraction

To describe the scattering of neutrons on a crystal containing different atoms, we first look at scattering of a neutron on one atom. Since the neutron beam which is used in scattering experiments is both monochromatic and collimated, the incoming neutron is described by a plane wave (see figure 7).

$$\varphi_{\mathrm{i}} = e^{i\mathbf{k}_{\mathrm{i}} \cdot \mathbf{r}} \tag{30}$$

The wavelength of the neutron is about 5 orders of magnitude larger than the nuclear force range. The scattering is weak and may be accounted for in the Born approximation (the single scattering particle can be considered as a perturbation of the incident beam). Hence the scattered wave from a single fixed nuclei is described by a spherical wave:

$$\varphi_{\mathrm{f}} = b \frac{e^{i\mathbf{k}_{\mathrm{f}} \cdot \mathbf{r}}}{r}, \tag{31}$$

where the amplitude b is called the scattering length. Combining equations (29), (30), and (31) we get:

$$\frac{d\sigma}{d\Omega} = b^2, \tag{32}$$

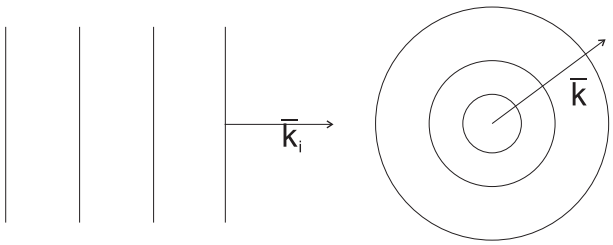

Figure 7. The incoming neutron beam is described by a plane wave scattering on a fixed nuclei, and the outgoing neutron beam is spherically symmetric.

and the meaning of the scattering length as the strength of the scattering from the atom is evident.

If we look at a crystal lattice of identical atoms, we need to consider the phase difference $\Delta\phi_n$ between two waves scattered on different atoms separated by the vector $\mathbf{R}_n$:

$$\Delta\phi_n = \mathbf{k}_\mathrm{i} \cdot \mathbf{R}_n - \mathbf{k}_\mathrm{f} \cdot \mathbf{R}_n = \boldsymbol{\kappa} \cdot \mathbf{R}_n, \quad \boldsymbol{\kappa} = \mathbf{k}_\mathrm{i} - \mathbf{k}_\mathrm{f} \tag{33}$$

The outgoing wave is a summation of all waves of the type $b\frac{e^{i\mathbf{k}_\mathrm{f}\cdot\mathbf{r}}}{r}e^{i\Delta\phi_n}$:

$$\varphi_\mathrm{f} = b\frac{e^{i\mathbf{k}_\mathrm{f}\cdot\mathbf{r}}}{r}\sum_n e^{i\boldsymbol{\kappa}\cdot\mathbf{R}_n}, \tag{34}$$

assuming that the distance $\mathbf{r}$ is large enough to be considered constant in the crystal. The differential scattering cross section becomes:

$$\frac{d\sigma}{d\Omega} = |\sum_n b e^{i\boldsymbol{\kappa}\cdot\mathbf{R}_n}|^2. \tag{35}$$

If the material consists of different atoms then the scattering length will depend on the different atoms, and will be denoted b_n. Equation (35) is valid in general, even if the atoms do not form a lattice.

If we have a primitive lattice of similar atoms, the b goes out of the sum. We can describe every distance between two atoms as a linear combination of three unit cell vectors: $\mathbf{R}_n = n_1\mathbf{a} + n_2\mathbf{b} + n_3\mathbf{c}$. Inserting $\mathbf{R}_n$ in the sum from equation (35) we get three sums of the form $|\sum_{n_1=0}^{N_1-1} e^{i\boldsymbol{\kappa}\cdot n_1\mathbf{a}}|^2$, and we recognize the Sinc function:

$$|\sum_{n_1=0}^{N_1-1} e^{i\boldsymbol{\kappa}\cdot n_1\mathbf{a}}|^2 = |\frac{1-e^{i\boldsymbol{\kappa}\cdot N_1\mathbf{a}}}{1-e^{i\boldsymbol{\kappa}\cdot\mathbf{a}}}|^2 = \frac{\sin^2(\frac{N_1}{2}\boldsymbol{\kappa}\cdot\mathbf{a})}{\sin^2(\frac{1}{2}\boldsymbol{\kappa}\cdot\mathbf{a})} = S_{N_1}(\boldsymbol{\kappa}\cdot\mathbf{a}) \tag{36}$$

The Sinc function has the peak the value N_1^2 and the width is proportional to $\frac{1}{N_1}$, for $\boldsymbol{\kappa}\cdot\mathbf{a} = 2\pi m$, m is an integer. It becomes a sum of delta functions as N_1 becomes large. If we write $\mathbf{R}_n = n_1\mathbf{a}+n_2\mathbf{b}+n_3\mathbf{c}$, we can split the sum in equation (35) into three Sinc functions and for large N_1, N_2, and N_3 we get:

$$\frac{d\sigma}{d\Omega} = |b|^2 N_1 N_2 N_3 \sum_{m=-\infty}^{\infty} \delta(\boldsymbol{\kappa}\cdot\mathbf{a} + \boldsymbol{\kappa}\cdot\mathbf{b} + \boldsymbol{\kappa}\cdot\mathbf{c} - 2\pi m),\ m\,\text{integer}. \tag{37}$$

When changing from Sinc functions to delta functions, it is crucial to make sure that the area of the curve is constant, which shows that the differential scattering cross section is proportional to the number of unit cells in all three directions.

If neutron scattering is performed at finite temperature one must consider the thermal motion of the crystal. This is called the Debye-Waller factor: e^{-2W}, where W is inversely proportional to the Debye temperature of the crystal. In $TmNi_2B_2C$ Gasser *et al.* find a Debye temperature of $\Theta_D \sim 200$ Kelvin [10]. In our case we do neutron scattering at temperatures between 20 mK and 30 K, therefore we need not bother with crystal vibrations.

The reciprocal lattice

The reciprocal lattice consists of the vectors $\mathbf{G}^*$ for which the dot product of $\mathbf{G}^*$ with a lattice vector is a multiple of 2π. Inserting $\mathbf{G}^*$ for $\boldsymbol{\kappa}$ in equation (37) shows that the reciprocal lattice vectors are exactly the vectors for which $\frac{d\sigma}{d\Omega}$ is different from zero. So, in scattering experiments we get an image of the reciprocal lattice. From this image we can extract the crystalline lattice. If we write $\mathbf{G}^*$ as a linear combination of three vectors: $\mathbf{G}^* = h\mathbf{a}^* + k\mathbf{b}^* + l\mathbf{c}^*$ it becomes clear that the following vectors fulfill the condition that $\mathbf{a}\cdot\mathbf{b}^* = 2\pi\delta_{ab}$, where $\mathbf{a}$ are the direct lattice vectors and $\mathbf{b}^*$ are the reciprocal lattice vectors.

$$\mathbf{a}^* = 2\pi\frac{\mathbf{b}\times\mathbf{c}}{\mathbf{a}\cdot(\mathbf{b}\times\mathbf{c})},\ \ \mathbf{b}^* = 2\pi\frac{\mathbf{c}\times\mathbf{a}}{\mathbf{a}\cdot(\mathbf{b}\times\mathbf{c})},\ \ \mathbf{c}^* = 2\pi\frac{\mathbf{a}\times\mathbf{b}}{\mathbf{a}\cdot(\mathbf{b}\times\mathbf{c})}. \tag{38}$$

Nuclear differential scattering cross section of the Borocarbides

The crystal structure of RNi_2B_2C is shown in figure 1 on page 9. There are several different atoms in the unit cell of RNi_2B_2C, so to calculate the differential scattering cross section we use equation (35). The sum is split into a sum in the unit cell and a lattice sum by writing the position vector as a vector in the unit cell plus a lattice vector: $\mathbf{R}_n = \mathbf{r}_n + n_1\mathbf{a} + n_2\mathbf{b} + n_3\mathbf{c} = \mathbf{r}_n + \mathbf{G}_{n_1n_2n_3}$.

$$\begin{aligned}\left(\frac{d\sigma}{d\Omega}\right)_{\mathrm{nuc}} &= |\sum_n b_n e^{i\boldsymbol{\kappa}\cdot\mathbf{r}_n}\sum_{n_1n_2n_3} e^{i\boldsymbol{\kappa}\cdot\mathbf{G}_{n_1n_2n_3}}|^2 \\ &= |F(\boldsymbol{\kappa})|^2 N_1N_2N_3\sum_{\mathbf{G}^*}\delta(\boldsymbol{\kappa}-\mathbf{G}^*),\end{aligned} \tag{39}$$

for N_1, N_2, N_3 large. Here, we get essentially the same formula as in equation (37) and the only difference is that the prefactor b^2 is replaced by the square of the structure factor $|F(\boldsymbol{\kappa})|^2$, where:

$$F(\boldsymbol{\kappa}) = \sum_n b_n e^{i\boldsymbol{\kappa}\cdot\mathbf{r}_n} \tag{40}$$

The structure factor $F(\boldsymbol{\kappa})$ can be interpreted as the scattering length of the unit cell. To calculate the structure factor of the RNi_2B_2C we need the position vectors of the atoms in the unit cell, given in reciprocal units:

$$\mathbf{r}_{\mathrm{R}} = (0,0,0)\,,\,(\tfrac{1}{2},\tfrac{1}{2},\tfrac{1}{2}) \tag{41}$$

$$\mathbf{r}_{\mathrm{Ni}} = (\tfrac{1}{2},0,\tfrac{1}{4})\,,\,(\tfrac{1}{2},0,\tfrac{3}{4})\,,\,(0,\tfrac{1}{2},\tfrac{1}{4})\,,\,(0,\tfrac{1}{2},\tfrac{3}{4}) \tag{42}$$

$$\mathbf{r}_{\mathrm{B}} = (\tfrac{1}{2},\tfrac{1}{2},\tfrac{1}{2}-z)\,,\,(\tfrac{1}{2},\tfrac{1}{2},\tfrac{1}{2}+z)\,,\,(0,0,z)\,,\,(0,0,1-z) \tag{43}$$

$$\mathbf{r}_{\mathrm{C}} = (\tfrac{1}{2},\tfrac{1}{2},0)\,,\,(0,0,\tfrac{1}{2}), \tag{44}$$

z depends on which rare earth is in the Borocarbide, generally $z \simeq \frac{1}{3}$, for $TmNi_2B_2C$ $z = 0.3598$, and for $ErNi_2B_2C$ $z = 0.3597$ [43]. For the scattering vector $\boldsymbol{\kappa} = (h, k, l)$ in reciprocal lattice coordinates the structure factor becomes:

$$F(\boldsymbol{\kappa}) = b_{\mathrm{Re}}\left(1 + (-1)^{h+k+l}\right) + 2b_{\mathrm{Ni}}\cos(\frac{l\pi}{2})((-1)^h + (-1)^k)$$
$$+ \quad 2b_{\mathrm{B}}\cos(2\pi z l)(1 + (-1)^{h+k+l}) + b_{\mathrm{C}}((-1)^{h+k} + (-1)^l). \qquad (45)$$

As an example the structure factor for the relevant reflections in $TmNi_2B_2C$ are presented in table 4. For some reciprocal lattice points the structure factor is zero. These are all points $[h, k, l]$ where the sum $h+k+l$ is odd. If the sum is even the structure factor is different from zero and the size of it depends on to what extend the waves in the crystal cancel out. The strongest Bragg peak is [200] or equivalently [020], since the waves are displaced by exactly one wavelength when scattering on these planes. Notice the intensity of scattered neutrons is proportional to the square of the structure factor, giving a scaling between weak and strong peaks of $\frac{9.29^2}{0.043^2} = 46.700$.

$[h, k, l]$ $[rlu]$	$\lvert F(h, k, l)\rvert$ 10^{-12} cm
[100], [010]	0
[001]	0
[110]	1.05
[200], [020]	9.29
[111]	0
[002]	1.81
[003]	0
[004]	4.66
[005]	0
[006]	0.043

Table 4. Structure factors for $TmNi_2B_2C$ reflections.

4.2 Magnetic Diffraction

Magnetic scattering length

The neutron is a spin $\frac{1}{2}$ particle with a magnetic moment vector $\boldsymbol{\mu}_{\mathrm{n}}$ which will interfere with the magnetic field of the unpaired electrons of the atoms. Since this is a matter of vectors interfering, the scalar scattering length of an atom cannot be used directly, and needs to be redefined.

In the Born approximation, the magnetic scattering length b_{m} can be calculated as being proportional to the Fourier transform of the interaction potential V_{int} between the neutron and the electron at the atom [44]:

$$b_{\mathrm{m}} \propto V(\boldsymbol{\kappa})\,,\; V(\boldsymbol{\kappa}) = F(V_{\mathrm{int}}(\mathbf{R})) \qquad (46)$$

$\mathbf{R}$ is the relative distance between the neutron and the electron. This equation is physically intuitive since the interaction is off course, scaled by the interaction potential of the material and the scatterer. The Fourier transform represents the summation of the different contributions having different phases.

The interaction potential between the magnetic moment of the neutron and the magnetic field surrounding the electron is simply the dot product of the two:

$$V_{\text{int}}(\mathbf{R}) = \boldsymbol{\mu}_{\text{n}} \cdot \mathbf{H}(\mathbf{R}) \tag{47}$$

The magnetic field surrounding the electron is given by the rotation of the vector potential, and the vector potential of an electron is the dipole field: the cross product of the spin of the electron $\mathbf{S}$ and the position vector $\mathbf{R}$, divided by R^3. Hence, the magnetic scattering length of scattering of a neutron on an electron can be written as:

$$b_{\text{m}}(\boldsymbol{\kappa}) \propto \boldsymbol{\mu}_{\text{n}} \cdot \int e^{i\mathbf{K}\cdot\mathbf{R}} \nabla \times \frac{\mathbf{S} \times \mathbf{R}}{R^3} d^3r \tag{48}$$

When evaluating this integral and remembering all constants that were left out in the above derivation, we get the magnetic scattering vector to be:

$$\mathbf{b}_{\text{m}}(\boldsymbol{\kappa}) = \frac{e^2\gamma}{2m_{\text{e}}c^2} f(\boldsymbol{\kappa}) \frac{|\boldsymbol{\mu}|}{\mu_{\text{B}}} (\hat{\mu} - \hat{\kappa}(\hat{\kappa} \cdot \hat{\mu})), \tag{49}$$

$\hat{\kappa}$ and $\hat{\mu}$ are unit vectors in the direction of $\boldsymbol{\kappa}$ and $\boldsymbol{\mu}$, $\gamma = -1.91$ is the gyromagnetic factor for the neutron, e the proton charge, c the velocity of light, m_{e} the electron mass, $f(\boldsymbol{\kappa})$ is the magnetic form factor, and μ_{B} the Bohr magneton. The magnetic form factor $f(\boldsymbol{\kappa})$ is determined by the distribution of magnetization within a single atom. The form factor is the Fourier transform of the space distribution of the unpaired electrons. This is similar to the nuclear structure factor where it was a sum over the unit cell, but in this case the sum is over the magnetic moments of the unpaired electrons in the electron cloud. This sum can be evaluated using tabulated values for the free ion case [45]. Note when doing neutron scattering, we only see the part of the magnetic moment that is perpendicular to the scattering vector, hence the scattering length is zero if the scattering vector is parallel to the magnetic moment.

The magnetic neutron scattering length can be of the same order of magnitude as nuclear scattering amplitudes. The neutron is therefore an ideal probe for magnetic structures. However, the strength of the magnetic reflections decreases fast due to the form factor, as the length of the scattering vector increases.

When replacing b in equation (35), the magnetic differential scattering cross section can be calculated. Appendix A gives an example of how this can be done.

5 $ErNi_2B_2C$

In 1996, it was reported that weak ferromagnetism was observed in $ErNi_2B_2C$ for temperatures below 2.3 K [46]. This postulate remained unresolved until Choi and co-workers published neutron diffraction data of this weak ferromagnetic phase in 2001 [25]. They found not only odd higher order reflections of the magnetic phase, but also even order peaks, which they proved where magnetic in origin. The even order reflections represent an antiferromagnetic wave where the length of a net ferromagnetic moment oscillates with the same period. Note that the oscillation is among moments pointing in the same direction, only the length in this direction varies. The exact spin structure of this weak ferromagnetic phase was resolved by Jensen in reference [1].

The motivation for doing the present experiments on $ErNi_2B_2C$ was a clear indication of an interaction between magnetic order and superconductivity, namely the observation of a sharp cusp at T_N in the temperature dependence of the upper critical field H_{c2}. Interestingly, it turned out that the sharp cusp appears only when the field is applied along [001], when the field is along [100] it has a minor cusp, and only a smooth change of slope appears, when the field is along [110] [47]. The speculation was raised that only an antiferromagnetic state, which is driven by Fermi surface nesting, is able to cause a sharp cusp in H_{c2}, whereas the antiferromagnetic state with the field along [100] and [110] might be different, not dependent on the nesting feature. In the following section, the magnetic structures of $ErNi_2B_2C$ are examined in general in the presence of a magnetic field, and specifically close to H_{c2}, in order to improve the understanding of the interdependence of superconductivity and magnetism.

In zero field the ordering wave vector is found to be along the a (b) axis and the ordered moments are along the b (a) axis perpendicular to the ordering wave vector $\mathbf{Q}_N^A = Q\mathbf{a}^*$ ($\mathbf{Q}_N^B = Q\mathbf{b}^*$), with $Q = 0.55$ [19, 43]. The Néel temperature is $T_N \approx 6$ K and the superconducting transition occurs at $T_c = 11$ K. The even order peaks observed by Choi *et al.* is not observed in zero field in our samples, see section 5.6 for further details.

5.1 Experimental details

The results of examining the magnetic structure of $ErNi_2B_2C$ are based on several neutron-scattering experiments carried out on the E1 triple-axis and the E4 two-axis spectrometers, at the Berlin Neutron Scattering Center (BENSC), Hahn-Meitner Institut (HMI). A magnetic field was applied along the crystallographic directions [010], [110], [110] + 22.5°, and [001] of crystals with dimensions of approximately $2 \times 3 \times 0.5$ mm^3. All samples were grown by a high-temperature flux method and isotopically enriched with 99.5 % ^{11}B to enhance the neutron transmission [30]. The analysis of the nuclear Bragg peaks shows significant extinction even for the weaker reflections. A wavelength of λ between 2.413 and 2.444 Å was selected by the (002) reflection of a pyrolytic graphite (PG) monochromator and higher-order contamination was suppressed by a PG filter in front of the monochromator. All measurements in an applied field were performed after zero-field cooling.

For fields applied within the ab plane (sections 5.2, 5.3, and 5.4), the experiments were carried out at the E1 spectrometer using collimators of 70', 40', 60', and 60' inserted between source, monochromator, sample, analyzer, and detector,

respectively. A horizontal-field cryomagnet with a maximum field of 4.0 T was used. It has large blind angles for neutron diffraction, which restricts the accessible reciprocal space significantly.

For the field applied along [001] (section 5.5), the E4 spectrometer was used with collimators of 40' 40' 40' inserted between the source, the monochromator, the sample, and the detector in order to define the resolution. The vertical field was supplied by a cryomagnet with only a small blind angle and a maximum field of 14 T. Results are only reported for fields up to 13 T, because the crystal detached at higher fields.

Several long scans, where many orders of the magnetic reflections can be seen, are presented in section 5.6. The data in this section were from the preliminary investigations, performed at the cold neutron TAS7 spectrometer at the Risø National Laboratory DR3 research reactor. Neutron with an incoming energy of 9 meV was used with pyrolythic graphite (002) monochromator and (002) analyzer crystals. The collimation was open from source to monochromator to sample, 80' before the analyzer, and 140' after the analyzer.

5.2 Results: Field along [010]

A detailed field analysis of the two magnetic domains at the reflections $(200) - \mathbf{Q}_{\mathrm{N}}^{\mathrm{A}}$ and $(020) - \mathbf{Q}_{\mathrm{N}}^{\mathrm{B}}$ was performed at several temperatures with the field applied along [010]. In zero field, the magnetic domains with $\mathbf{Q} = \mathbf{Q}_{\mathrm{N}}^{\mathrm{A}}$ or $\mathbf{Q}_{\mathrm{N}}^{\mathrm{B}}$ are equally populated, but the application of the magnetic field along [010] suppresses the domain with the magnetic moments perpendicular to the magnetic field, i.e., the $\mathbf{Q}_{\mathrm{N}}^{\mathrm{B}}$ domain.

Note that the equal population of the two domains in zero field observed in our experiments may be sample dependent. The magnetostriction measurements by Doerr *et al.* show a strong asymmetry of their sample [48]. The volume ratio between the two orthorhombic domains is estimated to be 1:2, as explained by an unequal zero-field population of the two domains of the single-$\mathbf{Q}$ ordered system, and it is noticeable that even the asymmetry is detected to reappear in a reversible way, after the application of a field of 6.0 T.

Figure 8 presents scans of the magnetic reflections at T = 1.8 K in increasing fields. The scattering intensity due to the minority domain, $\mathbf{Q}_{\mathrm{N}}^{\mathrm{B}}$, which is presented in the left panel, is gradually suppressed by the magnetic field and the value of Q changes slightly from the zero-field value 0.552 to 0.555 during this process. In the case of the majority domain, $\mathbf{Q}_{\mathrm{N}}^{\mathrm{A}}$ shows several different peak positions in increasing fields, as can be seen in the right panel of Fig. 8. In zero field (blue circles) the reflection is observed at $Q = 0.55$, and the intensity has the same value as for the minority domain. As the field is increased to 0.4 T some of the minority domain intensity appears in the majority domain. At 0.8 T Q has changed to 0.57, increasing the field to 1.2 T causes the reflection to appear at 0.59, as the field is increased further to 1.4 T Q decreases to 0.58 and eventually at 1.8 T the reflection returns to the 0.57 value.

The transition from one Q value to another proceeds not as a continuous translation of $\mathbf{Q}$, rather the intensity jumps from one reflection to another. This can be seen in Fig. 9. In the left panel the transition at 0.7 T from the Q=0.55 to Q=0.57 is presented, and in the right panel the transition around 1 T from Q=0.57 to Q=0.59 can be seen. In both panels, the reflections start out as single peaks, then a shoulder is developed, and in the next scan, the reflection is shifted to an-

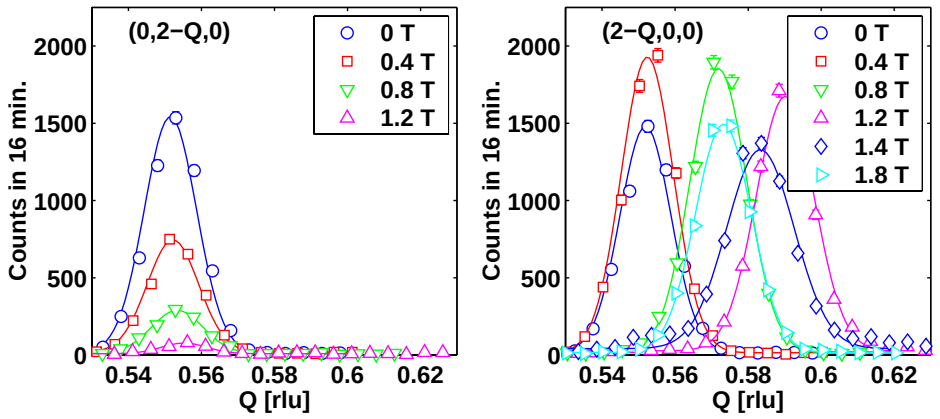

Figure 8. Scans of the magnetic reflection in increasing fields along [010]*, at* $T = 1.8$ *K. Left panel: minority* $\mathbf{Q}_N^B$ *domain. Right panel: Majority* $\mathbf{Q}_N^A$ *domain. Notice that* Q *shows the following values* $0.55, 0.57, 0.59, 0.58$*, and* 0.57 *respectively in increasing fields. The lines are one Gaussian fits to the data. The* Q *values are calculated by scaling the h-scans to the position of the* (020) *and* (200) *nuclear Bragg peaks.*

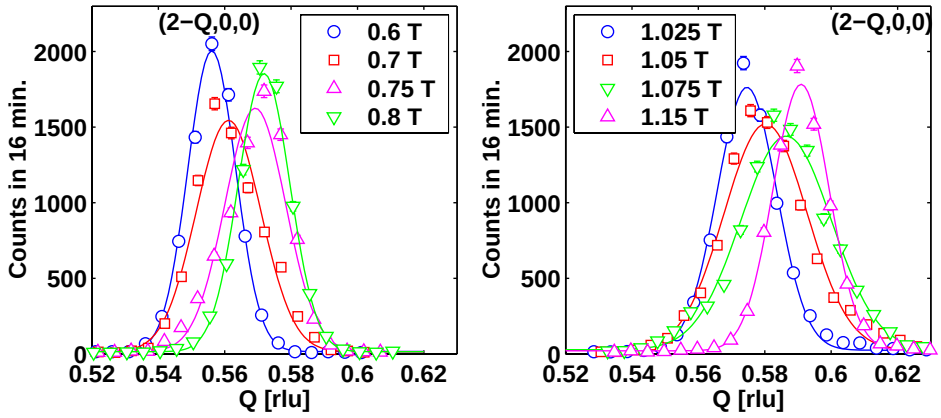

Figure 9. Scans of the majority $\mathbf{Q}_N^A$ *domain in increasing fields. Left panel: transition from* $Q = 0.55$ *to* $Q = 0.57$*. Right panel: transition from* $Q = 0.57$ *to* $Q = 0.59$*. The lines are one Gaussian fits to the data.*

other position, but now with a shoulder towards the previous Q position. Finally, in the last scans, one peak appears at the new Q value.

Since not only one, but two peaks appear at some field values, the data is fitted with two Gauss functions, which yields the correct positions of the reflections. The left panel of figure 10 presents the positions of the peaks, obtained when fitting with a two Gaussian function. The width of the two Gaussians are kept constant, at the value determined in zero and low fields, where only one peak appears. Fits with an amplitude larger than one half of the maximum amplitude are plotted as solid markers, cyan colored markers represent amplitudes within the range of one third to one half of the maximum amplitude, and open markers represent peaks with an amplitude smaller than one third of the maximum amplitude. In the low field range (up to 0.6 T at T = 1.8 K, and up to 0.8 T at T = 5.1 K) it was only possible to fit one peak to the scans. In comparison, the right panels present

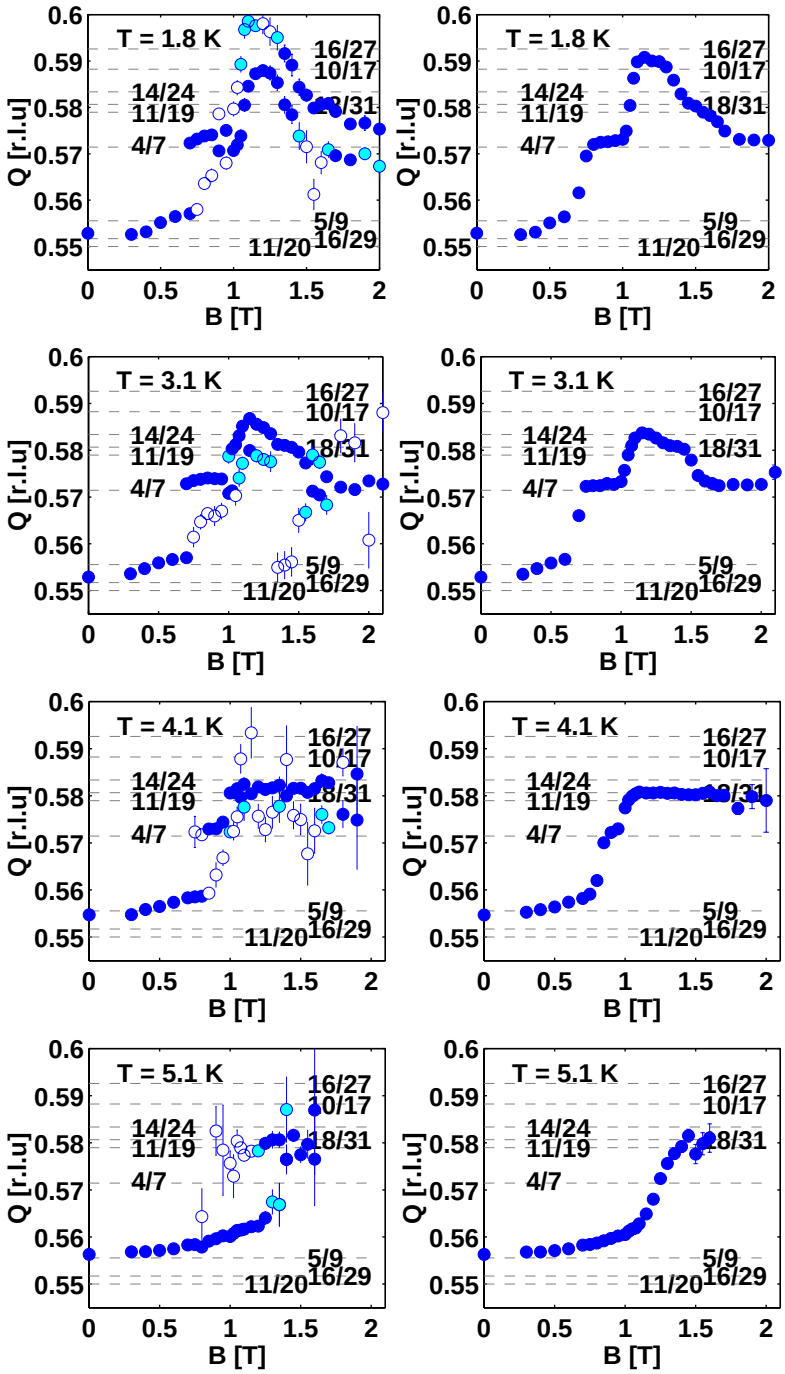

*Figure 10. Left panels: The position of the magnetic reflection in increasing fields, fitted with two gaussians, fixing the width of the Gaussians to the average width of the single peaks (*0.0153 *rlu FWHM at* 1.8 *K and* 0.00163 *rlu FWHM at* $T = 5.1$ *K). Fits with an amplitude larger than one half of the maximum amplitude are plotted as solid blue markers, cyan colored markers represent amplitudes within the range of one third to one half of the maximum amplitude, and open markers represent peaks with an amplitude smaller than one third of the maximum amplitude. Right panel: One Gaussian fits.*

one Gaussian fits to the same data. The details about the Q value come from the two Gaussian fits. However, the main features of the behavior of the magnetic reflection are equally visualized in the right panel, and in order to simplify the figures, all plots presented in the remaining part of this section are extracted from one Gaussian fits.

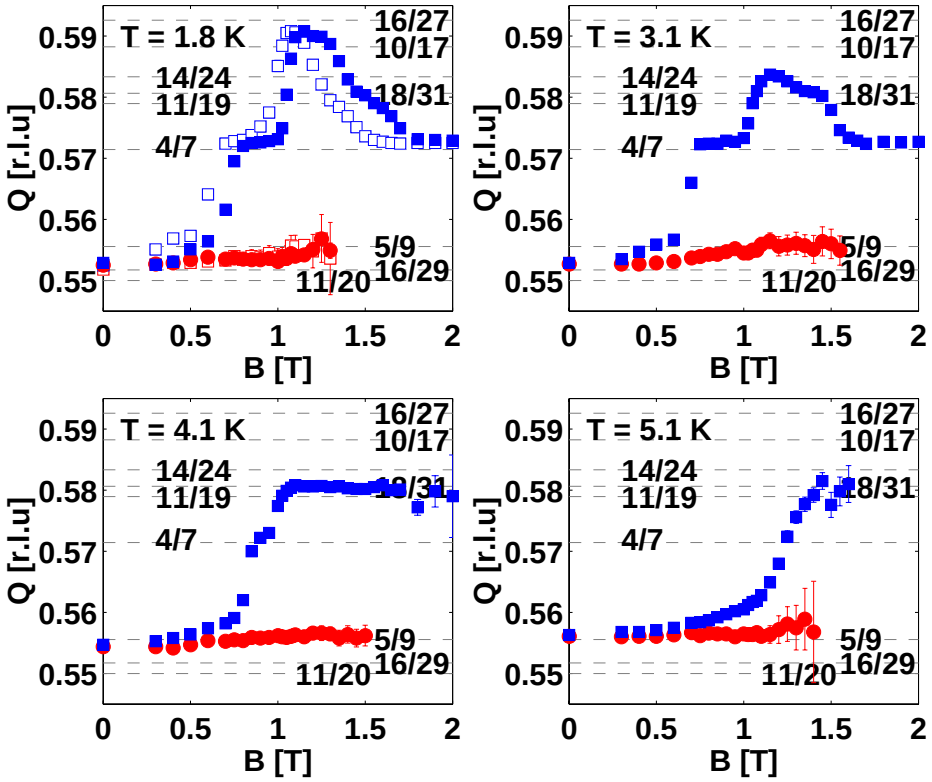

Figure 11. Positions of the magnetic reflections of the majority $\mathbf{Q}_N^A$ domain measured in h-scans at $(2-Q,0,0)$ (squares) and of the minority $\mathbf{Q}_N^B$ domain measured in k-scans at $(0,2-Q,0)$ (circles), as functions of a field applied along [010]*. Hysteresis is examined only for the* 1.7 *K data, where the solid symbols represent the data obtained when increasing the field, and the open ones show the decreasing field data.*

Figure 11 presents the positions of the magnetic reflections at $(200)-\mathbf{Q}_{\mathrm{N}}^{\mathrm{A}}$ and $(020)-\mathbf{Q}_{\mathrm{N}}^{\mathrm{B}}$ as a function of field, for the four temperatures examined. The positions are obtained by fitting a one Gaussian to the $[h00]$- and $[0k0]$-scans through the magnetic peaks, and scaling to the positions of the (200) and (020) nuclear Bragg reflections. The most likely commensurable values, given in the brackets, are indicated on the figure by the dashed lines. At 1.8 K, the value of Q changes from 0.552 ($\frac{11}{20}$ or $\frac{16}{29}$) to 0.573 ($\frac{4}{7}$) at 0.7 T, and from this value to 0.588 ($\frac{10}{17}$ or $\frac{16}{27}$) at 1.1 T. At 1.4 T Q is reduced to 0.580 ($\frac{11}{19}$ or $\frac{18}{31}$), and at 1.7 T it reverts to 0.573. The antiferromagnetic ordering disappears at about 2.1 T at which point the sample enters the saturated paramagnetic state. At 1.8 K, the reflections have been measured both for increasing and decreasing values of the field (solid and open symbols, respectively). In decreasing fields, the value of Q changes in steps between the same values, only a small field hysteresis of approx. 0.2-0.3 T is observed. As was already shown in figure 8, the scattering intensity due to the

minority domain is gradually suppressed by the magnetic field and in this figure it is clear that the value of Q changes slightly from the zero-field value 0.552 to 0.555 during this process.

Increasing the temperature to 3.1 K does not change the overall picture, however the magnetic phase with $Q = 0.588$ is not observed, instead $Q = 0.584$ appears in a narrow range of fields. At T = 4.1 K the $Q = 0.57$ reflection ($\frac{4}{7}$) is only seen for a few fields, and above 1 T the structure stays at $Q = 0.58$ until the intensity disappears. At the highest examined temperature T = 5.1 K, the Q value shifts gradually towards slightly higher Q, and at 1.3 T it jumps to $Q = 0.58$ where it stays until it disappears.

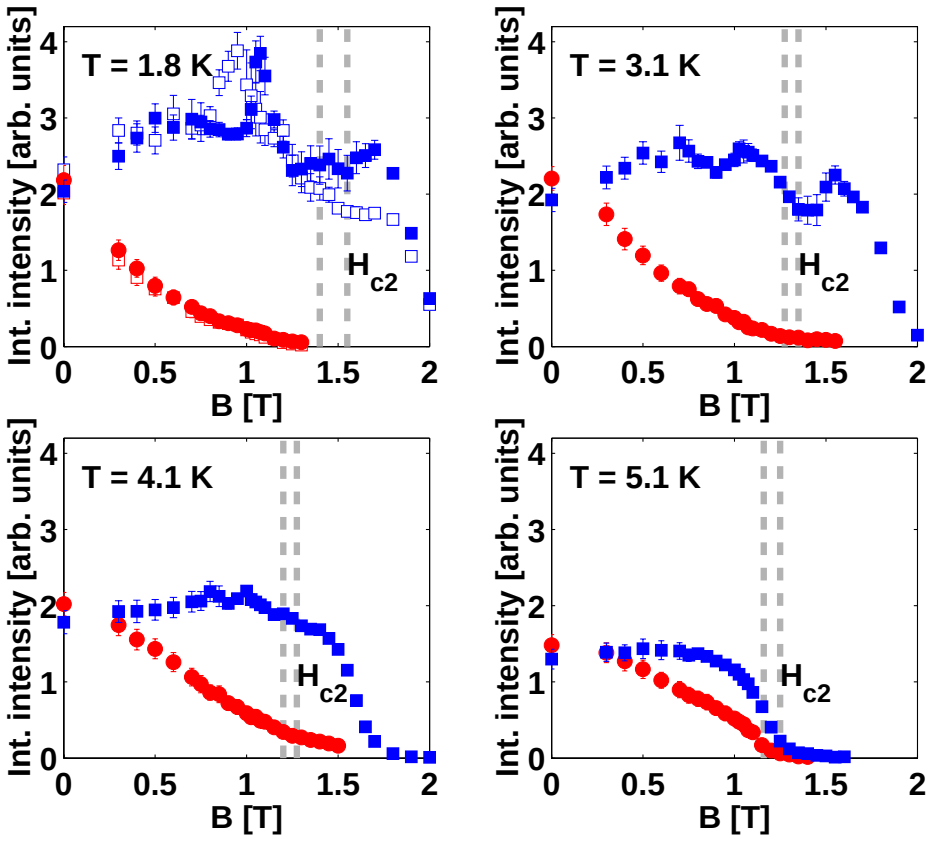

Figure 12. Integrated intensities of the magnetic reflections of the majority $\mathbf{Q}_N^A$ *domain measured in h-scans at* $(2-Q, 0, 0)$ *(squares) and of the minority* $\mathbf{Q}_N^B$ *domain measured in k-scans at* $(0, 2-Q, 0)$ *(circles), as functions of a field applied along* [010]. *The solid symbols represent the data obtained when increasing the field, and the open ones show the decreasing-field data. (Hysteresis is examined only for the* 1.7 *K data). The upper critical field for superconductivity is marked by dashed lines, taken from figure 2 and 3 in reference [47].*

In order to determine which magnetic phase is present at the different values of the field, we need to know the experimental accuracy. All the presented positions are the measured values, corrected for the position of the nuclear Bragg peak. The $\frac{4}{7} = 0.5714$ structure, which is the most stable field-induced structure because of its small number of layers in one commensurable period, has an experimental value of Q in the interval 0.5725–0.5730, determined by two Gaussian fits, see

figure 10. This indicates a systematic error in the determination of Q of 0.002 in addition to the random one of 0.001.

Figure 12 presents the integrated intensities of the $(200) - \mathbf{Q}_{\mathrm{N}}^{\mathrm{A}}$ and $(020) - \mathbf{Q}_{\mathrm{N}}^{\mathrm{B}}$ magnetic reflections. The intensities are evaluated as the product of the amplitude and the width of the one-Gaussian fits. Numerical integrations or the two-Gaussian fits lead to the same results. The variation of the intensity is probably much affected by extinction: In zero field, the two domains are equally populated, but when one domain is suppressed not all the intensity will appear in the other domain, because the intensity of the larger domain is more affected by extinction. This may explain the decrease of total intensity between 0 and 1.0 T, which is observed for all temperatures. At 1.0 T and 1.8 K (upper left panel), the total intensity is temporarily regained, which may reflect a reduction of extinction due to the presence of random domains with $Q = 0.572$ and $Q = 0.588$. At 3.1 K, there is also a peak in the intensity around 1.0–1.1 T, but much less pronounced. Above 1.2–1.3 T and below 1.8 T in the low temperature plot, the total intensity is roughly constant, and in this range the system consists of only a single domain with a certain Q, and the minority $\mathbf{Q}_{\mathrm{N}}^{\mathrm{B}}$ domain has disappeared. Above 1.8 T, the intensity is reduced by the magnetic field until at 2.0–2.2 T the antiferromagnetic ordering is completely quenched.

Hysteresis

The results at 1.8 K in figures 11 and 12 are obtained both for increasing and decreasing values of the field. In the case of the majority domain, the hysteresis in the intensity and in the position of the magnetic Bragg peak are concordant with each other. The hysteresis shown by the first-order transitions between different commensurable values of Q, is an independent measure for the tendency of the period of the magnetic structure to lock-in to the commensurable values. A detailed neutron-diffraction analysis [49] and the magnetization measurements show that the transition to the saturated paramagnetic state at about 2.0 T is of first order, and the smaller intensity observed between 1.5–2.0 T when reducing the field, is consistent with this first-order nature of the transition. The intensity due to the minority $\mathbf{Q}_{\mathrm{N}}^{\mathrm{B}}$ domain shows no hysteresis. This is highly surprising. The minority domain was anticipated to be metastable in a field, and after being eliminated completely at high fields, we expected this domain to be energetically unfavorable, until the applied field was reduced to less than $\sim$0.1 T. The critical field for the stability of the $\mathbf{Q}_{\mathrm{N}}^{\mathrm{B}}$ domain has been followed at higher temperatures (measured for increasing values of the field). It is about 1.3 T at 1.8 K and increases to about 1.4–1.6 T, when the temperature is 3.1 and 4.1 K, until it finally starts to decrease when the temperature approaches T_{N} (it is still about 1.2 T at 5.1 K). This critical field is somewhat uncertain to determine, but, clearly, it does not decrease with temperature in the same fashion as the critical field for the $\mathbf{Q}_{\mathrm{N}}^{\mathrm{A}}$ domain.

Details of width, amplitude and background

Figure 13 presents details of the width and amplitude of the Gaussian fits to the magnetic reflections of the majority $\mathbf{Q}_{\mathrm{N}}^{\mathrm{A}}$ domain measured in h-scans at $(2-Q, 0, 0)$ (squares) and of the minority $\mathbf{Q}_{\mathrm{N}}^{\mathrm{B}}$ domain measured in k-scans at $(0, 2-Q, 0)$ (circles), as functions of a field applied along [010]. Notice, near the transitions from

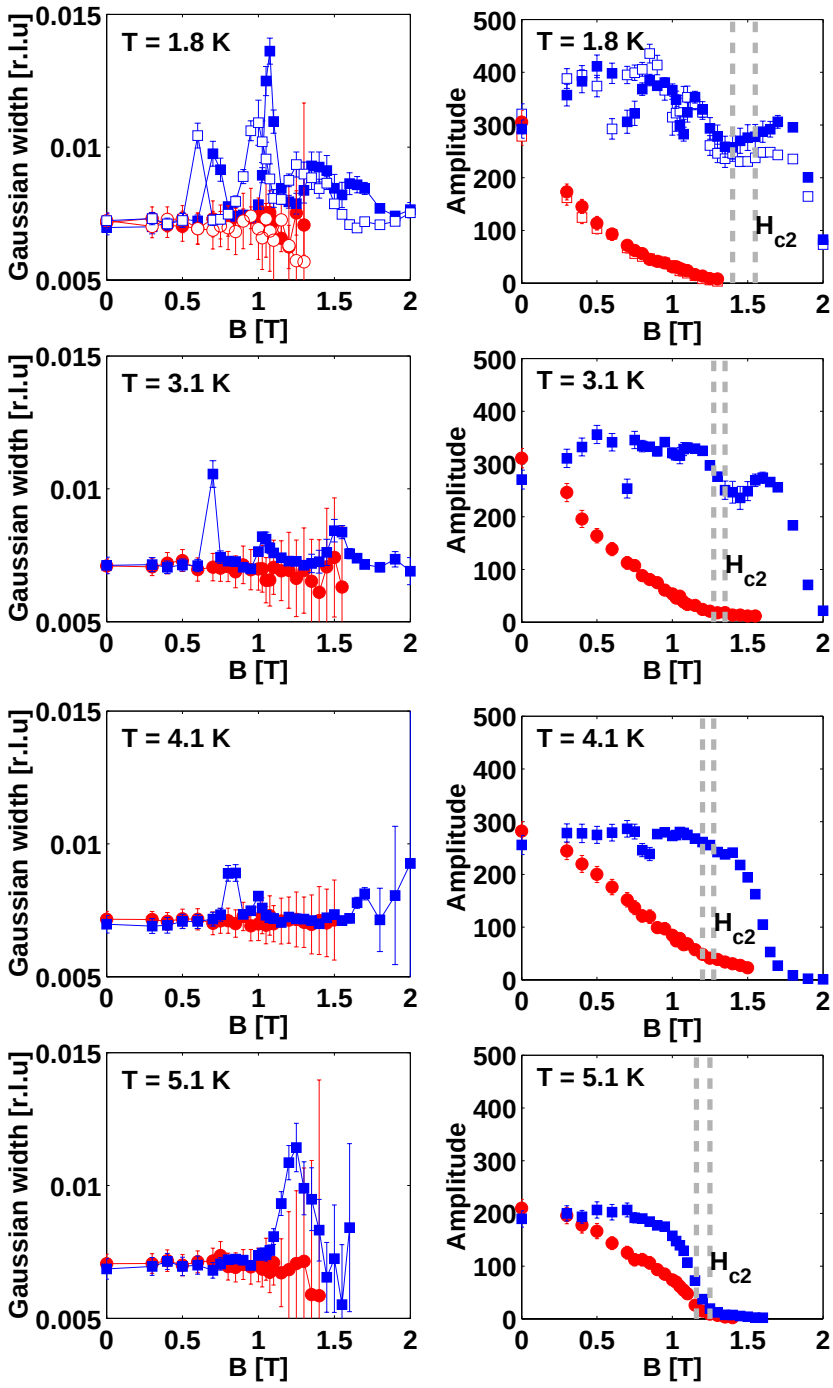

Figure 13. Gaussian fitted width (left panels) and amplitude (right panels) of the magnetic reflections of the majority $\mathbf{Q}_N^A$ *domain measured in h-scans at* $(2-Q,0,0)$ *(squares) and of the minority* $\mathbf{Q}_N^B$ *domain measured in k-scans at* $(0,2-Q,0)$ *(circles), as functions of a field applied along* $[010]$*. The solid symbols represent the data obtained when increasing the field, and the open ones show the decreasing-field data. The amplitude is the maximum number of neutron counts in* 5000 *monitor counts which corresponds to approximately* 15 *minutes.*

one magnetic period to another, the width of the one-Gaussian fit increases dramatically by up to 100%. In the experiments on $ErNi_2B_2C$ the width is resolution limited. Examining the zero field Gaussian width (Gw) in order to estimate the minimum domain size yields: $\Delta Q = Gw \cdot 2\sqrt{2\ln 2} \cdot \frac{2\pi}{a} = 0.0297\text{Å}^{-1}$ FWHM, and the lower limit of the coherence length is given by $\frac{2}{\Delta Q} = 67$ Å.

In some field regions many small peaks appear in the Q range of $0.54 - 0.63$, and as an example, the left part of figure 14 presents scans at 0 T, 1.1 T, 1.15 T, and 1.3 T, with the insert showing in detail these small peaks located around a main peak. Also it can be seen in figure 8 in the 1.4 T data. A way to quantify these many small peaks, is to fit one Gaussian to the main peak and regard the background determined in the fit as a measure for the average amplitude of the small peaks. The right part of figure 14 shows the fitted background at T = 1.8 K in increasing fields. It is clear that this phenomenon of many small peaks only appears in the field interval of 1 T to 1.6 T, however, notice that exactly at B = 1.15 T the background is flat, this can be seen in both panels of figure 14. The appearance of many small peaks is an indication that the energies of the different structures are very close, specifically in this field range. At 1.4 T where the background peaks, the structure starts to revert to lower Q values.

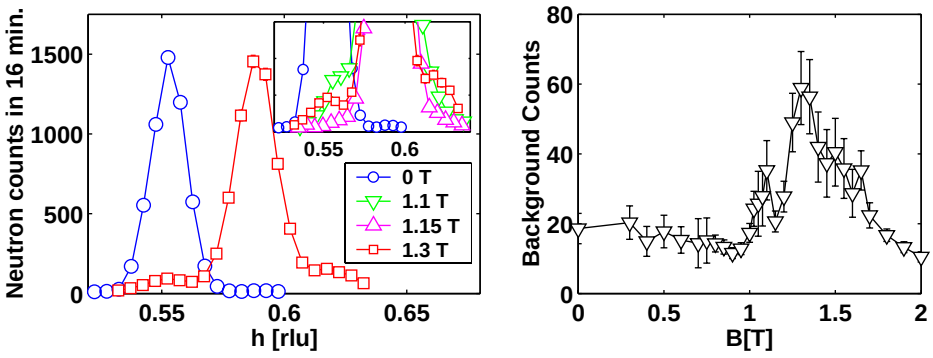

Figure 14. Left panel: $[h00]$ *scans through the* $(2-Q,0,0)$ *reflection at* 0 *T,* 1.1 *T,* 1.15 *T, and* 1.3 *T. Notice the higher background in the* 1.3 *T data, which is shown more clearly in the insert. Here it is obvious that at* 1.3 *T there are three peaks: one at* 0.55 *rlu, a main peak at* 0.59 *rlu and one at* 0.62 *rlu. In the right panel the background obtained when fitting one Gauss to the peak is presented. Between* 1 *T and* 1.6 *T it is clear that the background is increased. This is the same field region where* Q *is larger than* 0.57.

5.3 Results: Field along [110]

In the case where the field is along [110], the two domains are degenerate, and we observed essentially the same intensities for the magnetic peaks at $\mathbf{Q}_N^A$ and $\mathbf{Q}_N^B$ both in zero field and in an applied field. A detailed field and temperature survey was performed for the $(110) - \mathbf{Q}_N^A$ magnetic reflection. Three different peak positions of the magnetic structure appear as the magnetic field is increased. Figure 15 shows $[h10]$ scans through the $(110) - \mathbf{Q}_N^A$ reflection at various values of the field at $T = 1.8$ K, which represents the three periods of magnetic structure at $h = 0.448$, 0.428, and 0.419 corresponding to $Q = 0.552$ ($\frac{11}{20}$ or $\frac{16}{29}$), 0.572 ($\frac{4}{7}$), and 0.581 ($\frac{18}{31}$ or $\frac{11}{19}$). At low fields $Q = 0.552$, with a slight increase to $Q = 0.555$

between 0.5 T and 1 T. At 1 T the reflection is divided into two peaks, one at $Q = 0.555$ and one at $Q = 0.572$. Gradually, all the intensity is shifted to the $Q = 0.572$ reflection and at 1.5 T part of the intensity shifts to $Q = 0.581$. For B = 1.6 T and 1.7 T all the intensity lies in the 0.581 reflection, but at 1.8 T a reappearance of the 0.572 reflection is observed. Both peaks decrease gradually in intensity until they disappear at 2.1 T.

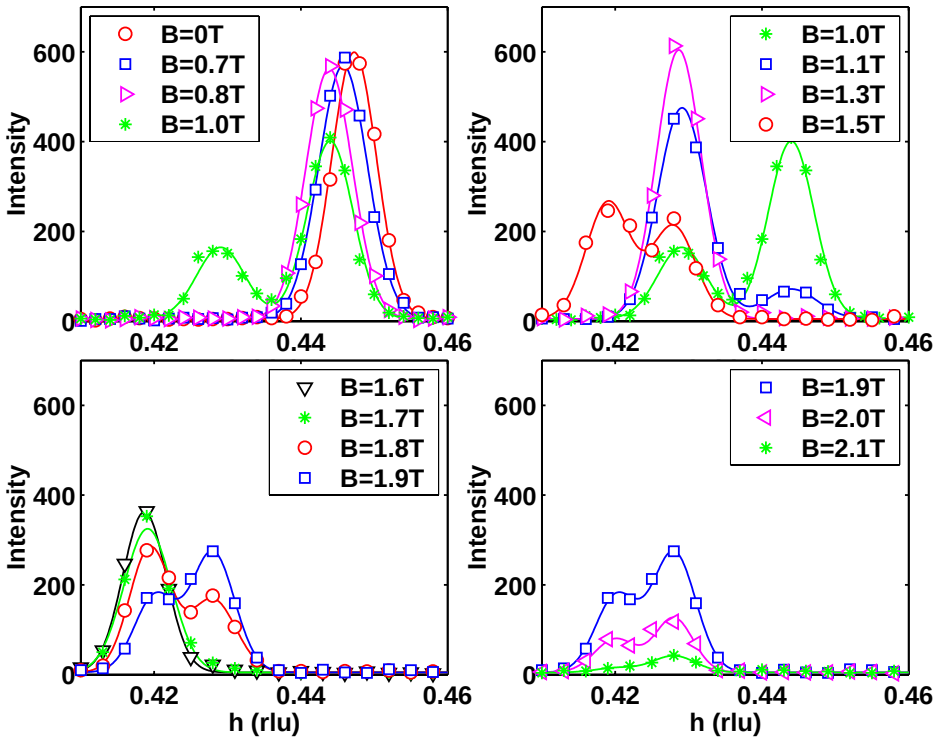

Figure 15. Field along [110]*:* [*h*10] *scans of the* (110) − $\mathbf{Q}_N^A$ *reflection in increasing fields and at* $T = 1.8$ *K. The lines are Gaussian fits to one or two peaks.*

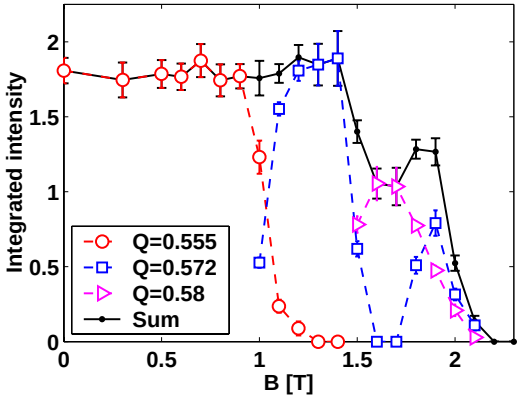

Figure 16. Integrated intensity of the (110) − $\mathbf{Q}_N^A$ *reflection at different peak positions versus field at* $T = 1.8$ *K. Solid black markers indicate the sum of integrated intensity in all peaks.*

Notice the intensity at 1.6 T is dramatically lower than the zero field intensity, only 40 % of the zero field intensity is measured at 1.6 T. The integrated intensity of the magnetic reflection was determined by fitting one, or, if two phases are present at the same time, two-Gaussian functions to the data points, and the result is presented in figure 16.

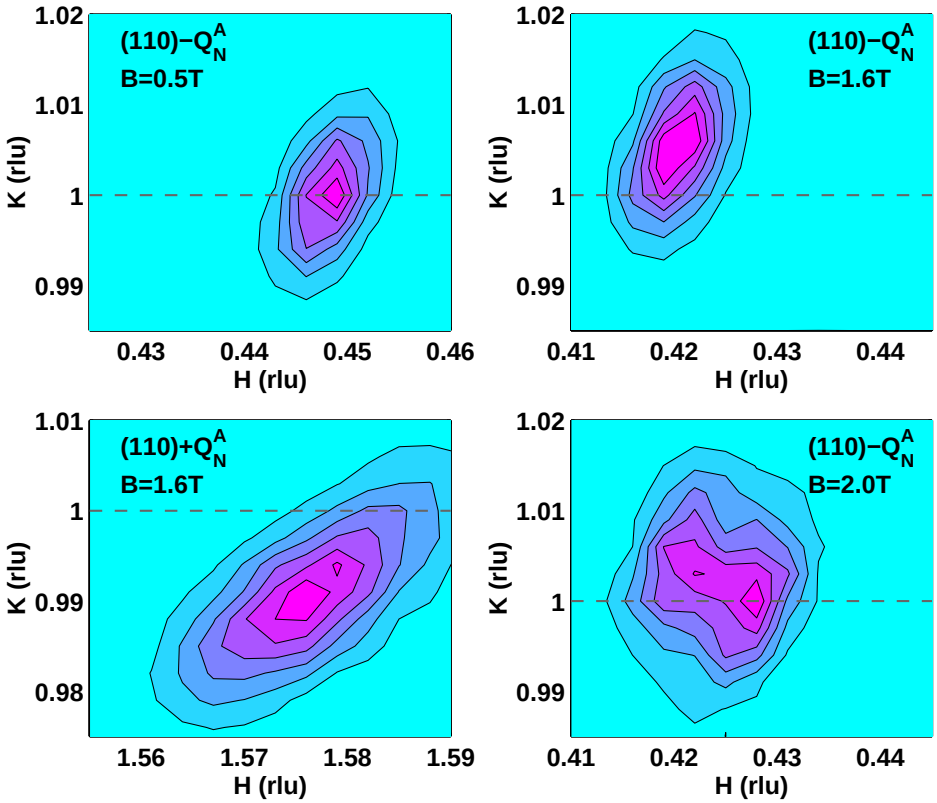

Figure 17. Grid scans of the $(110) \pm \mathbf{Q}_N^A$ *reflection at* $T = 1.8$ *K in increasing fields.*

In order to figure out where the missing intensity could be, we measured numerous grid scans of the $(110) - \mathbf{Q}_{\mathrm{N}}^{\mathrm{A}}$ reflection. These show the appearance of a small orthogonal component of the modulation vector around B = 1.6 T. Grid-scans of the magnetic reflection at several fields are presented in figure 17. At a field of 0.5 T the $(110) - \mathbf{Q}_{\mathrm{N}}^{\mathrm{A}}$ reflection lies at $(h, k) = (0.448, 1)$ whereas at 1.6 T it lies at $(h, k) = (0.420, 1.005)$. In the lower left panel the $(110) + \mathbf{Q}_{\mathrm{N}}^{\mathrm{A}}$ reflection is shown at 1.6 T, and here $(h, k) = (1.577, 0.993)$. Notice in the lower right panel the 0.57 and 0.58 structures coexist at $B = 2$ T, and that only the 0.58 part of the peak is rotated, whereas the 0.57 structure stays in the symmetry direction. Thus we conclude that $\mathbf{Q}_{\mathrm{N}}^{\mathrm{A}}$ changes from $(Q, 0, 0)$ to $(Q, \delta Q, 0)$, with δQ in the interval of [-0.004,-0.007]. Clearly, the presence of the finite orthogonal component explains the observed reduction of the integrated intensity of the $[h10]$ scan at 1.6 T in Fig. 15. We regain 94% of the zero-field intensity at this position. An analysis of the magnetic reflection at $(110) + \mathbf{Q}_{\mathrm{N}}^{\mathrm{A}}$ was performed at several values of field and temperature in order to check for consistency. The finite orthogonal component also appears at the magnetic peaks $(110) - \mathbf{Q}_{\mathrm{N}}^{\mathrm{B}}$ and $(000) + \mathbf{Q}_{\mathrm{N}}^{\mathrm{B}}$, giving $\mathbf{Q}_{\mathrm{N}}^{\mathrm{B}} = (\delta Q, Q, 0)$. The value $\delta Q \approx -0.005$, corresponding to a rotation of $\mathbf{Q}$ by

$\delta\theta = \arcsin(\frac{0.005}{0.58}) = 0.5°$, is a typical one, and the largest negative value observed is $\delta Q \approx -0.007$. Whenever δQ is non-zero, in the $\mathbf{Q}_{\mathrm{N}}^{\mathrm{A}}$ or the $\mathbf{Q}_{\mathrm{N}}^{\mathrm{B}}$ domain, it is negative. This corresponds to a rotation of $\mathbf{Q}$ away from the direction of the magnetic field, corresponding to a rotation of the transverse component of the modulated moments towards the direction of the field. The last option assumes that the structure maintains the transverse configuration when the propagation direction is changed. At first sight, one could say that in this highly anisotropic system it is unlikely that the moments rotate away from a crystalline axis however, the only motivation for the structure to rotate is the gain in Zeeman energy by rotating the moments towards the field direction.

In order to be sure of the alignment of the spectrometer, nuclear scans are presented in Fig. 18. The first order (200) reflection lies in the blind angles of the cryostat, so instead the (100) reflection was examined with second order neutrons. The left panel presents a transverse omega scan, which is equivalent to a k-scan. The center should be at omega = 20.23°, and it is found to be only 0.03° of. In the right panel, a longitudinal h-scan is presented, showing that the alignment in the h direction is performed within an accuracy of 0.002 rlu.

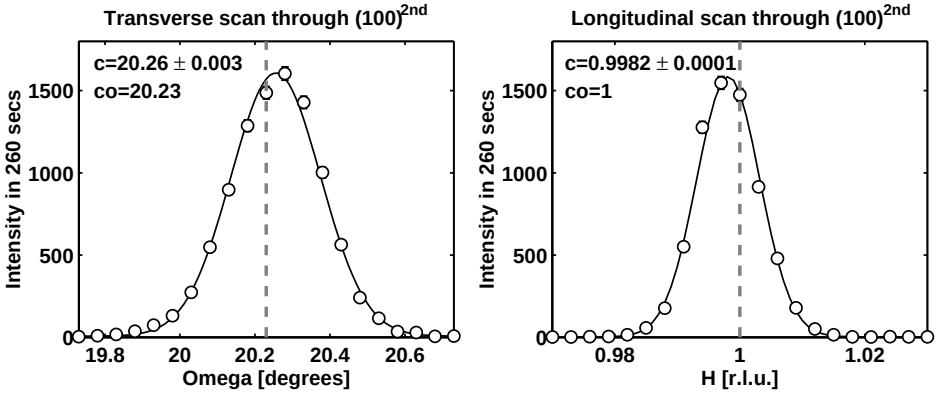

Figure 18. Transverse (left panel) and longitudinal (right panel) scan of the (200) *reflection, measured with second order neutrons at the* (100) *position at* $T = 2.0$ *K. The co values are the values of the perfectly centered reflection. This check is performed after grid scans of the* $(0.55, 0, 0)$, $(0, 0.55, 0)$, *and* $(0.45, 1, 0)$ *reflections, at* 1.5 T *which all show a clear rotation of the* Q *vector.*

The (110) nuclear Bragg peak could be reached with first order neutrons, and the position of this reflection was examined regularly before and after grid scans at different fields. It does not show any change of position as a function of field.

The plots in Fig. 19 show the characteristic variation patterns with field of the principal component Q of the modulation wave vector at all measured temperatures. Some of the scans were shown in Fig. 15, and the position is determined by fitting one or two Gaussian functions to the results. Open circles represent points where the value of δQ is not known, because no grid scan is performed. The Q value is marked by open or colored squares in the respective cases of $\delta Q = 0$ or $\delta Q < 0$: yellow: $\delta Q = -0.002$, cyan: $\delta Q = -0.003$, green: $\delta Q = -0.004$, red: $\delta Q = -0.005$, blue: $\delta Q = -0.006$, and black: $\delta Q = -0.007$

First, lets consider the low field behavior. At 1.8 K, the structure changes gradually from $Q = 0.552$ ($\frac{11}{20}$ or $\frac{16}{29}$) to $Q = 0.555$ ($\frac{5}{9}$) between 0.5 and 1 T. When increasing the temperature the same picture emerges, only the transition becomes

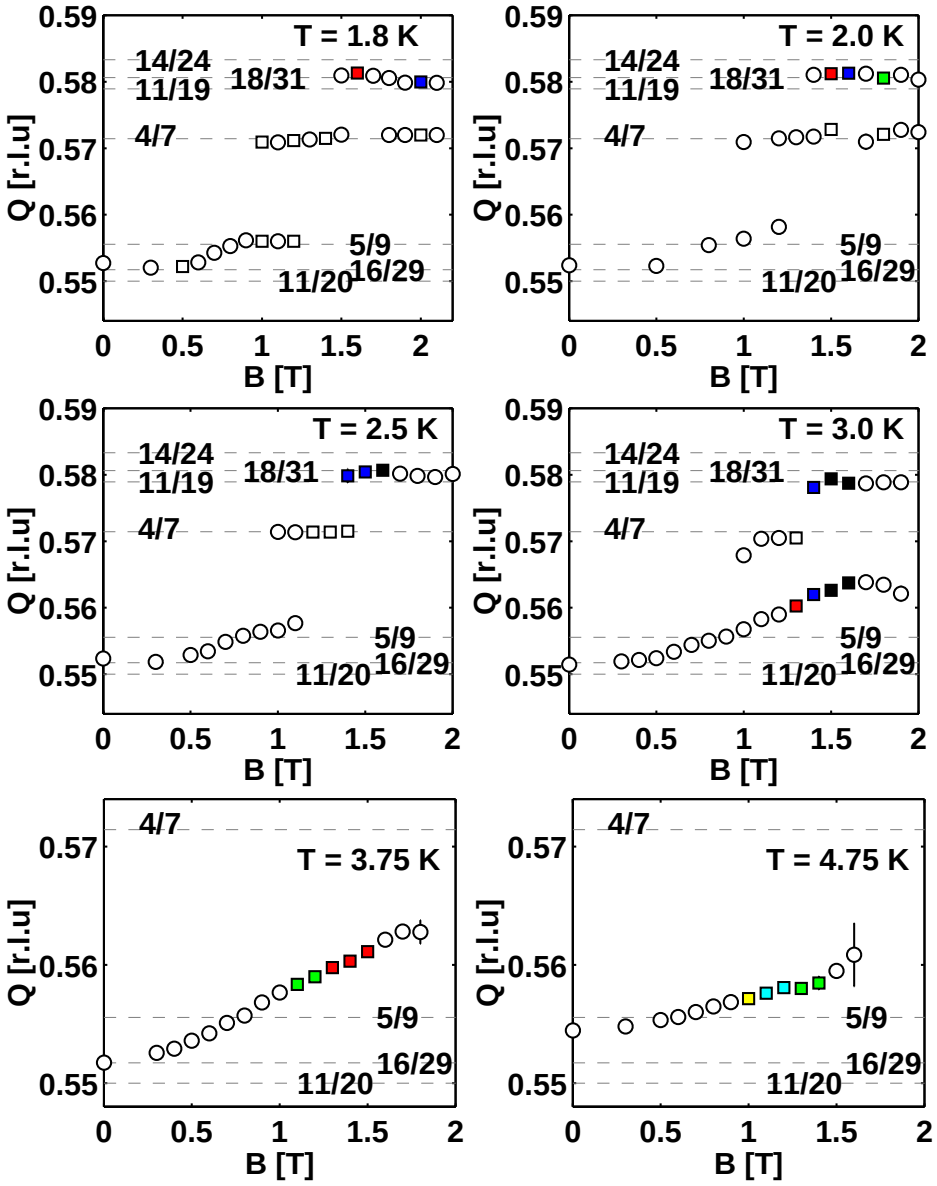

Figure 19. Field along [110]*: The field dependence of the value of* Q *of the* (110)-$\mathbf{Q}_N^A$ *reflection at all measured temperatures. Notice when* $\mathbf{Q}$ *is on the high symmetry* h*-axis the* Q *value is marked by open squares, open circles represent points where only one* h*-scan with* k*=1 was performed, so* δQ *is unknown. When* $\mathbf{Q}$ *is rotated away from the* h*-axis, the* Q *value is marked by colored squares: yellow:* $\delta Q = 0.002$*, cyan:* $\delta Q = 0.003$*, green:* $\delta Q = 0.004$*, red:* $\delta Q = 0.005$*, blue:* $\delta Q = 0.006$*, and black:* $\delta Q = 0.007$*.*

more and more smooth, until at 4.75 K, where the zero field structure is very close to $Q = 0.555$. In the following, the zero and low field structures are treated as one phase and the more drastic changes in structure when applying a field are discussed.

Generally, for temperatures below 3 K, the zero field magnetic structure with Q in the interval of [0.55,0.56] persists up to 1 T, where it changes into the the

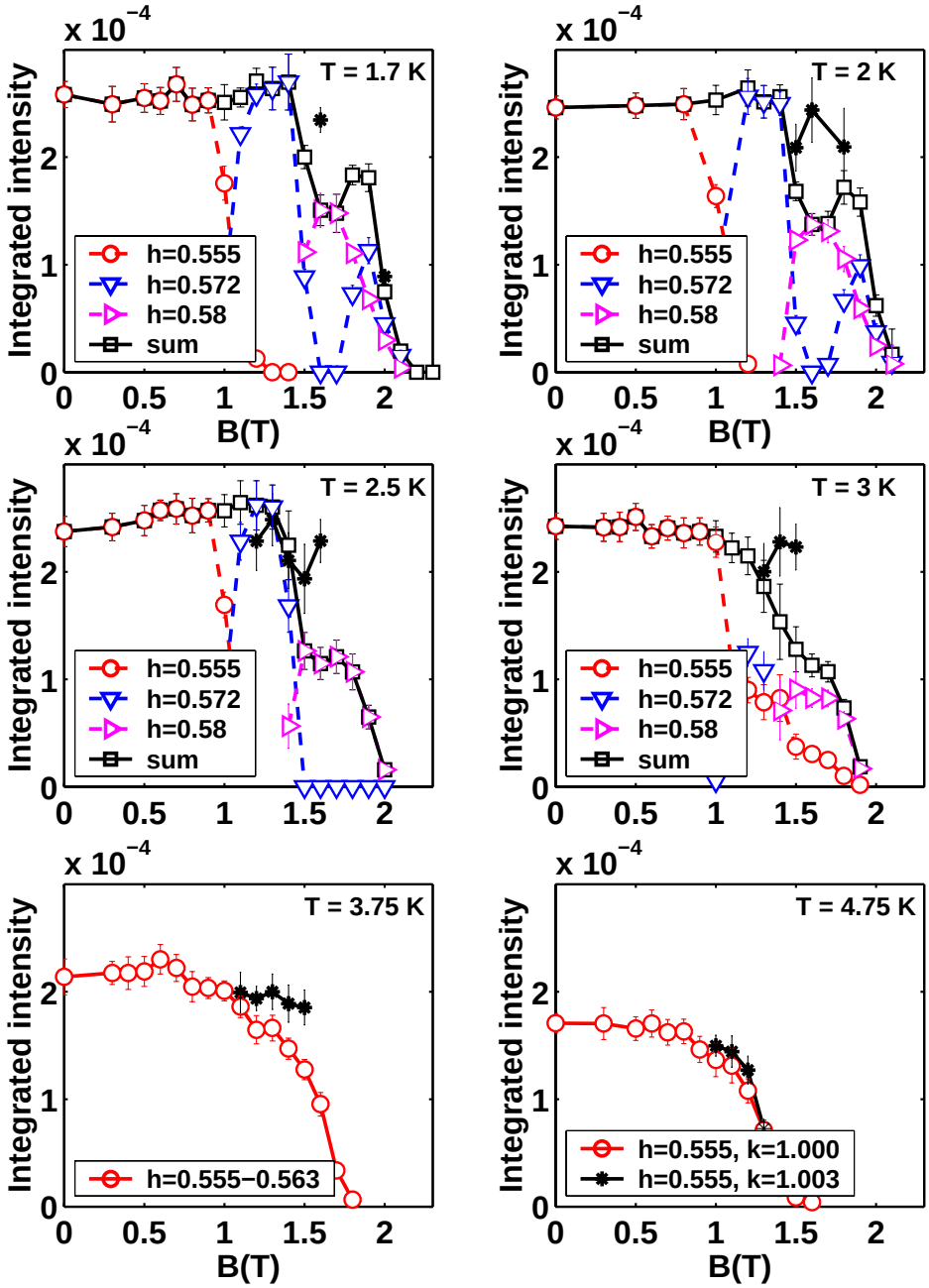

Figure 20. Field along [110]*: The field dependence of the integrated intensity of the* (110)-$\mathbf{Q}_N^A$ *reflection at all measured temperatures. The integrated intensity is evaluated as the product of the amplitude and width the individual peaks in the two-Gaussian fits. The total intensity is marked by black squares, and the black stars indicate the total intensity obtained in a scan where* $k = 1.003$ *or* $k = 1.006$*. This could only be done for the fields and temperatures where a grid scan was performed, which determined the extend of rotation of the reflection.*

$Q = \frac{4}{7}$ structure and at 1.4 T or 1.5 T it is replaced by a Q value of 0.581 ($\frac{11}{19}$ or $\frac{18}{31}$). In the upper panels, for T = 1.8 K and T = 2 K the $\frac{4}{7}$ structure reappears at 1.7 T or 1.8 T in coexistence with the $Q = 0.581$ structure up to 2.0 T. At 2.5 K the 0.581 structure persists as a single phase up to the transition to the field-induced ferromagnetic phase and at 3 K the $Q = 0.581$ phase coexists above 1.4 T with the zero field phase that has changed gradually from $Q \approx 0.55$ to $Q \approx 0.56$. In the lower panels, for T = 3.75 K and T = 4.75 K, only the zero field phase is observed and the value of Q increased gradually from 0.552 to 0.563 (T = 3.75 K) and 0.560 (T = 4.75 K). Notice the rotation of $\mathbf{Q}$ takes place in the 0.58, 0.55 and 0.56 structures above some critical field, whereas the $\frac{4}{7}$ structure with the short commensurable period of seven layers, has $\delta Q = 0$ at all fields and temperatures where it is observed.

Figure 20 presents integrated intensities of the magnetic reflection at (110)-$\mathbf{Q}_{\mathrm{N}}^{\mathrm{A}}$ at all examined temperatures, evaluated from Gaussian fits to h scans with $k = 1$. The figure presents the intensity of the magnetic reflections at the various Q values, which was presented in figure 19. The total intensity of the peaks at different Q values is plotted as black squares, and at T = 1.7 K, T = 2.0 K, and T = 2.5 K, a jump in the intensity at the field where $\mathbf{Q}$ rotates is observed. For T = 3.0 K, the structure is rotated at least for B = 1.3 T to B = 1.6 T, but here the intensity shows only a smooth change of slope at 1.3 T, where we know that the structure is rotated. In the lower panels for T = 3.75 K and T = 4.75 K, the reflection is rotated at least above 1.1 T and 1.0 T respectively, and the intensity is smooth in the entire field range. Black stars represent the integrated intensity of the rotated reflection, obtained from a scan away from the $k = 1.000$ symmetry direction. The grid scans were performed with intervals in k of 0.003, so the intensity is evaluated from h scans at $k = 1.003$ or $k = 1.006$, dependent on which of the scans yield the center of the rotated reflection. For T = 1.7 K, the intensity at 1.6 T of the $k = 1.006$ scan is much larger than the one at $k = 1.000$, however, for B = 2.0 T, almost no gain in intensity is observed. The grid scan for B = 2.0 T and T = 1.8 K was presented in figure 17, where it is clear that two peaks appear in the grid scan, one with $Q = 0.428$ and $\delta Q = 0$, and one with $Q = 0.422$ and $\delta Q = -0.006$, and that the main part of the intensity lies in the $\frac{4}{7}$ structure, which is on the axis.

5.4 Results: Field along $[110] + 22.5^\circ$

In order to acquire more information about the unusual rotation of the magnetic ordering wave vector, we have examined the behavior of the magnetic reflections, when applying the field along a direction half way in between the [010] and [110] directions. We performed grid scans of the magnetic reflections at $(110) - \mathbf{Q}_{\mathrm{N}}^{\mathrm{A}}$ and $(110) + \mathbf{Q}_{\mathrm{N}}^{\mathrm{B}}$ at base temperature in increasing fields, and the results are summarized in Fig. 21. The case $(1 - Q, 1, 0)$ shows the behavior of the $\mathbf{Q}_{\mathrm{N}}^{\mathrm{A}}$ majority domain, and the grid scans determine the positions of the magnetic reflection to lie between 0.551 to 0.585. No rotation of the magnetic reflection is detected in this domain. Two transition fields are observed at 0.8 T and 1.2 T consistent with the magnetization data [11]. In the minority $\mathbf{Q}_{\mathrm{N}}^{\mathrm{B}}$ domain, indicated by $(1, 1 + Q, 0)$ on the figure, Q changes from 0.550 to 0.553, and, most interestingly, the orthogonal component of the modulation vector is observed to become non-zero, $\delta Q \approx -0.005$, at fields larger than 1.2 T. At 1.0 T and 1.1 T a small rotation of +0.001 rlu is detected, however, since the alignment of the spectrometer is performed within an

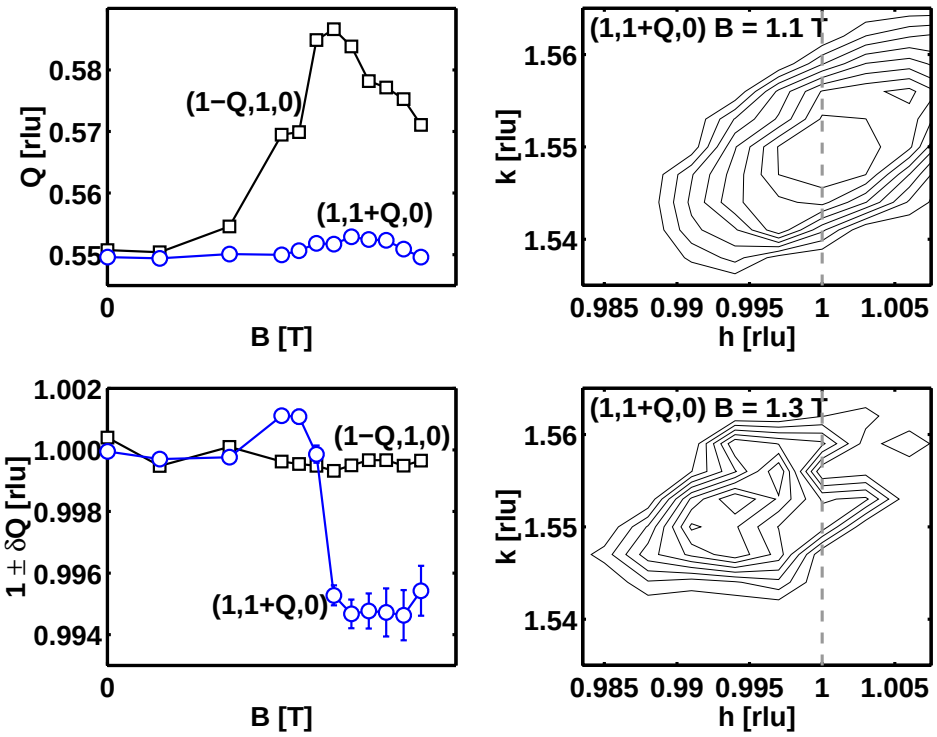

Figure 21. Field along $[110] + 22.5°$ *at* $T = 1.75$ *K: The position of the magnetic reflection of the majority (squares) and minority (circles) domains are presented in the left part of the figure. Top: principal periodic modulation* Q*, and bottom: orthogonal component* $1 \pm \delta Q$*. The right part of the figure presents two grid scans of the minority domain showing that* $\delta Q = 0$ *at* 1.1 *T and* $\delta Q \approx -0.005$ *at* 1.3 *T.*

accuracy of 0.001 rlu, it might simply be due to a field dependent systematic error of the spectrometer. Thus, we cannot say if this is an artifact or of it is indeed a true effect.

The magnetic structure in the majority domain behaves roughly in the same way as observed when the field is applied along [010]. In the minority domain the value of Q is nearly constant, as when the field is applied along [010]. The domain is reasonable stable also at high fields, the intensity is still about 20% of the zero-field value at 1.8 T, and, like in the case of field along [110], **Q** is rotated at fields above 1.2 T (at 1.75 K). The orthogonal component δQ not only has the same sign, but also the same magnitude as in the [110] case.

5.5 Results: Field along [001]

In this section, the magnetic structure of $ErNi_2B_2C$ is examined when applying the magnetic field along the [001] direction, which is the hard axis of magnetization. Figure 22 summarizes the results, the result is in short that nothing much happens. The left panel presents scans of the magnetic 1^{st} order reflection in increasing fields at T = 1.9 K. The scans for 0 T and 5 T are almost identical, and when the field is increased further the Q value shifts gradually towards larger Q, and the intensity starts to decrease. The middle panel presents the value of Q versus field, obtained by fitting a Gaussian to the scans presented in the left panel, here it is seen that

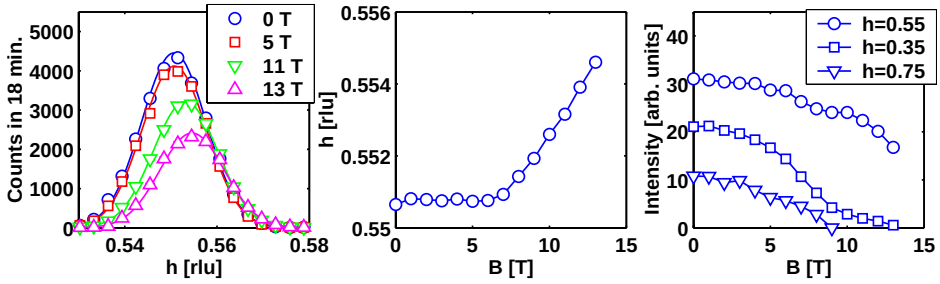

Figure 22. Left panel: Scans of the magnetic reflection at $Q = 0.55$ in increasing fields, $T = 1.9$ K. Middle panel: Position of the magnetic reflection obtained from Gaussian fits to scans as the ones presented in the left panel. Right panel: Integrated intensity of 1^{st} (circles), 3^{rd} (squares) and 5^{th} (triangles) orders of the magnetic reflection. All errorbars are smaller then the markers.

Q changes from 0.551 to 0.555 when the field changes from 0 T to 13 T. The right panel presents the integrated intensities obtained from the Gaussian fits to the 1^{st} (circles), 3^{rd} (squares) and 5^{th} (triangles) orders of the magnetic reflection. The 3^{rd} and 5^{th} order intensities decreases around 8 T, whereas the 1^{st} order intensity is roughly constant up to 10 T, whereafter it starts to decrease and it is approximately $\frac{2}{3}$ of the zero field value at 13 T. Thus the magnetic structure is less squared up, approaching a sine wave above 8 T.

5.6 Results: Higher order reflections

So far the analysis of the magnetic structures in $ErNi_2B_2C$ in an in-plane magnetic field has been concentrated on the behavior of the first order reflection, however much important information lies in the higher order reflections: The size of the odd order reflections reveals the squaring up of the structure and the size of the even order reflections reveals the weak ferromagnetic moment of the structure.

Figure 23 presents several scans of the magnetic reflections at T = 2.1 K, for the field applied along [010]. The blue circles in the top panel is the zero field scan, where all the odd order reflections up to ninth order are visible. In our samples we do not see the even order reflections from the weak ferromagnetic structure in zero field, which was observed by Choi and co-workers in 2001 [25]. The even order reflections occur when a small magnetic field is applied in any direction within the *ab* plane. The red circles are taken for $B = 1$ T, and even though only three peaks are visible, actually these are all the possible reflections for the $\frac{4}{7}$ structure because the reflections overlap as indicated in the figure. The 6^{th} and 8^{th} order reflections overlap with the first order reflections, and the 7^{th} order reflection ends up at the even numbered nuclear reflections.

When the field is increased, the ordering vector changes to $Q = 0.59$, thus here it is possible to separate the higher order reflections, and for the first time we see directly the even order reflections. One strange feature is the very small peak at the [100] nuclear position at $B = 1.3$ T, which is forbidden in the tetragonal (and also in the orthorhombic) symmetry. In a paper by Bancroft and co-workers a similar peak can be seen in a figure, also only at $B = 1.3$ T. I do not have an explanation for the origin of this peak, nor has Bancroft *et al.* since they do not even mention the peak in the text of their paper [50].

Increasing the field further, the higher order reflections die out, and at 1.75 T,

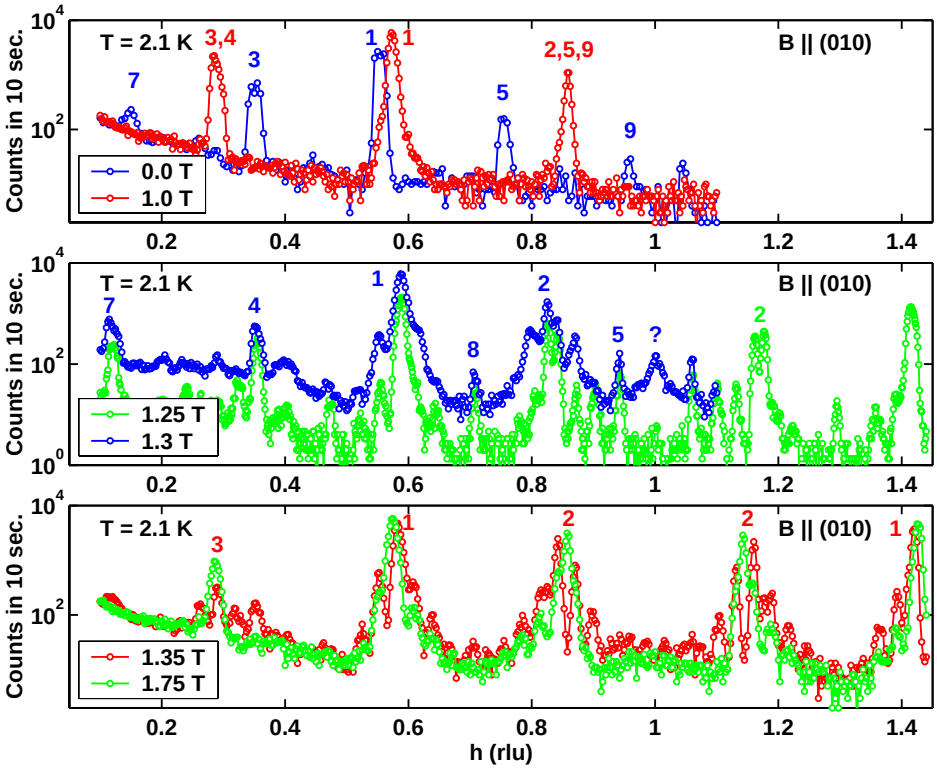

Figure 23. Scans of reflections along $(h00)$*, for* $B \parallel [010]$*,* $T = 2.1$ *K in increasing fields.*

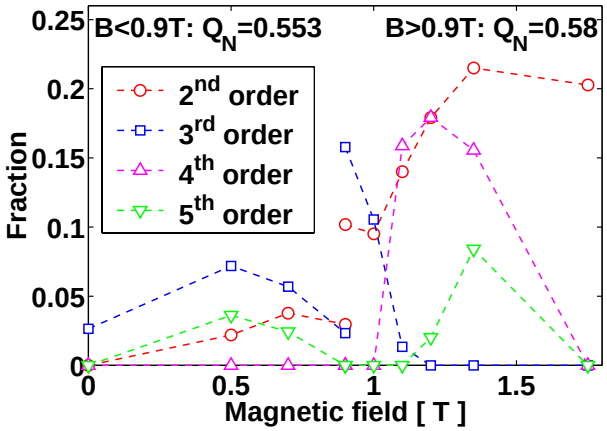

Figure 24. Relative intensities of magnetic higher order reflections relative to the first order intensity. The intensity of the 4^{th} *and* 5^{th} *order reflections are multiplied by* 10*. Measured in increasing fields along* [010] *for* $T = 4$ *K.*

only the 1^{st}, 2^{nd}, and 3^{rd} order reflections are present.

Figure 24 gives an overview of the intensities of the higher order reflections relative to the first order reflection. Notice that the relative intensities of the 4^{th} and 5^{th} order reflections are multiplied by 10. Firstly, one notices that there is a jump in the 2^{nd} and 3^{rd} order intensities at 0.9 T, which is connected to the change of ordering vector from $Q = 0.553$ to $Q = 0.58$. Secondly, there is a jump

in the 2^{nd}, 4^{th}, and 5^{th} order intensity at 1.1 - 1.3 T, at the same time, the 3^{rd} order intensity disappears. In total, the even order reflections are strengthened compared to the odd order reflections in increasing fields since the ferromagnetic part is induced by the applied magnetic field.

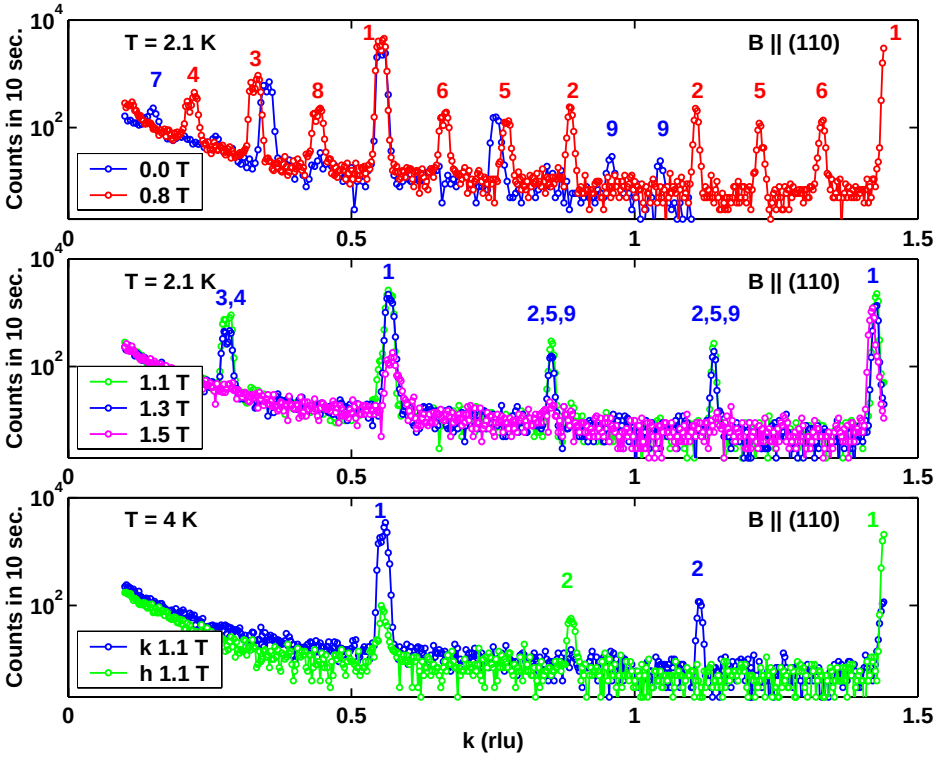

Figure 25. Scans of reflections along $(0k0)$*, for* $B \parallel [110]$*,* $T = 2$ *K. The lower panel presents scans along both* $(0k0)$ *(blue), and along* $(h00)$ *(green) at* $T = 4$ *K and* $B = 1.1$ *T . (The numbers indicate the order of the reflection, with the higher order reflection lying at a nuclear Bragg reflection* $\pm\, x\mathbf{Q}_N$*.)*

Figure 25 presents long scans along $[0k0]$ in increasing fields, $B\|[110]$, and T = 2.1 K. The blue circles in the upper panel is the same zero field scan as in figure 23, and the red circles represent the data taken at 0.8 T. Here $Q = 0.55$, and all the higher order reflections, both odd and even stand out beautifully. Increasing the field changes the structure to the $\frac{4}{7}$ structure and again the reflections overlap. The bottom panel shows a peculiarity observed in the long scans, which initiated all the following experiments on $ErNi_2B_2C$. The blue circles is a scan similar to the ones in the panels above taken at T = 4 K and B = 1.1 T, and this looks like one would expect. Interestingly the green markers represent a $[h00]$ scan performed perpendicular to the other one, and here the 1^{st} order intensity is almost gone at $Q = 0.55$, but there is plenty of intensity in the first order reflection at $(2 - 0.55, 0, 0)$. The second order reflections follows the same pattern where $(0 + 2Q, 0, 0)$ is absent, but the reflection at $(2 - 2Q, 0, 0)$ is there. There is no way the magnetic structure can generate this mismatch in intensity between plus and minus directions, and the only valid explanation is given considering the different resolution at these positions in reciprocal space combined with the rotation of the magnetic structure. With a larger resolution ellipsoid for larger

scattering vectors, the rotation of the Q vector will have less effect. The difference between the two scan directions in the lower panel of figure 25 is probably due to a misalignment of the field.

5.7 Phase diagrams and discussion

Figure 26 presents the magnetization measurements from reference [46]. The jumps in magnetization are plotted in the phase diagrams in figure 5.7 as black circles. The phase diagrams present an overview of the magnetic phases detected when applying the field along the symmetry directions [010], [110], and [001]. The phases, indicated by colors, represent the different commensurable structures, and are our best estimates derived from the temperature variation of the magnetic Bragg peak intensities. Notice, the colors from the neutron diffraction data were applied before adding the black circles for the magnetization data. The superconducting upper critical field is marked by a fine line [47].

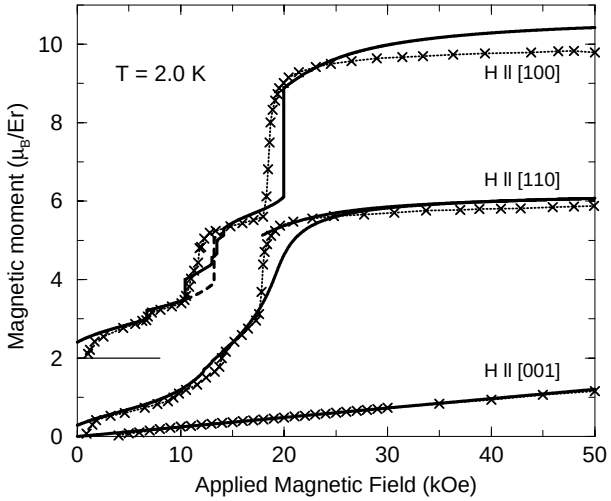

Figure 26. The magnetization curves of $ErNi_2B_2C$ at $T = 2$ K. The crosses connected by dashed lines show the experimental results from reference [46]. The remaining solid and dashed lines show the results calculated by the mean field model [1]. The results in the case of $H \parallel [100]$ have been shifted upwards by 2 units. The figure is taken from reference [23].

Top panel, $H \parallel [010]$

When the field is applied along [010], the domains in which the moments are parallel to the field, or $\mathbf{Q} \parallel [100]$, are the stable ones. This behavior contrasts that of a normal antiferromagnet, however in the present four-state clock system, it is hard to rotate the moments away from the [010] direction, it is much easier to change the magnitude of the moments.

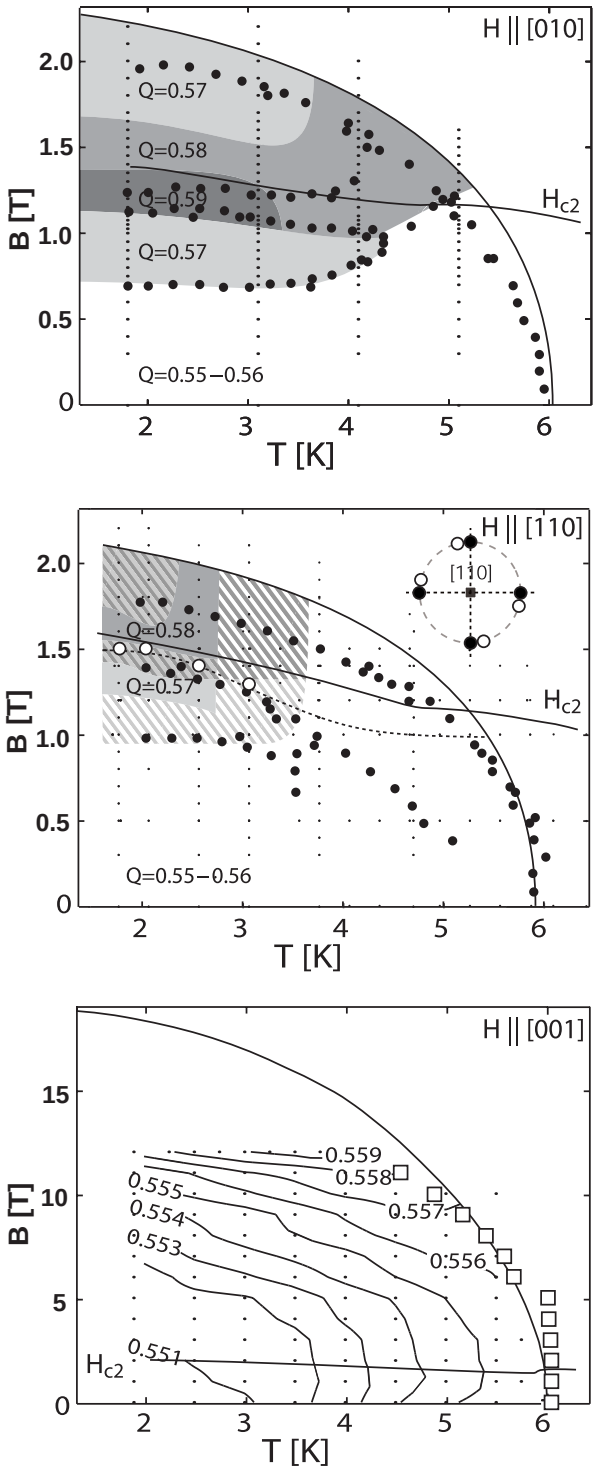

Figure 27. The magnetic phase diagrams of $ErNi_2B_2C$ for increasing values of applied field along [010] (top), [110] (middle), and [001] (bottom). Small black dots mark the (T, H) points where the measurements were made. The outermost boundary in the [010] and [110] cases marks the experimental points where the intensity of the magnetic phase disappears, and in the last case it is the Néel temperature determined by the mean-field model [1]. The superconducting critical field H_{c2} is marked by a fine solid line [47], and the solid circles indicate the magnetic phase lines derived from magnetization measurements [47]. Top, $H \parallel [010]$: Four commensurable phases are presented in the phase diagram. Middle, $H \parallel [110]$: White and gray areas indicate the existence of one of the three phases, and the striped areas represent coexistence of two of the phases. The modulation wave vector has a finite orthogonal component above the dashed line, and the open circles indicate that the orthogonal component is zero at fields below the points. Notice that δQ is always zero if $Q = \frac{4}{7}$, which means that in the top left corner the $Q = 0.58$ structure with $\delta Q \neq 0$ coexists with the $Q = \frac{4}{7}$ structure, which has $\delta Q = 0$. The insert shows schematically how the magnetic reflections are rotated in reciprocal space. Bottom, $H \parallel [001]$: Open squares represent the Néel temperature derived from the data, and the lines are contour plots of the values of Q.

Four commensurable phases are presented in the phase diagram. Starting from low fields, the first two changes of structure match perfectly with the jumps in magnetization measurements at 0.7 T and 1.15 T. The third magnetization jump appears at 1.25 T and does not seem to overlap with the transition from $Q = 0.59$ to $Q = 0.58$, which can be understood considering the nature of the transitions to lower Q values.

A change of Q to larger values is visualized as a spin flip, changing the mixture of sequences $d(5p)$, $d(3p)$, and $d(1p)$ by replacing with smaller number of pairs from 5 to 3 to 1 pair between spin slip planes. When increasing the field above 1.3 T, Q starts to decrease again, but of course the structures maintain their net magnetic moment, which can be seen in the magnetization measurements in figure 26. Thus, the changes of structure appearing above 1.3 T can be ascribed to a change of spin configuration which takes place without altering the net magnetization, and the phase lines for Q changing to lower values will not be observed in the magnetization measurements.

Instead, the model states that the change of double pair configuration $dduu \rightarrow duuu$ (see section 2.6 on page 17) is responsible for the third magnetization phase line (counting the black circles from low field and up at low temperature) appearing at B = 1.2 T – 1.3 T [1]. In principle, this transition should also be detectable in the diffraction experiments by a reduction of the scattering intensity by about 20 % . Unfortunately, the intensity measurements are much affected by extinction (see figure 12 on page 35), and it is not possible to decide, whether this predicted reduction in the intensity occurs or not.

The fourth jump in magnetization is the transition to an almost saturated paramagnetic structure or one could call it a field induced ferromagnetic state. In the magnetization measurements an effort was made to determine the Nèel temperature by correcting for the demagnetization field. In the experiments reported here, the phase line at 2.2 T represents the disappearance of intensity in the neutron diffraction measurements and we have not tried to evaluate the correct Nèel temperature, and this may explain the apparent mismatch of Nèel temperatures. The transition to the field induced ferromagnetic state is of first order, as shown in a detailed neutron diffraction analysis in reference [49]. This leaves the possibility that the demagnetization field smears out the first order transition and stabilizes intermediate structures, which may cause a small antiferromagnetic scattering peak at fields somewhat above the transition field determined from the magnetization measurements.

The most remarkable result obtained in the [010] case is the reversible appearance of the minority $\mathbf{Q}_{\mathrm{N}}^{\mathrm{B}}$ domain, as discussed in subsection 5.2. The stability of the $\mathbf{Q}_{\mathrm{N}}^{\mathrm{B}}$ domain up to a field along [010] of about 1.3 T at 1.8 K cannot be explained by the demagnetization field, which is less than 0.1 T at this field and crystal shape. The (meta)stability of the $\mathbf{Q}_{\mathrm{N}}^{\mathrm{B}}$ domain might be a consequence of the magnetoelastic energy of the different distortion of the two orthorhombic domains. This effect would decline rapidly with increasing temperatures, in contradiction to that the critical field for the $\mathbf{Q}_{\mathrm{N}}^{\mathrm{B}}$ domain shows a tendency to increase with increasing temperature. Most importantly, this mechanism leaves no way to explain why the $\mathbf{Q}_{\mathrm{N}}^{\mathrm{B}}$ domain reappears in a reversible way when the field is reduced.

Incidentally, the magnetostriction measurements by Doerr *et al.* show a strong asymmetry of their sample [48]. The volume ratio between the two domains is estimated to be 1:2, as explained by an unequal zero-field population of the two domains of the ordered system, and it is noticeable that even the asymmetry is

detected to reappear in a reversible way, after the application of a field of 6 T.

Alternatively, an explanation for the reversible behavior of the $\mathbf{Q}_{\mathrm{N}}^{\mathrm{B}}$ domain might be that the inhomogeneous type II phase of the superconductor, in some way, sustains this domain. An indicator of this is that the critical field for the stability of the $\mathbf{Q}_{\mathrm{N}}^{\mathrm{B}}$ domain, below 5 K, roughly coincides with H_{c2}. The value of $\kappa \approx 8$ is large in this system and the internal magnetic field is not varying much, as soon as the applied field is larger than a 0.2 T, so the inhomogeneities are mostly connected to the cores of the flux lines. How the cores may be able to stabilize the $\mathbf{Q}_{\mathrm{N}}^{\mathrm{B}}$ phase is an open question.

Middle panel, $H \parallel [110]$

For this field direction only three commensurable phases are presented in the grey-colored areas. The striped areas represent mixtures of two phases, defined by the color of each single phase region, e.g. $Q = 0.57$ light gray and $Q = 0.58$ dark gray and a mixture of these phases is observed in between the two phases and in the upper left corner. Again, starting at low fields and low temperature, the first two jumps of magnetization correspond to the changes of magnetic structure observed in neutron diffraction. Notice in this case the magnetization measurements are very smooth, but the jumps can be identified by looking at figure 26.

We cannot determine whether the second magnetization jump arises due to a change of magnetic structure from $Q = 0.57$ to $Q = 0.58$, or it is due to the change of double pair configuration $dduu \rightarrow duuu$, as discussed in the previous section. According to the model, the $dduu \rightarrow duuu$ transition would take place at this field [23]. Up to T = 3.5 K, the black circles overlap fairly well with the neutron diffraction data, but at higher temperatures the circles extend into the region where $Q = 0.55 - 0.56$ exists. It should be noted that at these high temperatures, the magnetization data must be even smoother than at 2 K, so the high temperature part of the phase line might be speculative.

A few points in the magnetization data indicate a vertical phase line at about 3.7 K, which we have no explanation for.

The white circles connected by a dotted line represent the transition to a rotated magnetic structure, with $\mathbf{Q}_{\mathrm{N}}^{\mathrm{A}} = (Q, \delta Q, 0)$ and $\mathbf{Q}_{\mathrm{N}}^{\mathrm{B}} = (\delta Q, Q, 0)$, $\delta Q \approx 0.005$. For T = 3.75 K and T = 4.75 K we have observed a rotation of $\mathbf{Q}$ at fields of 1.1 T and 1.0 T respectively, but we cannot say whether the structure rotates at a lower field. For all we know, it is possible that the rotation of $\mathbf{Q}$ follows the phase line determined by jumps in magnetization extending from $(T, B) = (2, 1.4)$ to $(T, B) = (5, 0.4)$, which was discussed above.

This rotation happens for all the observed commensurable structures with the exception of the seven layered $Q = \frac{4}{7}$ structure. The rotation may be explained by the gain in Zeeman energy of the commensurable structures, if the moments are rotated by an angle of the same sign and size as $\mathbf{Q}$ is rotated. This explanation is consistent with all observations: The rotation does not occur, if the field is applied along the c axis, or if the angle between the transverse components of the moments and the field is small, as it is in the $\mathbf{Q}_{\mathrm{N}}^{\mathrm{A}}$ domains, when the field is along [010] or is making an angle of 22.5° with [010] and [110]. In the $\mathbf{Q}_{\mathrm{N}}^{\mathrm{B}}$ domains, the rotation is observed in the latter case, where the angle is large and the domain is still stable at the required field.

A way to explain the rotation is to assume an additional anisotropic two-ion interaction making up for the inability of the classical coupling to rotate the

moments. That such a coupling is a possibility is demonstrated by the stability of the longitudinal polarization of the ordered moments in $TbNi_2B_2C$. The ordering wave vector in $TbNi_2B_2C$ is practically the same one as in $ErNi_2B_2C$, but the ordered moments are parallel to **Q** [43, 16]. The occurrence of this polarization in $TbNi_2B_2C$ reveals the presence of an anisotropic two-ion interaction similar to the classical one, but of opposite sign, so that it more than compensates for the strong reduction of the longitudinal coupling deriving from the classical interaction.

The rotation of **Q** may be considered as a 2π phase shift of the magnetic structure per approximately 200 double layers along the [010] direction. We have observed no higher harmonics perpendicular to [100] in the neutron diffraction experiments. Any higher harmonics would appear in the grid scans in figure 17 on page 40. This suggests that the phase shift proceeds in a smooth way. It is not obvious how the commensurable structures may accomplish that, but it is clear that long-period structures, like the 31 layered $Q = \frac{18}{31}$ structure, are less firmly locked to the lattice, and therefore may rotate more easily, than the 7 layered $Q = \frac{4}{7}$ structure. The mean-field model suggests another explanation for why the $Q = \frac{4}{7}$ structure does not rotate [23]. The calculations predict that this structure would behave in a unique way by staying in the *duudduu* configuration all the way up to the transition to the paramagnetic phase, without participating in the *dduu* $\rightarrow$ *duuu* transition at about 1.4 T. The rotation of Q probably occurs just above the *dduu* $\rightarrow$ *duuu* transition at low temperatures. This coincidence indicates that the extra Zeeman-energy gain deriving from the enhancement of the ferromagnetic component perpendicular to **Q** due to the *dduu* $\rightarrow$ *duuu* transition, is required in order to make the rotation of **Q** favorable. Therefore, the reason why the $Q = \frac{4}{7}$ structure does not rotate may be a consequence of the that gain in Zeeman-energy is insufficient, as long as the structure stays in the *dduu* phase.

Bottom panel, $H \parallel [001]$

The uniform magnetization created by a field along the c-axis is small, and smooth without any jumps, so only the neutron diffraction results are presented in the figure. The Nèel temperature (solid line) is determined by the mean field model [23], and the open squares are the Nèel temperature determined by extrapolating the tangent to the steepest part of the intensity curve to zero intensity. The lines are contour plots of the value of Q.

The critical field of the antiferromagnetic phase is calculated in the mean field model to be 18.3 T at 2 K [23], whereas the experimental value determined by Schmiedeshoff *et al.*[51] from resistivity measurements is 14 T. The results of T_N from our diffraction experiments, extending up to a field of 11 T, are in better agreement with the critical field predicted by the model. The difference between the two experimental sets of data may reflect a dependence of the critical field on the quality of the crystal, but also a minor misalignment of the field may produce a relatively large reduction of the critical field.

5.8 Summary

The present experimental analysis of the magnetic properties of $ErNi_2B_2C$, has revealed a remarkable variety of different commensurable magnetic structures.

The experiments on $ErNi_2B_2C$ was initiated in an attempt to solve the problem about the different behavior of H_{c2} at T_N for different field directions. The work

in this thesis established that the Fermi surface nesting structure is the stable magnetic structure at H_{c2} for all field directions.

The behavior of H_{c2} just below $T_{\rm N}$ is determined by two factors. One is the magnitude of the superzone energy gaps introduced by the antiferromagnetic ordering, which is proportional to the first harmonic of the ordered moments. The other is the rate of depletion in the density of Cooper-pair states produced by these gaps, as discussed in section 2.3. The first factor is of some importance for explaining the difference in the size of the cusps in H_{c2} at $T_{\rm N}$ observed experimentally [47]. The first harmonic increases rapidly, when the temperature is reduced below the second-order transition temperature at a constant field applied along [001]. When the field is applied in the *ab*-plane, the transition at $T_{\rm N}$ is of first order, with a first harmonic below the transition being relatively small, see sections 5.2 and 5.3. The first order transition may happen at slightly different temperatures in different domains of the sample, which may cause the transition to be smeared out. This different behavior may explain a reduction of the cusp, when the field is applied in the *ab*-plane instead of along [001]. At H_{c2}, the induced ferromagnetic moment shifts the conduction spin-up and spin-down bands with respect to each other, due to the RKKY interaction. These spin gaps are much the largest, when the field is in the *ab*-plane. As discussed above, the spin gaps probably have the consequence that the nesting peak in $\mathcal{J}_{\perp}(\mathbf{Q})$ is reduced, already above the magnetic ordering temperature. If the nesting feature is diminished, the result may be a further reduction of the cusps in H_{c2} at $T_{\rm N}$ in the *ab*-case.

In contrast, most of the magnetic properties of the present Er system are explained without any reference to the superconducting electrons. There might be some weak influences on the magnitudes of the moments, which are, however, difficult to detect as they probably disappear gradually when approaching the upper critical field.

The spectacular effect of the small-angle rotation of $\mathbf{Q}$ occurs at fields along [110]. This unexpected observation indicates that the classical dipole interaction cannot be the only anisotropic two-ion interaction of importance in this system. An additional one, like that responsible for the longitudinal polarization of the ordered moments in $TbNi_2B_2C$, is required in order to account for this particular phenomenon.

The second spectacular effect detected in the experiments is the surprising stability and the reversible behavior of the minority $\mathbf{Q}_{\rm N}^{\rm B}$ domain, when the field is applied along [010]. As discussed in the previous section, it is very unlikely that this phenomenon would have occurred in the normal phase of the magnet. The arguments only leave the explanation that the minority domain, for some unknown reason, is able to survive in parts of the crystal up to a field close to H_{c2}, due to the inhomogeneities introduced by the superconducting type II phase. This challenging problem needs to be examined in further detail.

6 $TmNi_2B_2C$

In $TmNi_2B_2C$ the moments order below $T_N = 1.5$ K in a unique structure with $\mathbf{Q}_F = (0.094, 0.094, 0)$ and the moments pointing in the c-direction, which is not seen in any of the other RNi_2B_2C [52, 53]. The origin of this magnetic phase was a puzzle, which we decided to resolve, and the result is presented below.

6.1 Experimental details

All samples were grown by a high-temperature flux method and isotopically enriched with 99.5 % ^{11}B to enhance the neutron transmission [54, 37].

The neutron diffraction experiments presented in this thesis on $TmNi_2B_2C$ were all performed for a field along [100]. They were carried out both at the BER-II reactor at BENSC, Hahn-Meitner Institut, and at the Risø National Laboratory DR3 research reactor.

The measurements at BENSC (magnetic ordering in $TmNi_2B_2C$) were performed on the cold neutron beam line V2 triple-axis spectrometer, using 13.75 meV neutrons, and pyrolythic graphite (004) monochromator and (002) analyzer crystals. The sample had a dimension of $2 \times 2 \times 1$ mm^3, and horizontal cryomagnets with maximum fields of respectively 4 T and 6 T were used. The collimation was open before the monochromator, 60′ before the sample, 60′ before the analyzer, and 60′ after the analyzer. Additionally, some high resolution measurements were performed using second order neutrons with an incident energy of 3.5 meV, a beryllium filter, and collimation open - 20′ - 20′ - open. The high resolution data with B = 2.6 T is included in section 6.3 of this thesis.

Using a high resolution set-up at the cold neutron TAS7 spectrometer at Risø the experiment concerning the low intensity tail of the $\mathbf{Q}_N$ phase in $TmNi_2B_2C$, was performed with 2.8 meV neutrons, pyrolythic graphite (002) monochromator and (002) analyzer crystals, and a collimation: open - 15′ - 15′ - 30′. The sample was the same as in the experiment described above which had a dimension of $2 \times 2 \times 1$ mm^3, and a 1.8 T horizontal cryomagnet was used.

The $(Tm_{1-x}Yb_x)Ni_2B_2C$ samples with $x = 0.10$ and 0.15 had a dimension of $4 \times 3 \times 0.2$ mm^3, and they where cooled down in a 1.8 T horizontal cryomagnet. The cold neutron TAS7 spectrometer was used with 15.2 meV neutrons, pyrolythic graphite (004) monochromator and (002) analyzer crystals, and an open collimation.

An experiment looking for a static or dynamic deformation at $\mathbf{Q} = (-0.48, 0, 4)$, was performed at SINQ at the Paul Scherrer Institute. Two large samples of $TmNi_2B_2C$ where glued onto one sample holder in order to obtain as much intensity as possible. The total weight of the samples was 360 mg, and the two samples were aligned within an angle of 0.5 ° in a 1.8 T horizontal cryomagnet. In the elastic part neutrons with 13.7 meV incoming energy were used, pyrolythic graphite (004) monochromator and (002) analyzer crystals, and a radial collimation of 120' between sample and analyzer. The inelastic part of the experiment was performed with 4.8 mev neutrons, pyrolythic graphite (002) monochromator and (002) analyzer crystals, and a beryllium filter with a radial collimation of 120' placed between sample and analyzer.

6.2 Results: Magnetic structures in $TmNi_2B_2C$

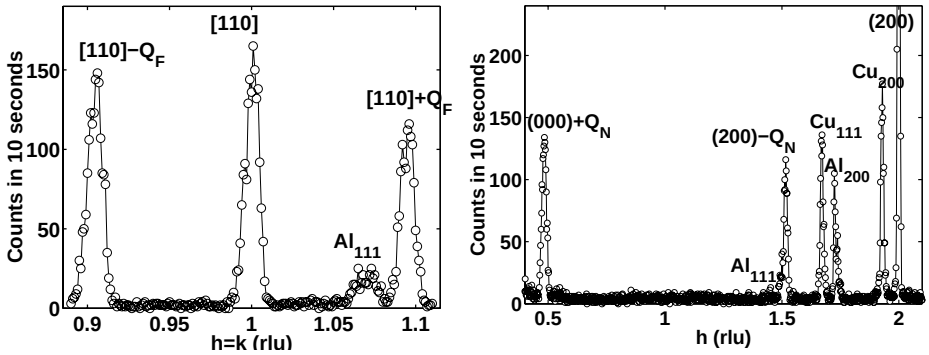

Figure 27. Left panel: $(hh0)$ scans through the (110) nuclear and the $(110) \pm \mathbf{Q}_F$ magnetic reflections at $B = 0$ T and $T = 0.1$ K. The reflection at $h = k = 1.07$ is an Al powder peak coming from the sample environment. Right panel: $(h00)$ scan for $B = 1.8$ T and $T = 0.1$ K showing magnetic reflections at $(000) + \mathbf{Q}_N$ and $(200) - \mathbf{Q}_N$, a nuclear reflection at (200), and some powder reflections from Al and Cu.

The zero field magnetic structure of $TmNi_2B_2C$ is a long wavelength structure with $\mathbf{Q}_F = (0.094, 0.094, 0)$. The left panel of Fig. 27 presents a scan in the [110] direction through the magnetic and nuclear reflections. The reflection at $h = k = 1.07$ is an aluminum powder peak which comes from the sample environment. Applying a magnetic field of more than 1 T in the a direction, gradually suppresses the $\mathbf{Q}_F$ magnetic phase, and another magnetic phase appears with $\mathbf{Q} = \mathbf{Q}_N$ =(0.482,0,0).

A long scan in the a direction is shown in the right panel of Fig. 27, and the $\mathbf{Q}_N$ reflection can be seen both at (000)+$\mathbf{Q}_N$ and at (200)-$\mathbf{Q}_N$. Additionally, powder reflections from Cu and Al are observed. The (200) nuclear reflection extends to 800 counts.

The behavior of the $\mathbf{Q}_N$ phase versus field and temperature is presented in Fig. 28, two values of the $\mathbf{Q}_N$ vector is observed, $\mathbf{Q}_{NI}$ and $\mathbf{Q}_{NII}$. The top panel shows the how the phase evolves in increasing fields. When the field is increased above 4 T a shoulder appears on the higher Q value side of the peak, and at 4.4 T the reflection has changed into a peak at $h = 0.495$ with a small shoulder at $h = 0.482$. The ordering vector $\mathbf{Q}_{NII} = (0.496, 0, 0)$, could at first sight look like a lock-in to the commensurate antiferromagnetic site

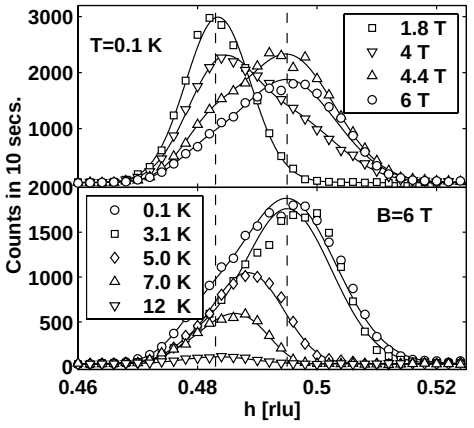

Figure 28. Longitudinal scans of the magnetic reflections observed in $TmNi_2B_2C$. The top and bottom panels are $[h00]$-scans through the $\mathbf{Q}_{NI}$/$\mathbf{Q}_{NII}$ reflections respectively at $T = 100$ mK as the field is increased from 1.8 to 6 T, and at $B = 6$ T for temperatures between 100 mK and 12 K. The position of the $\mathbf{Q}_{NI}$ and $\mathbf{Q}_{NII}$ peaks are indicated by the dashed lines.

$(0.5, 0, 0)$, but it was determined relative to the nuclear Bragg peaks within an accuracy of 0.001 rlu. The bottom panel of Fig. 28 presents scans through the $\mathbf{Q}_{\rm N}$ phase obtained at 6 T upon heating. At 100 mK the $\mathbf{Q}_{\rm NI}$ phase only shows up as a small shoulder on the $\mathbf{Q}_{\rm NII}$ peak. When the temperature is increased the intensity of both peaks decreases, but the relative intensity of $\mathbf{Q}_{\rm NI}$ with respect to $\mathbf{Q}_{\rm NII}$ increases and becomes the dominant at approximately 4 K. Note the transition does not proceed by a continuous translation of the ordering vector from $Q = 0.483$ to 0.496, since several of the peaks are asymmetric. Instead the intensity of one of the closely spaced reflections decreases as the intensity of the other increases.

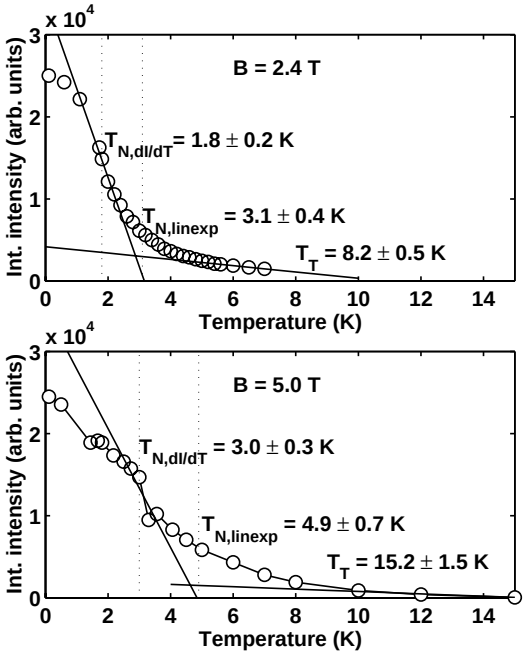

Figure 29. Temperature dependence of the numerically integrated intensity of the $\mathbf{Q}_{NI}$ and $\mathbf{Q}_{NII}$ reflections in $TmNi_2B_2C$. The data in the top panel is obtained in a field of 2.4 T ($\mathbf{Q}_{NI}$ only) and the bottom panel at 5 T. The lower limit of the Nèel temperature, $T_{(N,\frac{dI}{dT})}$, is determined as the maximum change of slope of the intensity curve. The upper limit of the Nèel temperature, $T_{(N,linexp)}$, and the vanishing temperature of the low intensity tail, T_T, is determined by the linear extrapolation to zero of respectively the steepest slope and the high temperature part of the intensity curve. Error bars for the numerically calculated intensity are smaller than the data points.

In figure 29 we show the temperature dependence of the numerically integrated intensity of the $\mathbf{Q}_{\rm NI}$ reflection at 2.4 T (top panel), and of the $\mathbf{Q}_{\rm NI}$ and $\mathbf{Q}_{\rm NII}$ reflections at 5 T (bottom panel). The total intensity is evaluated as the sum of scattered neutrons in a $[h00]$ scan through the reflection, subtracting the background scattering. Looking at the 2.4 T data, we see that the intensity is saturated at low temperatures, and starts to decrease linearly between 1 and 2 K. Above 2 K it bends of and a low intensity persists up to a temperature of 8 K. Due to this low intensity tail the Nèel temperature, $T_{\rm N}$, of the $\mathbf{Q}_{\rm N}$ phase is difficult to establish. Figure 29 presents the result of determining a lower and upper limit of $T_{\rm N}$. The lower limit is the maximum change of slope of the intensity curve ($T_{(\mathrm{N},\frac{dI}{dT})}$)

whereas the upper limit is determined by fitting a straight line to the steepest part of the intensity curve and extrapolating it to zero intensity ($T_{(\mathrm{N,linexp})}$). The vanishing temperature of the low intensity tail, T_{T}, is determined by extrapolating the last part of the curve to zero. Since it is notoriously difficult to determine the vanishing of such a slowly decreasing signal, it was not possible to determine this temperature to greater accuracy than a few degrees. The result for 2.4 T is: $T_{(\mathrm{N},\frac{dI}{dT})} = 1.8 \pm 0.2$ K, $T_{(\mathrm{N,linexp})} = 3.1 \pm 0.4$ K, and $T_{\mathrm{T}} = 8.2 \pm 0.5$ K. In the lower part of figure 29 the same analysis is performed for the 5 T data, yielding $T_{(\mathrm{N},\frac{dI}{dT})} = 3.0 \pm 0.3$ K, $T_{(\mathrm{N,linexp})} = 4.9 \pm 0.7$ K, and $T_{\mathrm{T}} = 15.2 \pm 1.5$ K. Notice that the intensity is not as smooth as in the 2.4 T case, a clear jump is observed at 3 K. This may be caused by extinction: at low temperature both the $\mathbf{Q}_{\mathrm{NI}}$ and $\mathbf{Q}_{\mathrm{NII}}$ phase exists, but at 3 K the $\mathbf{Q}_{\mathrm{NII}}$ phase is suppressed, and only one phase, the $\mathbf{Q}_{\mathrm{NI}}$ is observed. Thus the total intensity may appear smaller in the single phase than in the double phase. This is consistent with the observation that the lower limit of T_{N} (determined as the maximum of $-\frac{dI}{dT}$) coincides with the transition temperature for the disappearance of the $\mathbf{Q}_{\mathrm{NII}}$ ordering vector (diamonds in fig. 31), for all fields where the $\mathbf{Q}_{\mathrm{NII}}$ phase exists. At this point it is important to notice that the Nèel temperature defined a lower and upper limits is not the transition temperature for a true phase transition, which becomes apparent for the 5 T data where there is no clear change of slope in the intensity.

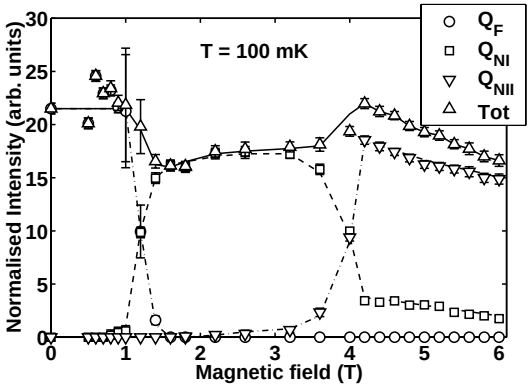

Figure 30. Field dependence of the integrated intensity of the $\mathbf{Q}_F$, $\mathbf{Q}_{NI}$, and $\mathbf{Q}_{NII}$ reflections in $TmNi_2B_2C$ at 100 mK following a zero field cooling and a field ramp at base temperature.

Figure 30 presents the field dependence of the integrated intensity of the different magnetic reflections at 100 mK. It is calculated as the product of the amplitude and width of the one- or two-Gaussian fits to the scans. For the two-Gaussian fits, the best fits were obtained by setting the width to a constant value, obtained in the one-Gaussian fits below 4 T. The intensity of the $\mathbf{Q}_{\mathrm{F}}$ reflection was obtained from Gaussian fits to $[hh0]$ scans ($h = 0.9 - 1.1$) through the two magnetic peaks around (110), and the $\mathbf{Q}_{\mathrm{NI}}$ and $\mathbf{Q}_{\mathrm{NII}}$ intensities were acquired from Gaussian fits to $[h00]$ scans through (000) + $\mathbf{Q}_{\mathrm{NI/NII}}$. Notice, in this way we compare intensities of longitudinal scans only. Also shown is the sum of the integrated intensity for all the magnetic reflections. All $\mathbf{Q}_{\mathrm{F}}$ intensities are scaled by the Lorentz-, form-, and structure factors, in order to obtain an intensity which is comparable to the intensity of the $\mathbf{Q}_{\mathrm{N}}$ reflection, see appendix A. The error bars for the determination of the form factor of the Tm ion in $TmNi_2B_2C$ are quite large. This results

in an error bar of 25 % on scaling the $\mathbf{Q}_{\mathrm{F}}$ intensity to $\mathbf{Q}_{\mathrm{NI}}$ values. This is valid for all the $\mathbf{Q}_{\mathrm{F}}$ values, but on the figure, it is indicated only for B = 1 T and B = 1.1 T. A jump in the total intensity appears at the $\mathbf{Q}_{\mathrm{F}} \rightarrow \mathbf{Q}_{\mathrm{NI}}$ transition at 1.4 T, however this is within the accuracy of the correction from $\mathbf{Q}_{\mathrm{F}}$ intensity to $\mathbf{Q}_{\mathrm{NI}}$ intensity. More interestingly, we observe an increase at the $\mathbf{Q}_{\mathrm{NI}} \rightarrow \mathbf{Q}_{\mathrm{NII}}$ transition at 4 T, which also appears when doing a numerical integration of the intensity. This could be due to a change of spin configuration connected to the change of ordering vector ($\mathbf{Q}_{\mathrm{NI}} \rightarrow \mathbf{Q}_{\mathrm{NII}}$). If the magnetic ordering is sinusoidal, the magnetic intensity depends only on the size of the ordered magnetic moment. If not, higher order reflections appear and the exact spin configuration of the magnetic wave determines the intensity of the first harmonic, therefore a change of spin configuration could lead to a change of intensity. Another possible explanation for the jump at 4 T is extinction. Below 4 T only one magnetic phase is present, and the intensity could be reduced due to extinction, whereas above 4 T two magnetic phases coexist, which could lower the effect of extinction and therefore increase the total amount of scattered intensity. Above 4 T the intensity of the $\mathbf{Q}_{\mathrm{NII}}$ (and $\mathbf{Q}_{\mathrm{NI}}$) reflection decreases, which indicates that the magnetic moments are beginning to tilt towards the field.

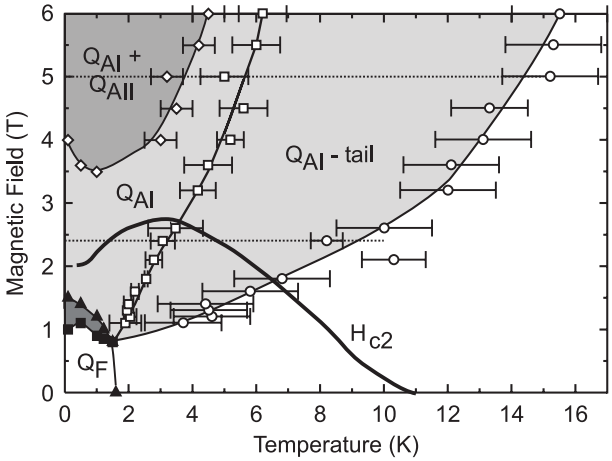

Figure 31. Experimental phase diagram for $TmNi_2B_2C$ with the magnetic field along [100] *showing the extent of the magnetic phases by the different degrees of shading. Notice, the $\mathbf{Q}_{NI}$ and $\mathbf{Q}_{NII}$ phases are labelled $\mathbf{Q}_{AI}$ and $\mathbf{Q}_{AII}$ in this figure. The region between the solid squares and triangles show the overlap of the $\mathbf{Q}_F$ and $\mathbf{Q}_{NI}$ phases (dark shading). The upper limit of the Nèel temperature and the range of the low temperature tail, both determined as indicated in figure 29, is shown by respectively open squares and circles. The vanishing of the $\mathbf{Q}_{NII}$ phase is shown by diamonds, and above 4 T the lower limit of T_N match the diamonds of the $\mathbf{Q}_{NII}$ phase. The superconducting upper critical field, H_{c2}, was determined from transport measurements by Naugle et al. [29]. The dotted lines correspond to the temperature scans shown in figure 29.*

The results for $TmNi_2B_2C$ are summarized in figure 31, where we show the extent of the various magnetic phases. At low fields the magnetic $\mathbf{Q}_{\mathrm{F}}$ phases (marked by triangles) persist up to 1.5 T, with a transition to the $\mathbf{Q}_{\mathrm{NI}}$ phase (limited by open and solid squares) commencing at 1 T. At $3.5 - 4$ T the $\mathbf{Q}_{\mathrm{NII}}$ phase, marked by diamonds, appears and suppresses the $\mathbf{Q}_{\mathrm{NI}}$ phase to some extent.

However, the two phases continue to coexist up to the highest measured field. The majority of the phase diagram is dominated by the $\mathbf{Q}_{\mathrm{NI}}$ phase, and it is striking how, within our field range, both T_{N} (whether we consider the lower or upper limit of T_{N}) and T_{T} continues to increase with T_{T} reaching ten times the value of the zero field T_{N}. The dotted lines correspond to the two temperature curves shown in figure 29. It is especially interesting to look at the curve at 2.4 T. At this field the system enters the superconducting state at 5 K, and at approximately 1 K a re-entrance to the normal state occurs. However, looking at figure 29 there are no sudden changes in the integrated intensity at these transitions. Similar results were found for fields of 2.1 and 2.6 T.

Figure 32 presents an overview of the positions of the magnetic reflections around the nuclear peak (110) in reciprocal space. The long wavelength structure with $\mathbf{Q} = \mathbf{Q}_{\mathrm{F}}$ with four symmetry related peaks is replaced by two peaks with $\mathbf{Q} = \mathbf{Q}_{\mathrm{N}}$, when the magnetic field applied along the a axis exceeds 1.5 T. Notice the symmetry break introduced by the $\mathbf{Q}_{\mathrm{N}}$ structure, there are no peaks in the b direction of the $\mathbf{Q}_{\mathrm{N}}$ phase.

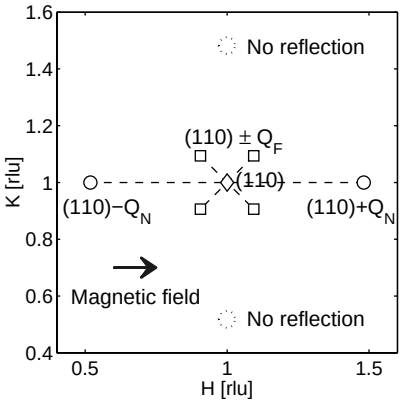

Figure 32. Reciprocal space (h, k) around the nuclear reflection (110)*, with the magnetic field direction indicated by an arrow.*

6.3 Results: Low intensity tail of the $\mathbf{Q}_{\mathrm{N}}$ phase in $TmNi_2B_2C$

In order to examine the details of the low intensity tail, we performed a high resolution study of the $\mathbf{Q}_{\mathrm{N}}$ phase in $TmNi_2B_2C$

The magnetic field was applied parallel to the a-axis, and the widths of both nuclear and magnetic peaks were measured along the a- and b-axes directions. The nuclear Bragg peaks were resolution limited, having widths consistent with the calculated resolution function obtained by the Rescal programme [55]. A comparison between the measured nuclear (200)-reflection and the calculated resolution is shown in the top panel of figure 33.

Longitudinal ([h00]) and transverse ([0k0]) scans through the $\mathbf{Q}_{\mathrm{NI}}$ reflection were performed at temperatures between 1.6 and 9 K, and fields of 1.2, 1.4. 1.5, 1.8, and 2.6 T. Overall, we found both widths to be constant within ± 10% for all temperatures and fields. Hence there appears to be no change of the magnetic correlation length between the main $\mathbf{Q}_{\mathrm{NI}}$ phase and the low intensity tail, or depending on whether this phase coexists with superconductivity or not.

Figure 34 presents the transverse width as a function of temperature at 1.8 T, and here one can see that in the high resolution scans the width is constant within the 10% mentioned above, whereas the low resolution scans present larger errorbars and larger deviations from the mean value, but no real features in the width which could explain e.g. a phase transition is observed.

The longitudinal width of the $\mathbf{Q}_{\mathrm{NI}}$ reflection was resolution limited, giving only a lower limit for the magnetic correlation length parallel to the field of $\xi_{\mathrm{m}}{}^{\parallel} = 400 \pm 50$ Å. For the transverse width it is possible to determine the magnetic correlation length perpendicular to the direction of the field, $\xi_{\mathrm{m}}^{\perp}$. The bottom panel

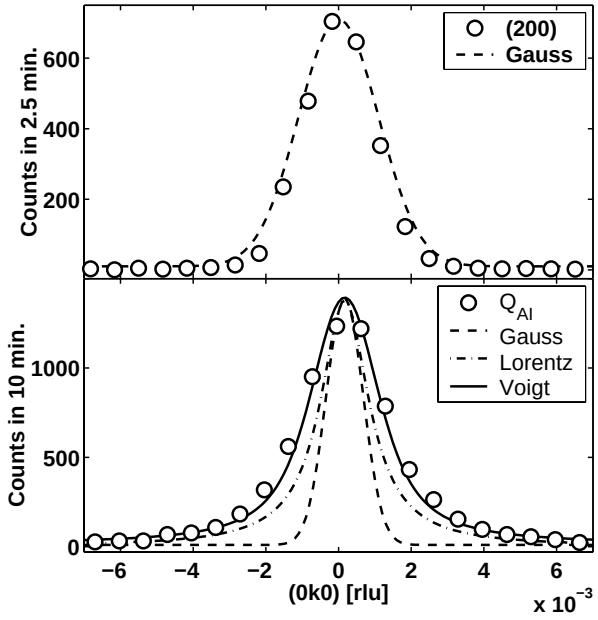

Figure 33. Top panel: High resolution transverse scan through the nuclear (200) *reflection, using second order neutrons. The dashed line is the calculated Gaussian resolution with a width of* 0.0026 *rlu. Bottom panel: High resolution transverse scan through* $(0.483, 0, 0)$ *at* 1.7 *K and* 1.8 *T. The full line is a Voigt fit to the data, composed of a Lorentzian (dash-dotted line) of width* 0.00160 *rlu, convoluted with a Gaussian (dashed line) with a width of* 0.0012 *FWHM rlu equal to the calculated resolution.*

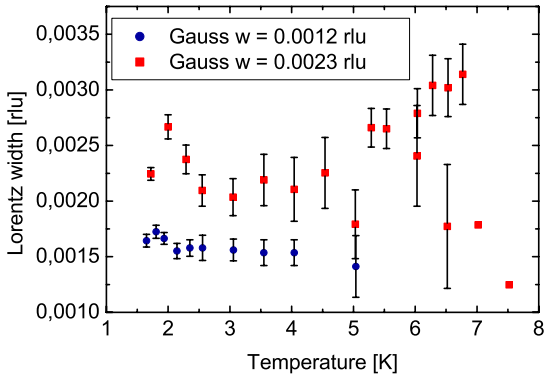

Figure 34. Widths of the magnetic reflection obtained from high (blue) and low (red) resolution transverse scan through $(0.483, 0, 0)$ *at* 1.8 *T. The widths are Lorentzian widths, obtained by fitting a Voigt function to the data, composed of a Lorentzian convoluted with a Gaussian with a fixed width of* 0.0012 *FWHM rlu (high resolution data, blue) or* 0.0023 *FWHM rlu (low resolution data, red).*

of figure 33 shows a transverse scan at $\mathbf{Q} = \mathbf{Q}_{\mathrm{NI}}$, with the calculated Gaussian resolution of 0.0012 rlu FWHM, indicated by the dashed line. It is clearly seen that there is a broadening of the reflection with pronounced tails as compared to the resolution. Fitting a Voigt function with the Gaussian width equal to the

calculated resolution, we obtain a width of the Lorentzian part shown by the dash-dotted line equal to $\Delta Q = (16 \pm 0.6) \cdot 10^{-4}$ rlu $= 29 \pm 1\ \mu\text{m}^{-1}$. Using the standard expression, $\xi = \frac{2}{\Delta Q}$, to determine the extent of the correlated volume, we obtain a magnetic correlation length of $\xi_{\text{m}}^{\perp} = 690 \pm 50$ Å. This is significantly longer than the superconducting coherence length, which is measured to be $\xi_{\text{sc}} = 120$ Å or 180 Å [54, 29].

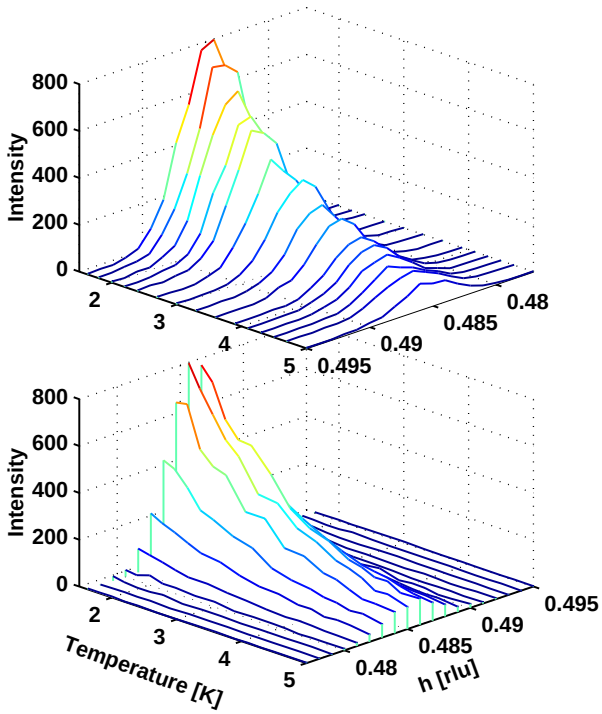

Figure 35. Top panel: High resolution longitudinal scans through the $(0.485, 0, 0)$ *reflection at* $B = 2.6$ *T, using second order neutrons. Bottom panel: A plot of the same scans versus temperature.*

Traditionally, one would consider the possibility that a tail of scattered neutrons could be due to diffuse scattering from small domains of magnetic ordering appearing as precursors of the bulk ordering. The signature of this would be an increased peak width just above T_{N} [56]. A way to visualize this is to plot the intensity versus temperature of a point in reciprocal space, which lies in the background, as close to the reflection as possible. Here a peak will appear at and above T_{N} in case of diffuse scattering. In the upper part of figure 35, longitudinal scans of the $\mathbf{Q}_{\text{N}}$ reflection at various temperatures is presented. In the lower part the same scans shows the temperature variation of the intensity at each reciprocal point in the h-scans, and it is clear that there is no sign of any peaks at the edges of the reflection. This is also the case for the transverse scans, so we conclude that the low intensity tail of the $\mathbf{Q}_{\text{N}}$ phase is not due to diffuse scattering.

6.4 Results: $(\text{Tm}_{1-x}\text{Yb}_x)\text{Ni}_2\text{B}_2\text{C}$

The motivation for examining the magnetic structures of Yb doped $TmNi_2B_2C$ was the idea of suppressing superconductivity by an alternative method. In this

way we could examine the interaction between superconductivity and the magnetic structures of $TmNi_2B_2C$.

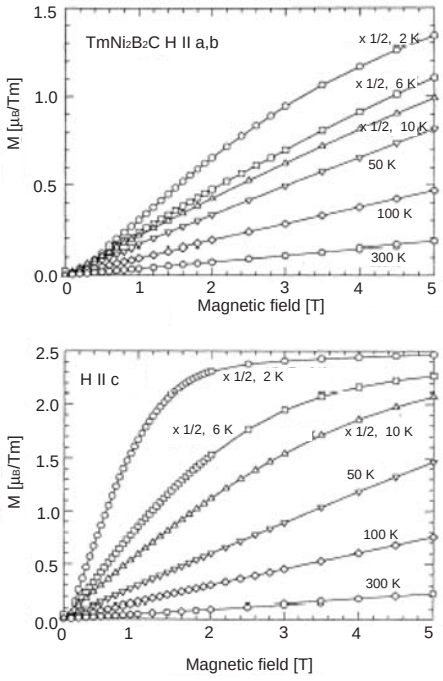

Figure 36. Magnetization measurements on pure $TmNi_2B_2C$ for magnetic fields applied perpendicular (upper panel) and parallel to the c-axis, from reference [54].

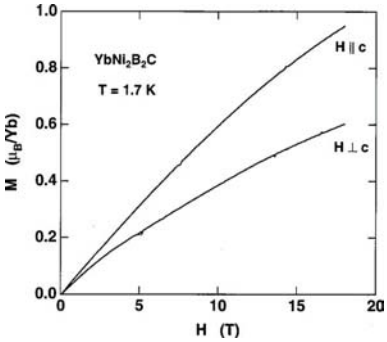

Figure 37. Magnetization measurements on $YbNi_2B_2C$ for magnetic fields applied perpendicular and parallel to the c-axis, from reference [57]

$YbNi_2B_2C$ is a heavy-fermion compound with a Kondo temperature of 10 K, and it shows no sign of superconducting or magnetic order down to 0.34 K [37]. There is a strong hybridization between the $4f$-levels and the conduction electrons in this material, which means that excited states are created in the superconducting energy gab, this decreases the energy gap, and thereby T_c is suppressed. As a consequence, ytterbium strongly suppresses superconductivity when using it as a dopant in superconducting RNi_2B_2C compounds. The magnetization curves of $TmNi_2B_2C$ and $YbNi_2B_2C$ are presented in figures 36 and 37. For $TmNi_2B_2C$ in the left panel, the T = 2 K data (circles) can be compared to the magnetization data for $YbNi_2B_2C$ in the right panel. Notice, both in $TmNi_2B_2C$ and $YbNi_2B_2C$ the c axis is the easy axis of magnetization, and the magnetization is much smaller in $YbNi_2B_2C$ than in $TmNi_2B_2C$. The magnetic properties of the two compounds are thus quite similar, but with Yb having a much smaller magnetic moment than the Tm ions.

In $TmNi_2B_2C$ superconductivity is partly suppressed by Yb doping, giving $T_c = 4.9$ K for $x = 0.1$, and $T_c = 2$ K for $x = 0.15$. In zero field the magnetic structure is the $\mathbf{Q}_F$ phase with similar wave vector and Nèel temperature as in the pure Tm compound. The assumption was that in $(Tm_{0.90}Yb_{0.10})Ni_2B_2C$ it would require a smaller field to go from the $\mathbf{Q}_F$ to the $\mathbf{Q}_{NI}$ phase than in the pure thulium

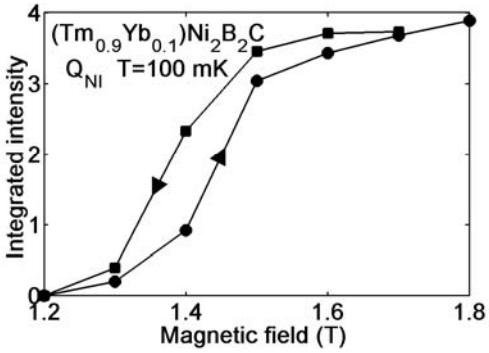

Figure 38. Integrated intensity of the $\mathbf{Q}_{NI}$ phase in $(Tm_{0.90}Yb_{0.10})Ni_2B_2C$, at 100 mK following a zero field cool, obtained in increasing fields (circles) and thereafter in decreasing fields (squares).

compound, because the effect of doping with ytterbium, should be analogous to applying a magnetic field.

In figure 38 the integrated intensity of the $\mathbf{Q}_{\rm NI}$ phase in $(\rm Tm_{0.90}Yb_{0.10})Ni_2B_2C$ is presented. The transition field is 1.4 T, which is 0.4 T higher than in the undoped thulium compound, and the field hysteresis is approximately 0.1 T. At 15 percent ytterbium doping the $\mathbf{Q}_{\rm F}$ phase is stable up to the maximum measured field of 1.8 T.

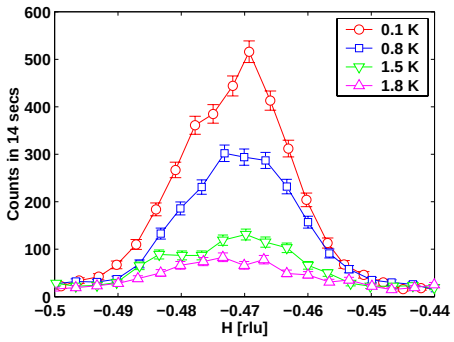

Figure 39. H-scans of the magnetic reflection at $(-0.47, 0, 0)$ in $(Tm_{0.90}Yb_{0.10})Ni_2B_2C$ in an applied field of 1.8 T, for temperatures of 0.1 K (circles), 0.8 K (squares), 1.5 K (down triangles), and 1.8 K (up triangles).

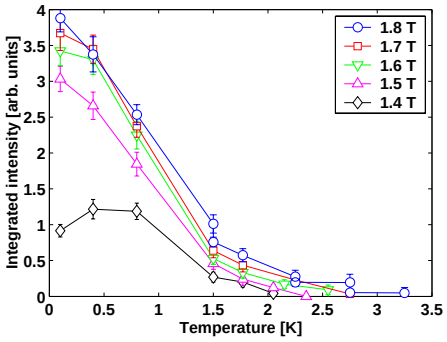

Figure 40. Integrated intensities of the $\mathbf{Q}_{NI}$ phase versus temperature in $(Tm_{0.90}Yb_{0.10})Ni_2B_2C$ in increasing fields, for fields of 1.4 T (diamonds), 1.5 T (up triangles), 1.6 T (down triangles), 1.7 T (squares), and 1.8 T (circles).

Fig. 39 presents h-scans of the magnetic reflection at 1.8 T for increasing temperatures. Notice that the center of the reflection lies at $h = 0.47 \pm 0.002$ rlu, whereas it lies at 0.482 for the pure thulium compound. The integrated intensity of the magnetic reflection is presented in Fig. 40. It is evaluated from Gaussian fits to h scans, similar to the ones shown in Fig. 39. The Nèel temperature which in the pure thulium compound was determined either by linear extrapolation of the steepest part of the intensity curve or by maximum in $-\frac{dI}{dT}$, cannot be determined because of missing data points in the range 0.8 to 1.5 K, where $T_{\rm N}$ lies. As in the

pure thulium compound a low intensity tail of the $\mathbf{Q}_{\mathrm{NI}}$ structure is observed. The tail temperatures lie in the range of 2 - 3 K, compared to Nèel temperatures lying between 1 K and 1.5 K. Here the maximum field examined is 1.8 T, and as expected the $\mathbf{Q}_{\mathrm{NII}}$ phase is not observed.

6.5 Results: Static or dynamic deformation

In a neutron diffraction experiment we cannot detect a possible quadrupolar ordering. However, since strain may play a role, we can look for either a static or a dynamic deformation of the crystal lattice. As explained in section 3.3 a softening of a phonon with wavevector $\mathbf{Q}_{\mathrm{N}}$ has been observed in YNi_2B_2C and $LuNi_2B_2C$. Imagine that this phonon is present also in $TmNi_2B_2C$ and that it may go soft and thereby support the quadrupolar structure. The deformation should correspond to c axis displacements of the Tm ions, with a period $\mathbf{Q}_{\mathrm{N}}$ along the a direction. Such a static deformation cannot be seen at the reciprocal point $(0.48, 0, 0)$, which is where the data presented in section 6.2 was taken. Instead one has to go to $(0.48, 0, l)$ points, because the larger l the stronger the reflection should be. We have performed an elastic neutron diffraction experiment looking at the reciprocal lattice point $(-0.48, 0, 4)$ both in zero field and in an applied field up to 1.8 T, and the results are presented in figure 41.

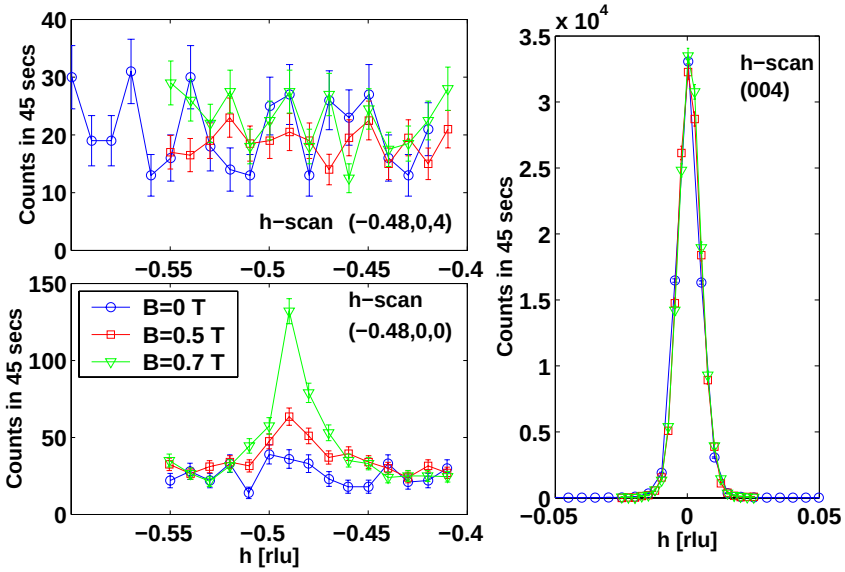

Figure 41. Development of reflections around $(-0.48, 0, 4)$ *(Top left) and* $(-0.48, 0, 0)$ *(bottom left), and a control scan at* (004)*, for applied fields of* 0 *T (circles),* 0.5 *T (squares), and* 0.7 *T (triangles).*

Notice in the upper left panel that there is no intensity at the $(-0.48, 0, 4)$ position, indicating that there is no static deformation. The intensity of the (004) reflection is 33500 neutron counts in 45 seconds, as seen in the right panel. In the same time interval, the background at (-0.48,0,4) lies in the interval of 15–30 neutron counts. Even though we do not see any intensity at this point, there could still be a static deformation, only with a smaller amplitude than what we can resolve in the present experiment.

A matlab calculation is performed in order to calculate the intensity of the

$(-0.48, 0, 4)$ reflection relative to the (004) reflection, in the case of a deformation of the thulium ions in the c direction with a wave vector of (-0.48,0,0). The conclusion is, assuming we are able to resolve a reflection with an intensity of half the background that a deformation of this kind would have an amplitude smaller than 2×10^{-3} lattice units.

The lower left panel presents scans of the $(-0.48, 0, 0)$ reflection in increasing fields, and notice that there is an indication of a peak already at 0.5 T, and a clear peak is visible at 0.7 T. In the experiments presented in section 6.2 the first sign of intensity appears at 0.8 T (see figure 30 on page 58). The reason that the magnetic intensity is not seen at the $(-0.48, 0, 4)$ reflection is due to several factors. Most significantly, in magnetic diffraction only the part of the magnetic moment perpendicular to the scattering vector can be seen yielding approximately a factor of $\frac{1}{9}$, but also the form factor of the magnetic scattering reduces the intensity by a factor $\frac{1}{4}$.

Figure 42 presents inelastic neutron scattering scans at the $(-0.48, 0, 4)$ reflection in order to look for a softening of the phonon at T_c, similar to what was seen in the other compounds. There is an indication of a slight softening, since the inelastic peak at 3 meV becomes more narrow moving slightly to the low energy side. In figure 43 the peak intensity of the scans in figure 42 is presented versus temperature. The intensity is measured at an energy transfer of 3.05 meV at $\mathbf{Q} = (-0.48, 0, 4)$. Instead of a clear interaction with superconductivity with a change of the phonon mode at T_c, in this case we observe that something happens at T $\approx$ 25 K and not at T_c. Further experiments are required in order to understand what happens to the phonon mode.

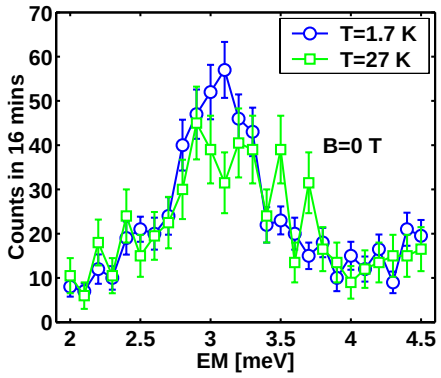

Figure 42. Inelastic scan at $\mathbf{Q} = (-0.48, 0, 4)$*, at* $T = 1.7$ *K (circles) and* $T = 27$ *K (squares), in zero field. The intensity at EM =* 3.05 *meV is used in the next figure.*

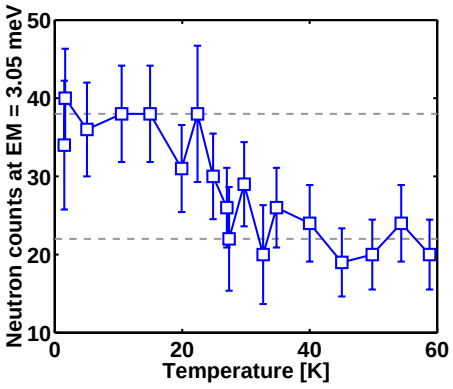

Figure 43. Neutron counts in 10 *minutes at an energy transfer EM = 3.05 meV, at the reciprocal lattice point* $\mathbf{Q} = (-0.48, 0, 4)$*. The grey lines are guides to the eye, indicating the low and high temperature levels of neutron counts.*

6.6 Summary and discussion

The assumption when starting the experiments on $TmNi_2B_2C$ was that applying a magnetic field along the a-direction would suppress superconductivity with little effect on the predominantly axial magnetic moments. In this way the appearance of the $\mathbf{Q}_N$ phase was believed to be caused by the suppression of superconductivity. This suppression made it energetically favorable to create a magnetic order with a Q-vector determined by the maximum in the magnetic susceptibility at the Fermi surface nesting vector $\mathbf{Q}_N$.

However, our results disprove the simple picture where a suppression of superconductivity induces a magnetic structure at $\mathbf{Q}_N$.

Two results imply that the controlling parameter is not superconductivity, but something else. Firstly, the intensity of the $\mathbf{Q}_N$ phase at 2.4 T does not show any sign of change when crossing H_{c2}. If superconductivity were the controlling parameter for the appearance of the $\mathbf{Q}_N$ phase, then we would expect a jump in the intensity at the superconducting transitions. Secondly, all when suppressing superconductivity by doping with Yb the transition field increases compared to the pure Tm compound. Doping with Yb on the Tm site suppresses superconductivity, but nonetheless the transition field between the $\mathbf{Q}_F$ and the $\mathbf{Q}_{NI}$ phases increases. If superconductivity were the controlling parameter for the appearance of the $\mathbf{Q}_{NI}$ phase, then we would expect the transition field to decrease in the doped compound. Generally, when doping with a magnetic ion in a superconductor, electron states appear in the superconducting gap. The energy scales of the Kondo system T_K relative to the superconducting system T_c, determines the position of the states in the gap, and the strongest effect on superconductivity appears for $T_c \approx T_K$ [58]. This delocalization of the $4f$-states by doping with Yb suppresses superconductivity significantly, however how the delocalization effects the magnetic structures is not obvious. Instead we can simply consider the $\mathbf{Q}_N$ magnetic structure as a standard rare earth case, where the de Gennes scaling controls the parameters of the magnetic phase. The de Gennes factor changes from $\frac{7}{6} = 1.167$ in a free thulium ion to $\frac{9}{28}$ in an ytterbium ion. This gives an average de Gennes factor of 1.08 in 10 % ytterbium doped $(Tm_{1-x}Yb_x)Ni_2B_2C$. T_N will decrease by 7 % corresponding to the average change in de Gennes factor. Even though the de Gennes analysis yields no information of whether it may explain the shift of 0.4 T in field, it does explain the destabilization of the $\mathbf{Q}_N$ phase.

Even though the role of superconductivity on the magnetic phases seems to be very weak, a purely magnetic stabilization of the $\mathbf{Q}_N$ phase is also not consistent with the present results. The Néel temperature ($T_N(B)$) of the $\mathbf{Q}_{NI}$ phase increases in increasing fields, up to the maximum field of 6 T. The usual scenario when applying a magnetic field perpendicular to the moments in an antiferromagnetically ordered state, is that the magnetic state is destabilized. If our starting assumption was correct, we would expect that at low fields, the $\mathbf{Q}_{NI}$ phase would be stabilized by a field because of the increasing suppression of superconductivity, giving an increasing $T_N(B)$ in field. Whereas, above H_{c2} one would expect the applied field to suppress the antiferromagnetic $\mathbf{Q}_{NI}$ phase gradually, and $T_N(B)$ would decrease in increasing fields. Instead we observe an increasing $T_N(B)$ in increasing fields throughout the field region. Thus we conclude that the $\mathbf{Q}_{NI}$ phase is stabilized by something else than a purely magnetic interaction, e.g. as in CeSb, where a strong uniaxial anisotropy and magnetoelastic effect give rise to a cascade of magnetic structures with an increasing T_N in field [59].

The results presented in this thesis suggest that the properties of the $\mathbf{Q}_N$ phase

cannot solely be attributed to the suppression of superconductivity. The applied magnetic field induces some other mechanism, which stabilizes the $\mathbf{Q}_{\mathrm{N}}$ phase. The smooth variation of the intensity of the $\mathbf{Q}_{\mathrm{N}}$ phase with temperature with no signature of a true phase transition, also indicates that we are dealing with a field induced phenomenon. Any theory attempting to explain the magnetic phases of $TmNi_2B_2C$ in a magnetic field, should address not only the points discussed above, but also three other properties of the $\mathbf{Q}_{\mathrm{NI}}$ phase.

Firstly, the appearance of $\mathbf{Q}_{\mathrm{NII}}$ ordering above 4 T is not yet understood. It might be that the origin of the $\mathbf{Q}_{\mathrm{NII}}$ phase lies in field induced modifications of the Fermi surface. Secondly, the $\mathbf{Q}_{\mathrm{N}}$ phase appears only parallel to the applied field, not perpendicular to it. This symmetry break introduced by the $\mathbf{Q}_{\mathrm{N}}$ phase is not yet understood. Thirdly, the low intensity tail of the $\mathbf{Q}_{\mathrm{N}}$ phase, which has a constant correlation length throughout the phase diagram, and extends as high as to 15 K, is not accounted for in any present theory.

All in all it appears obvious that a new mechanism, not controlled by superconductivity, is in play and needs to be unravelled before the unusual experimental phase diagram of $TmNi_2B_2C$ can be accounted for. As presented in section 2.4, a quadrupolar and/or magnetoelastic effect may explain the rising T_{N}, the low intensity tail, and the symmetry break of the $\mathbf{Q}_{\mathrm{N}}$ phase. Further experiments will reveal if this is the true explanation of the magnetic structures of $TmNi_2B_2C$.

7 Summary and outlook

The work in this thesis has been a search for evidence for a clear interaction between superconductivity and magnetism. However, most of the results indicate that the superconducting properties play a small, if any, role in the magnetic system.

7.1 Summary

The results presented in chapters 5 and 6 are summarized in the following.

$ErNi_2B_2C$

The present experimental analysis of the magnetic properties of $ErNi_2B_2C$, has revealed a remarkable variety of different commensurable magnetic structures. The experiments on $ErNi_2B_2C$ were initiated in an attempt to solve the problem with the different behavior of the upper critical field at T_N for different field directions. The work in this thesis established that the Fermi surface nesting structure is the stable magnetic structure at H_{c2} for all field directions.

I conclude that most of the magnetic properties of the present $ErNi_2B_2C$ system are explained without any reference to the superconducting electrons.

The spectacular effect of the small-angle rotation of $\mathbf{Q}$ occurs at fields along [110]. This unexpected observation indicates that the classical dipole interaction cannot be the only anisotropic two-ion interaction of importance in this system.

The second spectacular effect detected in the experiments is the surprising stability and the reversible behavior of the minority $\mathbf{Q}_N^B$ domain, when the field is applied along [010]. It is very unlikely that this phenomenon would have occurred in the normal phase of the magnet. The arguments only leave the explanation that the minority domain, for some unknown reason, is able to survive in parts of the crystal up to a field close to H_{c2}, due to the inhomogeneities introduced by the superconducting type II phase.

$TmNi_2B_2C$

Initially, the appearance of the $\mathbf{Q}_N$ phase was believed to be caused by the suppression of superconductivity. This suppression made it energetically favorable to create a magnetic order with a Q-vector determined by the maximum in the magnetic susceptibility at the Fermi surface nesting vector $\mathbf{Q}_N$. The results presented in this thesis suggest that the properties of the $\mathbf{Q}_N$ phase cannot solely be attributed to the suppression of superconductivity.

Two results imply that the controlling parameter is not superconductivity, but something else. Firstly, the intensity of the $\mathbf{Q}_N$ phase at 2.4 T does not show any sign of change when crossing H_{c2}. Secondly, all when suppressing superconductivity by doping with Yb the transition field increases compared to the pure Tm compound.

Even though the role of superconductivity on the magnetic phases seems to be very weak, a purely magnetic stabilization of the $\mathbf{Q}_N$ phase is also not consistent with the present results. Two results indicate that we are dealing with a field induced phenomenon: The Néel temperature ($T_N(B)$) of the $\mathbf{Q}_{NI}$ phase increases in increasing fields, up to the maximum field of 6 T, and the smooth variation

of the intensity of the $\mathbf{Q}_N$ phase with temperatures with no sign of a true phase transition.

All in all it appears obvious that a new mechanism, not controlled by superconductivity, is in play and needs to be unravelled before the unusual experimental phase diagram of $TmNi_2B_2C$ can be accounted for. As presented in section 2.4, a quadrupolar and/or magnetoelastic effect may explain the rising T_N, the low intensity tail, and the symmetry break of the $\mathbf{Q}_N$ phase.

7.2 Outlook

Despite extensive studies of the magnetic properties of $ErNi_2B_2C$ and $TmNi_2B_2C$ there are still interesting questions to be answered. Listed below are a number of experiments which are a direct extension of those reported in this thesis.

- $ErNi_2B_2C$: Further studies of the rotation of the $\mathbf{Q}$ vector in order to establish whether the rotation is connected to the $dduu \rightarrow duuu$ transition or if it is a signature of the transition from the normal to superconducting phase.
- $ErNi_2B_2C$: The interesting lack of hysteresis in the minority domain should be examined in detail. In order to determine if this phenomenon is connected to the superconducting flux cores, it should be studied while varying the superconducting properties. This can be done either by varying the temperature, by doping e.g. with cobalt on the nickel site, or by applying an additional magnetic field in the c-direction.
- $TmNi_2B_2C$: A static deformation of the Tm ions in the c direction with wavevector $\mathbf{Q}_N$ could explain all observed features of the magnetic phase in $TmNi_2B_2C$. An X-ray experiment can determine the structural details both in zero and non-zero magnetic field.
- $TmNi_2B_2C$: In case there is no static deformation to be observed by X-ray scattering, it could be interesting to try to look for a phonon softening at the nesting wavevector $\mathbf{Q}_N$ similar to what was observed in $LuNi_2B_2C$, $HoNi_2B_2C$, and YNi_2B_2C compounds.

Acknowledgements

Many people have contributed with help to work presented in this thesis. In particular, I wish to express my gratitude for being part of a lively and very inspiring group of physicists at Risø. While working on this thesis, I have always had a broad group of specialists to rely on for the different problems I encountered. For this I wish to thank all my colleagues at Risø. In particular I want to thank my supervisor Niels Hessel Andersen for helping not only with discussions and encouragement, but also for his helpfulness and understanding during my pregnancy and maternity leave. Asger Abrahamsen deserves thanks for always being ready to help no matter what it took to solve the problem. Bente Lebech has been very helpful, specifically during some of the experiments, and in general by helping me to learn from her experience. Thanks to Anette Jensen for the impressive amount of work that was done while I was away.

The theoretical support for this thesis has been provided by Jens Jensen and Per Hedegård from the University of Copenhagen. Their contributions have been of great value in the planning and evaluation of experiments.

Paul C. Canfield has grown all the crystals which I have worked on. His dedicated nature provides a rich source of ideas and discussions which I have enjoyed to a great extent.

Much of the work presented in this thesis was done at Berlin Neutron Scattering Center at Hahn-Meitner Institut. Peter Vorderwisch, Jens Klenke, and Karel Prokes are instrument responsibles on the spectrometers V2, E1, and E4, and they deserve thanks for making sure that the experiment time was optimally used. Michael Meissner, Peter Smeibidl and the sample environment group deserve thanks for making sure that the sample environment worked to perfection. Michael Meissner also deserves thanks for doing heat capacity measurements on $TmNi_2B_2C$. That work is not included in this thesis, but will be published elsewhere.

Some of the experiments were performed at Paul Scherrer Institut in Zurich. Thanks to Stine Nyborg Klausen, Joel Mesot, and Christof Niedermayer for offering their help during my experiments on Rita-II, and Markus Zolliker for preparing the sample environment.

Last, but not least thanks to my husband Michael deserves thanks for being there all the way. He accepted the temporary status of single parenthood with the extra pressure of having a confused and at times mentally absent wife. Our daughter, Victoria, has given us many moments of pure joy, making it easier for me to focus on the work that needed to be done.

References

[1] J. Jensen. Mean-field model of the ferromagnetic ordering in the superconducting phase of $ErNi_2B_2C$. *Physical Review B* **65**, 140514 (2002).

[2] J. Jensen. Private communication.

[3] M. B. Maple. Superconductivity, A probe of the magnetic state of Local Moments in metals. *Applied Physics* **9**, 173–203 (1976).

[4] A. A. Abrikosov & L. P. Gorkov. Contribution to the Theory of Superconducting Alloys with Paramagnetic Impurities. *Sov. Phys. JETP* **12**, 1243–1253 (1961).

[5] J. W. Lynn, J. A. Gotaas, R. W. Erwin, R. A. Ferrell, J. K. Bhattacharjee, R. N. Shelton & P. Klavins. Temperature dependent sinusoidal magnetic order in the superconductor $HoMo_6Se_8$. *Physical Review Letters* **52**, 133–136 (1984).

[6] R. Nagarajan, C. Mazumdar, Z. Hossain, S. K. Dhar, K. V. Gopalakrishnan, L. C. Gupta, C. Godart, B. D. Padalis & R. Vijayaraghavan. Bulk Superconductivity at an Elevated Temperature ($T_c \approx 12$ K) in a Nickel Containing Alloy System Y-Ni-B-C. *Physical Review Letters* **72**, 274–277 (1994).

[7] R. J. Cava, H. Takagi, H. W. Zandbergen, J. J. Krajewski, W. F. Peck Jr, T. Siegrist, B. Batlogg, R. B. van Dover, F. J. Felder, K. Mizuhashi, J. O. Lee, H. Eisaki & S. Uchida. Superconductivity in the quaternary intermetallic compounds $LnNi_2B_2C$. *Nature* **367**, 252–253 (1994).

[8] T. Siegrist, H. W. Zandbergen, R. J. Cava, J. J. Krajewski & W. F. Peck Jr. The crystal structure of superconducting $LuNi_2B_2C$ and the related phase LuNiBC. *Nature* **367**, 254–256 (1994).

[9] J. Jensen & A. R. Mackintosh. *Rare Earth Magnetism.* Oxford Science Publications, (1991).

[10] U. Gasser, P. Allenspach, F. Fauth, W. Henggeler, J. Mesot, A. Furrer, S. Rosenkrantz & P. Vorderwisch. Neutron crystal-field spectroscopy of RNi_2B_2C (R = Ho, Er, Tm). *Zeitschrift fur Physik B* **101**, 345–352 (1996).

[11] P. C. Canfield & S. L. Bud'ko. Angular dependence of metamagnetic transitions in RNi_2B_2C (R = Er, Ho, Dy, Tb). *J. Alloys Compd.* **262**, 169 (1997).

[12] T. V. Ramakrishnan & C. M. Varma. Pairbreaking in superconductors near and below antiferromagnetic transitions. *Physical Review B* **24**, 137 (1981).

[13] S. B. Dugdale, M. A. Alam, I. Wilkinson, R. J. Hughes, I. R. Fischer, P. C. Canfield, T. Jarlborg & G. Santi. Nesting properties and anisotropy of the Fermi surface of $LuNi_2B_2C$. *Physical Review Letters* **83**, 4824–4827 (1999).

[14] P. W. Anderson & H. Suhl. Spin Alignment in the Superconducting State. *Physical Review* **116**, 898–900 (1959).

[15] C. Detlefs, A. I. Goldman, C. Stassis, P. C. Canfield, B. K. Cho, J. P. Hill & D. Gibbs. Magnetic structure of $GdNi_2B_2C$ by resonant and nonresonant x-ray scattering. *Physical Review B* **53**, 6355 (1996).

[16] P. Dervenagas, J. Zarestky, C. Stassis, A. I. Goldman, P. C. Canfield & B. K. Cho. Magnetic structure of $TbNi_2B_2C$. *Physical Review B* **53**, 8506 (1996).

[17] K. D. D. Rathnayaka, D. G. Naugle, B. K. Cho & P. C. Canfield. Anisotropic magnetoresistance of single-crystal $HoNi_2B_2C$ and the interplay of magnetic and superconducting order. *Physical Review B* **53**, 5688–5695 (1996).

[18] A. I. Goldman, C. Stassis, P. C. Canfield, J. Zaretsky, P. Dervenagas, B. K. Cho & D. C. Johnston. Magnetic pair breaking in $HoNi_2B_2C$. *Physical Review B* **50**, 9668–9671 (1994).

[19] J. Zarestky, C. Stassis, A. I. Goldman, P. C. Canfield, P. Dervenagas, B. K. Cho & D. C. Johnston. Magnetic structure of $ErNi_2B_2C$. *Physical Review B* **51**, 678–680 (1995).

[20] K. Nørgaard, M.R. Eskildsen, N.H. Andersen, J. Jensen, P. Hedegård, S.N. Klausen & P.C. Canfield. Interdependence of Magnetism and Superconductivity in the Borocarbide $TmNi_2B_2C$. *Physical Review Letters* **84,21**, 4982–4985 (2000).

[21] C. Detlefs, F. Bourdarot, P. Burlet, P. Dervenagas, S. L. Budko & P. C. Canfield. Ordering wave vectors of metamagnetic states in $HoNi_2B_2C$: One dimension is not enough. *Physical Review B* **61**, R14916 (2000).

[22] A. Kreyssig. Private communication.

[23] A. Jensen, K. Nørgaard Toft, A. B. Abrahamsen, D. F. McMorrow, M. R. Eskildsen, N. H. Andersen, J. Jensen, P. Hedegård, J. Klenke, S. Danilkin, K. Prokes, V. Sikolenko, P. Smeibidl, S. L. Budko & P. C. Canfield. Field-induced magnetic phases in the normal and superconducting states of $ErNi_2B_2C$. To be published, present version attached to this thesis.

[24] C. Detlefs, A. H. M. Z Islam, T. Gu, A. I. Goldman, C. Stassis, P. C. Canfield, J. P. Hill & T. Vogt. Magnetoelastic tetragonal-to-orthorhombic distortion in $ErNi_2B_2C$. *Physical Review B* **56**, 7843–7846 (1997).

[25] S.-M. Choi, J. W. Lynn, D. Lopez, P. L. Gammel, P. C. Canfield & S. L. Bud'ko. Direct observation of Spontaneous Weak Ferromagnetism in the Superconductor $ErNi_2B_2C$. *Physical Review Letters* **87**, 107001–107004 (2001).

[26] J. R. Waldram. *Superconductivity of metals and cuprates.* Institute of Physics Publishing, (1996).

[27] K. D. D. Rathnayaka, A. K. Bhatnagar, A. Parasiris, D. G. Naugle, P. C. Canfield & B. K. Cho. Transport and superconducting properties of RNi_2B_2C (R=Y, Lu) single crystals. *Physical Review B* **55**, 8506–8519 (1997).

[28] G. M. Schmiedeshoff, J. A. Detwiler, W. P. Beyermann, A. H. Lacerda, P. C. Canfield & J. L. Smith. Critical fields and specific heat of $LuNi_2B_2C$. *Physical Review B* **63**, 134519 (2001).

[29] D. G. Naugle, K. D. D. Rathnayaka & K. Clark. Critical field and magnetoresistance of single crystal $TmNi_2B_2C$. *Int. J. Mod. Phys. B* **13**, 3715 (1999).

[30] B. K. Cho, P. C. Canfield, L. L. Miller, D. C. Johnston, W. P. Beyermann & A. Yatskar. Magnetism and Superconductivity in single-crystal $ErNi_2B_2C$. *Physical Review B* **52**, 3684–3695 (1995).

[31] C. V. Tomy, M. R. Lees, L. Afalfiz, G. Balakrishnan & D. McK. Paul. Superconductity and magnetism in $DyNi_2B_2C$ single crystals. *Physical Review B* **52**, 9186–9189 (1995).

[32] M. R. Eskildsen. *Small Angle Neutron Scattering Studies of the Flux Line Lattices in the Borocarbide Superconductors*. PhD thesis, University of Copenhagen, (1998).

[33] L. F. Mattheiss. Electronic properties of superconducting $LuNi_2B_2C$ and related boride carbide phases. *Physical Review B* **49**, 13279–13282 (1994).

[34] M. Divis, H. Michor, S. Khmelevski, P. Blaha, G. Hilscher & K. Schwarz. First principles study of electronic structure of Rare Earth Borocarbides. *NATO Proceeding series* , 83–88 (2000).

[35] G. Hilscher, H. Michor & M. Divis. Magnetism and Superconductivity in the Rare Earth Nickel Borocarbides. *NATO Proceeding series* , 187–196 (2000).

[36] V. N. Narozhnyi, G. Fuchs, J. Freudenberger, K. Nenkov & K.-H. Müller. Why $PrNi_2B_2C$ does not superconduct? *Physica B* **284**, 535–536 (2000).

[37] A. Yatskar, N. K. Budraa, W. P. Beyermann, P. C. Canfield & S. L. Budko. Heavy-electron behavior in single-crystal $YbNi_2B_2C$. *Physical Review B* **54**, R3772 (1996).

[38] P. Dervenagas, M. Bullock, J. Zarestky, P. Canfield, B. K. Cho, B. Harmon, A. I. Goldman & C. Stassis. Soft phonons in superconducting $LuNi_2B_2C$. *Physical Review B* **52**, R9839–R9842 (1995).

[39] H. Kawano, H. Yoshizawa, H. Takeya & K. Kadowaki. Anomalous Phonon Scattering Below T_c in YNi_2B_2C. *Physical Reveiw Letters* **77**, 4628–4631 (1996).

[40] M. Bullock, J. Zarestky, C. Stassis, A. Goldman, P. Canfield, Z. Honda, G. Shirane & S. M. Shapiro. Low-energy phonon excitations in superconducting RNi_2B_2C (RE = Lu, Y). *Physical Review B* **57**, 7916–7921 (1998).

[41] A. Kreyssig, C. Sierks, M. Loewenhaupt, J. Freudenberger, G. Fuchs, K.-H. Müller & C. Ritter. Magnetic ordering and superconducting properties of $Ho_x(Lu/Dy)_{1-x}Ni_2B_2C$. *Physica B* **241**, 826–828 (1998).

[42] P. C. Canfield, B. K. Cho & K. W. Dennis. Magnetic properties of single crystal $GdNi_2B_2C$. *Physica B* **215**, 337 (1995).

[43] J. W. Lynn, S. Skanthakumar, Q. Huang, S. K. Sinha, Z. Hossain, L. C. Gupta, R. Nagarajan & C. Godart. Magnetic order and crystal structure in the superconducting RNi_2B_2C materials. *Physical Review B* **55**, 6584–6598 (1997).

[44] J. Als-Nielsen. *Neutron and synchrotron radiation for condensed matter studies*, volume 1, chapter 1, 3–33. Springer-Verlag (1993).

[45] A. J. C. Wilson. *International Tables for Crystallography*. Kluwer Academic Publishers, (1992).

[46] P. C Canfield, S. L. Budko & B. K. Cho. Possible co-existence of superconductivity and weak ferromagnetism in $ErNi_2B_2C$. *Physica C* **262**, 249–254 (1996).

[47] S. L. Budko & P. C. Canfield. Rotational tuning of H_{c2} anomalies in $ErNi_2B_2C$: Angular-dependent superzone gap formation and its effect on the superconducting state. *Physical Review B* **61**, R14932–R14935 (2000).

[48] M. Doerr, M. Rotter, M. El Massalami, S. Sinning, H. Takeya & M. Loewenhaupt. Magnetoelastic effects in $ErNi_2B_2C$ single crystal: probing the H-T phase diagram. *J. Phys.: Condens. Matter* **14**, 5609 (2002).

[49] A. J. Campbell, D. McK. Paul & G. J. McIntyre. Neutron diffraction study of metamagnetic phases in $ErNi_2B_2C$. *Solid State Communications* **115**, 213–216 (2000).

[50] N. J. Bancroft, D. McK. Paul, G. McIntyre & C. D. Dewhurst. Magnetism and superconductivity in $ErNi_2B_2C$. *Pramana, J. Phys.* **58**, 907–911 (2002).

[51] G. M. Schmiedeshoff, S. Touton, W. P. Beyermann, A. H. Lacerda, S.L. Bud'ko & P. C. Canfield. Magnetotransport and the magnetic phase diagram of superconducting $ErNi_2B_2C$. *Int. J. Mod. Phys. B* **16**, 3212– (2002).

[52] R. Movshovich, M. F. Hundley, J. D. Thompson, P. C. Canfield, B. K. Cho & A. V. Chubukov. Specific heat of single-crystal YNi_2B_2C and $TmNi_2B_2C$ superconductors. *Physica C* **227**, 381–386 (1994).

[53] B. Sternlieb, C. Stassis, A. I. Goldman, P. C. Canfield & S. Shapiro. Single crystal neutron diffraction study of the magnetic structure of $TmNi_2B_2C$. *Journal of Applied Physics* **81**, 4937–4939 (1995).

[54] B. K. Cho, Ming Xu, P. C. Canfield, L. L. Miller & D. C. Johnston. Magnetic and superconducting properties of single-crystal $TmNi_2B_2C$. *Physical Review B* **52**, 3676–3683 (1995).

[55] D. A. Tennant & D. F. McMorrow. for further information see: http://xray.physics.ox.ac.uk/rescal/rescal.htm.

[56] J. Als-Nielsen & R. J. Birgeneau. Mean field-theory, Ginzburg criterion, and marginal dimensionality of phase-transitions. *American Journal of Physics* **45**, 554–560 (1977).

[57] A. Yatskar, C. H. Mielke, P. C. Canfield, A. H. Lacerda & W. P. Beyermann. Magnetotransport in the heavy-fermion system $YbNi_2B_2C$. *Physical Review B* **60**, 8012–8018 (1999).

[58] E. Müller-Hartmann & J. Zittartz. Kondo effect in superconductors. *Physical Review Letters* **26**, 428–432 (1971).

[59] G. Meier, P. Fischer, W. Halg, B. Lebech, B. D. Rainford & O. Vogt. Magnetic phase transitions of CeSb: II. Effects of applied magnetic fields. *J. Phys. C: Solid State Phys.* **11**, 1173–1185 (1978).

A Scaling $\mathbf{Q_F}$ intensities to $\mathbf{Q_N}$ equivalents in $TmNi_2B_2C$

This appendix explains the steps necessary to convert integrated intensities of the $\mathbf{Q}_\mathrm{F}$-reflections to their equivalent value if they had been situated at $\mathbf{Q}_\mathrm{N}$. First, the differential scattering cross section of a magnetic reflection is evaluated:

A.1 Calculating the magnetic scattering

Equation 35 in section 4.1, is the differential scattering cross section for nuclear scattering.

$$\frac{d\sigma}{d\Omega} = |\sum_n b e^{i\boldsymbol{\kappa}\cdot\mathbf{R}_n}|^2. \tag{A.1}$$

When dealing with magnetic scattering the magnetic scattering length b replaces the nuclear scattering length b_m, see section 4.2:

$$\mathbf{b}_\mathrm{m}(\kappa) = \frac{e^2\gamma}{2m_\mathrm{e}c^2} f(\boldsymbol{\kappa}) \frac{|\boldsymbol{\mu}|}{\mu_\mathrm{B}} (\hat{\mu} - \hat{\kappa}(\hat{\kappa}\cdot\hat{\mu})), \tag{A.2}$$

where $\hat{\kappa}$ and $\hat{\mu}$ are unit vectors in the direction of $\boldsymbol{\kappa}$ and $\boldsymbol{\mu}$, $\gamma = -1.91$ is the gyromagnetic factor for the neutron, e the proton charge, c the velocity of light, m_e the electron mass, $f(\boldsymbol{\kappa})$ is the magnetic form factor which is evaluated in appendix A.2, and μ_B the Bohr magneton. Note that when doing neutron scattering, we only see the part of the magnetic moment that is perpendicular to the scattering vector, hence the scattering length is zero if the scattering vector is parallel to the magnetic moment.

The magnetic order of $TmNi_2B_2C$ is a transverse incommensurate antiferromagnetic structure. The propagation of the spin density wave is in the ab-plane and the magnetic moments are along the c-direction and assumes a value of $3.78\mu_\mathrm{B}$ [43]. The magnetic ordering vector is $\mathbf{Q}_\mathrm{F} = 0.094(\mathbf{a}^* + \mathbf{b}^*)$ [43]. According to Lynn *et al.* the wave is almost "squared up" which means that instead of the size of the magnetic moment following a pure sinus, then the moment assumes almost its maximum value, in the direction determined by the modulation. This structure corresponds to a period of the magnetic modulation of 26 Å (or 5.3 spins in the (110)-direction). If we assume that this is the case the magnetic moment can be described by:

$$\boldsymbol{\mu} = \mu(0, 0, \mathrm{sign}(\sin(\mathbf{Q}_\mathrm{F}\cdot\mathbf{r}_\mathrm{Tm}))). \tag{A.3}$$

Equations (35), (41), (A.2), and (A.3) are combined to calculate the differential scattering cross section of the magnetic structure in $TmNi_2B_2C$. If we keep the scattering vector in the ab-plane ($\boldsymbol{\kappa} = h\mathbf{a}^* + k\mathbf{b}^*$), then in low fields, the magnetic moments is confined to the c axis and $\boldsymbol{\kappa}\cdot\boldsymbol{\mu} = 0$, yielding:

$$\begin{aligned}\left(\frac{d\sigma}{d\Omega}\right)_\mathrm{mag} &= |\frac{e^2\gamma}{2m_\mathrm{e}c^2} f(\boldsymbol{\kappa}) \frac{\mu}{\mu_B}|^2 \\ &\cdot |\sum_{n_1,n_2,n_3} \mathrm{sign}(\sin(\mathbf{Q}_\mathrm{F}\cdot\mathbf{r}_{\mathrm{Tm}1})) e^{i\boldsymbol{\kappa}\cdot\mathbf{r}_{\mathrm{Tm}_1}} \\ &+ \mathrm{sign}(\sin(\mathbf{Q}_\mathrm{F}\cdot\mathbf{r}_{\mathrm{Tm}_2})) e^{i\boldsymbol{\kappa}\cdot\mathbf{r}_{\mathrm{Tm}_2}}|^2. \end{aligned} \tag{A.4}$$

Now we make a coordinate transformation so that the sum in the ab-plane is directed along the magnetic order vector. Because it is important to maintain the correct number of scatterers of the crystal, the sums in the ab-plane are now with $\frac{N_1}{\sqrt{2}}$ and $\frac{N_2}{\sqrt{2}}$. Two of the sums become Sinc functions and only one sum has to be evaluated numerically:

$$\left(\frac{d\sigma}{d\Omega}\right)_{\text{mag}} = |\frac{e^2\gamma}{2m_{\text{e}}c^2}f(\boldsymbol{\kappa})\frac{\mu}{\mu_{\text{B}}}|^2 S_{N_3}(\pi l) S_{\frac{N_1}{\sqrt{2}}}(\pi(h-k))$$
$$\cdot\ |\sum_{n_2=0}^{\frac{N_2}{\sqrt{2}}-1}\Big(\text{sign}(\sin(2\pi d 2n_2)) + \text{sign}(\sin(2\pi d(2n_2+1)))e^{i\pi(h+k)}$$
$$+\ \Big(\text{sign}(\sin(2\pi d(2n_2+1))) + \text{sign}(\sin(2\pi d(2n_2+2)))e^{i\pi(h+k)}\Big)\, e^{2\pi i k}\Big)$$
$$\cdot\ e^{2\pi i(h+k)n_2}|^2 \tag{A.5}$$

Here d is the period of the magnetic scattering vector: $[d,d,0]$= [0.094,0.094,0]. The short notation $|\sum_{n_2}...|^2$ will be used for the fourfold sum in equation (A.5). The sum depends on the reciprocal vector $[h,k,l]$ but in reality it is zero everywhere but at the magnetic scattering vectors, which is the sum of allowed reciprocal lattice vectors plus $[\pm d,\pm d,0]$ or giving higher order peaks: plus 3, 5, or 7 $\cdot$ $[\pm d,\pm d,0]$. For every reciprocal lattice vector $\boldsymbol{\kappa} = h\mathbf{a}^* + k\mathbf{b}^*$, the sum is evaluated and this gives us the magnetic differential scattering cross section of $TmNi_2B_2C$.

In summary, the magnetic differential scattering cross section consists of two terms which differ for the two magnetic structures $\mathbf{Q}_{\text{F}}$ and $\mathbf{Q}_{\text{N}}$, the form factor and the structure factor. Another factor plays a role in the real life of neutron diffraction, namely, the Lorentz factor. The optimal way to study a magnetic structure is to scan along lines in reciprocal space. The difference from an angular crystallographic method is that instead of letting the change in instrument settings correspond to equidistant steps in angle between data points, the change in instrument settings corresponds to equidistant steps in reciprocal lattice units. The change is of geometrical nature, and the correction factor is:
$L^{-1} = \sin(\theta + \alpha_Q)$, where $\theta = \arcsin\left(\frac{|\mathbf{Q}|}{2k}\right)$ and α_Q is the angle between the scattering vector and the scan direction.

All in all the scattered intensity of the $\mathbf{Q}_{\text{F}}$ structure is given by the following equation:

$$I_{scat} = K\left(\frac{e^2\gamma}{2m_{\text{e}}c^2}\right)^2\left(\frac{\mu}{\mu_{\text{B}}}\right)^2 |\ f(\boldsymbol{\kappa})\ |^2\ L(\boldsymbol{\kappa})\ \frac{N_1}{\sqrt{2}}N_3\ |\ \sum ...\ |^2\ . \tag{A.6}$$

where K is a spectrometer specific constant, $L(\boldsymbol{\kappa})$ is the Lorentz factor, N_1 and N_3 are the number of unit cells in the a and c direction, and the sum represents the structure factor. A similar sum can be evaluated for the $\mathbf{Q}_{\text{N}}$ structure. The form factor, the Lorentz factor and the structure factor varies between different magnetic reflections, and in the following these correction factors are presented. In each case the result is a factor to be multiplied to the $\mathbf{Q}_{\text{F}}$-intensity.

A.2 Evaluating the correction terms

The following constants are used in the calculations: The length of the reciprocal lattice vector: $a^* = \frac{2\pi}{3.486} = 1.79$ Å^{-1}. And the length of the k vector representing the energy of the neutrons in the experiments: $k = 2.58$ Å^{-1}.

Scattering vectors:

$$
\begin{aligned}
|\mathbf{Q}_{\mathrm{N}}| &= |0.483 \times (1,0,0)| = 0.483\ a^* = 0.865\ \text{Å}^{-1}, \\
|\mathbf{Q}_{\mathrm{F1}}| &= |(1-0.095) \times (1,1,0)| = \sqrt{2} \times 0.905\ a^* = 2.29\ \text{Å}^{-1}, \\
|\mathbf{Q}_{\mathrm{F2}}| &= |(1+0.095) \times (1,1,0)| = \sqrt{2} \times 1.095\ a^* = 2.77\ \text{Å}^{-1}, \\
|\mathbf{Q}_{\mathrm{F3}}| &= |(1+0.095, 1-0.095, 0)| = \sqrt{(1.095^2 + 0.905^2)}\ a^* = 2.54\ \text{Å}^{-1}. \\
|\mathbf{Q}_{\mathrm{F4}}| &= |(1-0.095, 1+0.095, 0)| = \sqrt{(1.095^2 + 0.905^2)}\ a^* = 2.54\ \text{Å}^{-1}.
\end{aligned}
$$

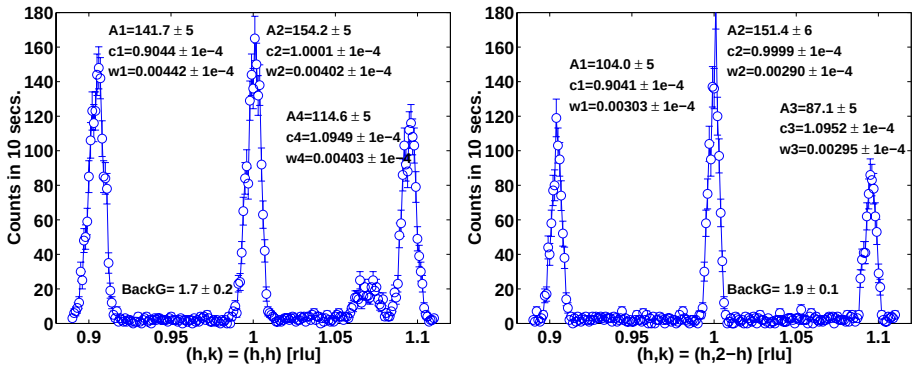

Figure 44. Left: Scan between the reciprocal lattice points $(0.89, 0.89)$ *and* $(1.11, 1.11)$ *through* $\mathbf{Q}_{F1}$ *(peak nr. 1),* (110)*,* Al_{111}*, and* $\mathbf{Q}_{F2}$ *(peak nr. 4). Right: Scan between the reciprocal lattice points* $(1.11, 0.89)$ *and* $(0.89, 1.11)$ *through* $\mathbf{Q}_{F3}$ *(peak nr. 1),* (110)*, and* $\mathbf{Q}_{F4}$ *(peak nr. 3). The results of Gaussian fits to the peaks are printed next to each peak.*

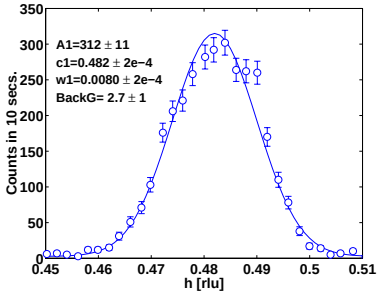

Figure 45. Longitudinal scan through the $\mathbf{Q}_N$ *peak. The results of a Gaussian fit is printed in the window.* $I = 312 \cdot 0.008 = 2.50$*.*

The integrated intensity of each magnetic reflection is obtained from figures 44 and 45 by multiplying the amplitude and width from the Gaussian scans. The factor $\sqrt{2}$ is due to the different step width when performing scans with steps of 0.001 rlu in the h direction and in the $h + k$ direction.

$$I(\mathbf{Q}_{\mathrm{N}}) = 2.50\ a^* = 4.475, \tag{A.7}$$

$$I(\mathbf{Q}_{\mathrm{F1}}) = \sqrt{2} \times 0.6271\ a^* = 1.588, \tag{A.8}$$

$$I(\mathbf{Q}_{\mathrm{F2}}) = \sqrt{2} \times 0.4616\ a^* = 1.169, \tag{A.9}$$

$$I(\mathbf{Q}_{\mathrm{F3}}) = \sqrt{2} \times 0.3147\ a^* = 0.7966, \tag{A.10}$$

$$I(\mathbf{Q}_{\mathrm{F4}}) = \sqrt{2} \times 0.2574\ a^* = 0.6516. \tag{A.11}$$

Lorenz factor

The Lorentz factor is given by:

$$L^{-1} = \sin\left(\theta + \alpha_Q\right),$$

where $\theta = \arcsin\left(\frac{|\mathbf{Q}|}{2k}\right)$ and α_Q is the angle between scattering vector and scan direction. For $\mathbf{Q}_{\mathrm{N}}$, $\mathbf{Q}_{\mathrm{F1}}$, and $\mathbf{Q}_{\mathrm{F2}}$, α_Q is zero and $L = \frac{1}{\sin\theta} = \frac{2k}{|\mathbf{Q}|}$:

$$L(\mathbf{Q}_{\mathrm{N}}) = \frac{2 \times 2.58}{0.865} = 5.965, \tag{A.12}$$

$$L(\mathbf{Q}_{\mathrm{F1}}) = \frac{2 \times 2.58}{2.29} = 2.253, \tag{A.13}$$

$$L(\mathbf{Q}_{\mathrm{F2}}) = \frac{2 \times 2.58}{2.77} = 1.863, \tag{A.14}$$

For $\mathbf{Q}_{\mathrm{F3}}$ and $\mathbf{Q}_{\mathrm{F4}}$ the scan starts in $(1.11, 0.89, 0)$ and ends in $(0.89, 1.11, 0)$, giving a scan direction of (-1,1,0). The scattering vectors are $(1.095, 0.905, 0)$ for $\mathbf{Q}_{\mathrm{F3}}$ and $(0.905, 1.095, 0)$ for $\mathbf{Q}_{\mathrm{F4}}$. α_Q is calculated as the angle between the scattering vector and the scan direction, using $\mathbf{a} \cdot \mathbf{b} = ab\cos\theta$:

$$\theta(\mathbf{Q}_{\mathrm{F3}}, \mathbf{Q}_{\mathrm{F4}}) = \arcsin\left(\frac{2.54}{2 \times 2.58}\right) = 29.49^{\mathrm{o}} \tag{A.15}$$

$$\alpha_Q(\mathbf{Q}_{\mathrm{F3}}) = \arccos\left(\frac{-1.095 + 0.905}{\sqrt{2} \times \sqrt{1.095^2 + 0.905^2}}\right) = 95.43^{\mathrm{o}} \tag{A.16}$$

$$L(\mathbf{Q}_{\mathrm{F3}}) = \frac{1}{\sin(29.49 + 95.43)} = 1.220, \tag{A.17}$$

$$\alpha_Q(\mathbf{Q}_{\mathrm{F4}}) = \arccos\left(\frac{-0.905 + 1.095}{\sqrt{2} \times \sqrt{1.095^2 + 0.905^2}}\right) = 84.57^{\mathrm{o}} \tag{A.18}$$

$$L(\mathbf{Q}_{\mathrm{F4}}) = \frac{1}{\sin(29.49 + 84.57)} = 1.095. \tag{A.19}$$

The Lorentz correction factors $f_{\text{Lorenz}}(\mathbf{Q})$ for different $\mathbf{Q}$ are given by:

$$f_{\text{Lorenz}}(\mathbf{Q}) = \frac{L_{\mathbf{Q}_\text{N}}}{L_{\mathbf{Q}}}, \tag{A.20}$$

$$f_{\text{Lorenz}}(\mathbf{Q}_{\text{F1}}) = \frac{5.965}{2.253} = 2.648, \tag{A.21}$$

$$f_{\text{Lorenz}}(\mathbf{Q}_{\text{F2}}) = \frac{5.965}{1.863} = 3.202, \tag{A.22}$$

$$f_{\text{Lorenz}}(\mathbf{Q}_{\text{F3}}) = \frac{5.965}{1.220} = 4.889, \tag{A.23}$$

$$f_{\text{Lorenz}}(\mathbf{Q}_{\text{F4}}) = \frac{5.965}{1.095} = 5.448. \tag{A.24}$$

Structure factor

The structure factor is presented in equation A.5, and the sum is evaluated in a matlab programme, calculating the intensity abs(jsum)^2 $N_1{}^2$ $N_3{}^2$ of the magnetic reflections at $\mathbf{Q}_\text{F}$ and $\mathbf{Q}_\text{N}$. Parameters used are N_1=N_2=30 and N_3=5.

$$f^2_{\text{Str. factor}} = \frac{f_{\text{Str. factor}}(\mathbf{Q}_\text{F})^2}{f_{\text{Str. factor}}(\mathbf{Q}_\text{N})^2} = \frac{3.849 \times 10^7}{2.193 \times 10^7} = 0.5697$$

Form factor

The magnetic form factor $f(\boldsymbol{\kappa})$ is determined by the distribution of magnetization within a single atom. In the majority of cases the magnetization is due to a single open atomic shell, therefore the form factor is the Fourier transform of the space distribution of the unpaired electrons. This is similar to the nuclear structure factor where it was a sum over the unit cell, but in this case the sum is over the magnetic moments of the unpaired electrons in the electron cloud. Within the dipole approximation (spherical symmetry) the magnetic form factor for a free Tm ion is given by:

$$f(\kappa) = \langle j_0(\kappa)\rangle + (1 - \frac{2}{g_\text{J}})\langle j_2(\kappa)\rangle \tag{A.25}$$

where g_J is the Landé splitting factor, and $\langle j_l(\kappa)\rangle$ are the l'th order spherical Bessel functions, corrected for the radial wavefunction for the unpaired electrons in the Tm atom. International Tables for Crystallography [45] give the coefficients in an analytical approximation to the Bessel functions:

$$\begin{aligned}\langle j_0(s)\rangle &= 0.0983 \cdot \mathrm{e}^{-18.324s^2} + 0.338 \cdot \mathrm{e}^{-6.918s^2} \\ &+ 0.5875 \cdot \mathrm{e}^{-2.662s^2} - 0.0241 \end{aligned} \tag{A.26}$$

$$\begin{aligned}\langle j_2(s)\rangle &= 0.176 \cdot s^2 \cdot \mathrm{e}^{-18.542s^2} + 0.9105 \cdot s^2 \cdot \mathrm{e}^{-6.579s^2} \\ &+ 0.897 \cdot s^2 \cdot \mathrm{e}^{-2.062s^2} - 0.0294 \cdot s^2 \end{aligned} \tag{A.27}$$

where $s = \frac{Q}{4\pi}$ in units of Å^{-1}. Notice that the strength of the magnetic reflections decreases quickly, as the length of the scattering vector increases.

Of course the distribution of electrons surrounding the atom in the crystal is not the same as in the free ion, and in the following, I compare results of calculating the form factor for the free Tm ion, and the empirically determined form factor,

which is obtained by fitting a Gaussian to the intensity of the magnetic structures versus the length of the scattering vector Q. Here it is important to use Lorenz- and structure- factor corrected intensities. Hence, the following intensity values are used:

$$I'(\mathbf{Q}) = \frac{I(\mathbf{Q}) \times f_{\text{Str. factor}}}{L(\mathbf{Q})} \tag{A.28}$$

$$I'(\mathbf{Q}_{\text{N}}) = \frac{4.408 \times 1}{5.965} = 0.738, \tag{A.29}$$

$$I'(\mathbf{Q}_{\text{F1}}) = \frac{1.588 \times 0.570}{2.253} = 0.402, \tag{A.30}$$

$$I'(\mathbf{Q}_{\text{F2}}) = \frac{1.169 \times 0.570}{1.863} = 0.358, \tag{A.31}$$

$$I'(\mathbf{Q}_{\text{F3}}) = \frac{0.797 \times 0.570}{1.220} = 0.372, \tag{A.32}$$

$$I'(\mathbf{Q}_{\text{F4}}) = \frac{0.652 \times 0.570}{1.095} = 0.339. \tag{A.33}$$

The two $\mathbf{Q}_{\text{F3}}$ and $\mathbf{Q}_{\text{F4}}$ intensities should be equal when corrected for the Lorentz factor, I cannot say why they are not. As a compromise, the average (0.355) is used in the calculations.

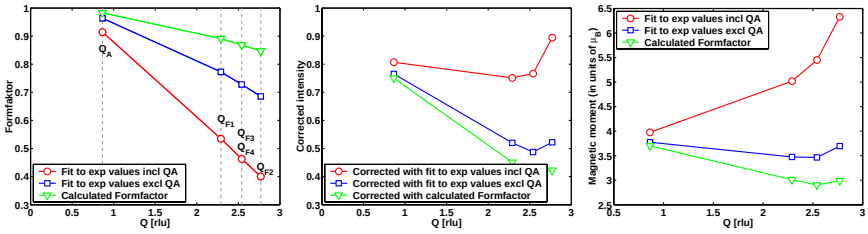

Figure 46. Left: Fitted and calculated form factors. Center: The form factor corrected experimental intensities. Right: The calculated magnetic moment.

Fitting the intensities of the $\mathbf{Q}_{\text{N}}$ and $\mathbf{Q}_{\text{F}}$ reflections with a Gaussian yields the result presented in figure 46. Circles include all five reflections, squares only the $\mathbf{Q}_{\text{F}}$ reflections, and triangles are the calculated form factors. In order to judge which form-factor correction is correct, I estimate the size of the magnetic moment calculated in the following way:

$$\left(\frac{d\sigma}{d\Omega}\right)_{\text{Mag}} = \left(\frac{e^2\gamma}{2m_{\text{e}}c^2}\right)^2 \left(\frac{\mu}{\mu_{\text{B}}}\right)^2 \mid f(\boldsymbol{\kappa}) \mid^2 \frac{N_1}{\sqrt{2}} N_3 \mid \sum \ldots \mid^2 . \tag{A.34}$$

$$\left(\frac{d\sigma}{d\Omega}\right)_{\text{Mag}} = \left(\frac{d\sigma}{d\Omega}\right)_{\text{Nuc}} \frac{I_{\text{Mag}}}{I_{\text{Nuc}}} = \mid F(\boldsymbol{\kappa}) \mid^2 N_1 N_2 N_3 \frac{I_{\text{Mag}}}{I_{\text{Nuc}}} \tag{A.35}$$

$$\left(\frac{\mu}{\mu_B}\right)^2 = \frac{N_2^2 \mid F(\boldsymbol{\kappa}) \mid^2}{\left(\frac{e^2\gamma}{2m_{\text{e}}c^2}\right)^2 \mid \sum \ldots \mid^2 \mid f(\boldsymbol{\kappa}) \mid^2} \frac{I_{\text{Mag}}}{I_{\text{Nuc}}} \tag{A.36}$$

The intensity of the (110) nuclear reflection is $154.2 \cdot 0.0040204 \cdot \sqrt{2}\, a^* = 1.578$ taken from figure 44. The intensities used for calculating the magnetic moment are corrected for Lorentz factors. The Lorentz factor for the (110) reflection is $\frac{2\,k}{Q} = \frac{2\,2.58}{\sqrt{2}\,1.79} = 2.02$

The value of the magnetic moment is calculated and plotted in the right part of figure 46. In the literature the magnetic moment of thulium in $TmNi_2B_2C$ is estimated to around 3.8 μ_B. It is clear that the circles, representing the fitted values, including the $\mathbf{Q}_N$ intensity is wrong, since the magnetic moment should be the same for all values of Q. The calculated form factor corrections of the free Tm ion (triangles), appears to underestimate the form factor. The empiric form factor (not including the $\mathbf{Q}_N$ intensity) (squares), appears to be the best estimate of the form factor, but note that the error in estimating the form factor is approximately 25 %:

$$F(\mathbf{Q}_N) = 0.964, \tag{A.37}$$
$$F(\mathbf{Q}_{F1}) = 0.773, \tag{A.38}$$
$$F(\mathbf{Q}_{F2}) = 0.686, \tag{A.39}$$
$$F(\mathbf{Q}_{F3}, \mathbf{Q}_{F4}) = 0.728. \tag{A.40}$$

The form factor corrections are:

$$f_{\text{Form factor}}(\mathbf{Q}_{F1}) = \frac{0.964}{0.773} = 1.247, \tag{A.41}$$
$$f_{\text{Form factor}}(\mathbf{Q}_{F2}) = \frac{0.964}{0.686} = 1.405, \tag{A.42}$$
$$f_{\text{Form factor}}(\mathbf{Q}_{F3}, \mathbf{Q}_{F4}) = \frac{0.964}{0.728} = 1.324. \tag{A.43}$$

A.3 Corrections

We can now multiply all the elements to get the complete correction factors as follows:

$$f(\mathbf{Q}) = f_{\text{Lorenz}} \times f_{\text{Str. factor}} \times f_{\text{Form factor}}, \tag{A.44}$$
$$f(\mathbf{Q}_{F1}) = 2.648 \times 0.5697 \times 1.247 = 1.881, \tag{A.45}$$
$$f(\mathbf{Q}_{F2}) = 3.202 \times 0.5697 \times 1.405 = 2.563, \tag{A.46}$$
$$f(\mathbf{Q}_{F3}) = 4.889 \times 0.5697 \times 1.324 = 3.688, \tag{A.47}$$
$$f(\mathbf{Q}_{F4}) = 5.448 \times 0.5697 \times 1.324 = 4.109. \tag{A.48}$$

The intensities obtained are:

$$I(\mathbf{Q}_{F1}) = 1.588 \times 1.881 = 2.987, \tag{A.49}$$
$$I(\mathbf{Q}_{F2}) = 1.169 \times 2.563 = 2.996, \tag{A.50}$$
$$I(\mathbf{Q}_{F3}) = 0.7966 \times 3.6877 = 2.938, \tag{A.51}$$
$$I(\mathbf{Q}_{F4}) = 0.6516 \times 4.109 = 2.677. \tag{A.52}$$

Since the $\mathbf{Q}_N$ intensity was obtained with a longitudinal scan, only the longitudinal scans of $\mathbf{Q}_{F1}$ and $\mathbf{Q}_{F2}$ can be compared to the $\mathbf{Q}_N$ reflection. $I_{\text{total}} = 2.987 + 2.996 = 5.983$.

Conclusion

The total intensity of the $\mathbf{Q}_{\mathrm{F}}$ phase would be 5.983 if the reflection were situated at the position of the $\mathbf{Q}_{\mathrm{N}}$ reflection. The first part of the experiment (up to B = 1.8 T) was performed at Risø, Denmark, and the rest of the phase diagram was established at Hahn-Meitner-Institut, Germany. The difference in the intensity of the $\mathbf{Q}_{\mathrm{N}}$ reflection at 1.8 T was a factor of 3.5916 to be multiplied to the Risø experiments. In total, the zero field intensity of the $\mathbf{Q}_{\mathrm{F}}$ phase is scaled from 1.588 to $5.983 \cdot 3.5916 = 21.5$, which can be seen in figure 30 on page 58.

Bibliographic Data Sheet **Risø-R-1440(EN)**

Title and authors

Neutron diffraction studies of magnetic ordering in superconducting $ErNi_2B_2C$ and $TmNi_2B_2C$ in an applied magnetic field

Katrine Nørgaard Toft

ISBN	ISSN
87-550-3286-9; 87-550-3287-7 (Internet)	0106-2840

Department or group	Date
Materials Research Department	5/1-2004

Groups own reg. number(s)	Project/contract No(s)

Sponsorship

Pages	Tables	Illustrations	References
106	4	46	59

Abstract (max. 2000 characters)

The field-induced magnetic structures of $ErNi_2B_2C$ and $TmNi_2B_2C$ in are especially interesting because the field suppresses the superconducting order parameter and therefore the magnetic properties can be studied while varying the strength of superconductivity.
$ErNi_2B_2C$: For magnetic fields along all three symmetry directions, the observed magnetic structures have a period corresponding to the Fermi surface nesting structure. The phase diagrams present all the observed magnetic structures. Two results remain unresolved: 1. When applying the magnetic field along [010], the minority domain ($\mathbf{Q_N}^{\mathbf{B}}$ = (0,Q,0) with moments perpendicular to the field) shows no signs of hysteresis. I expected it to be a meta-stable state, which would be gradually suppressed by a magnetic field, and when decreasing the field it would not reappear until some small field of approximately 0.1 T. 2. When the field is applied along [110], the magnetic structure rotates a small angle of 0.5 degrees away from the symmetry direction.
$TmNi_2B_2C$: A magnetic field applied in the [100] direction suppresses the zero field magnetic structure $\mathbf{Q_F}$ = (0.094,0.094,0) (T_N = 1.6 K), in favor of the Fermi surface nesting structure $\mathbf{Q_N}$ = (0.483,0,0). The appearance of the $\mathbf{Q_N}$ phase was initially believed to be caused by the suppression of superconductivity. This suppression should make it favorable to create a magnetic order with a Q-vector determined by the maximum in the magnetic susceptibility at the Fermi surface nesting vector $\mathbf{Q_N}$. The phase diagram for the magnetic structures is presented, however several properties of the $\mathbf{Q_N}$ magnetic structure cannot be explained within any known models. Quadrupolar ordering is suggested as a possible candidate for explaining these features of the $\mathbf{Q_N}$ structure.

Descriptors INIS/EDB

Boron Carbides; Erbium compounds; Magnetic fields; Magnetism; Neutron diffraction; Nickel compounds; Superconductors; Thulium compounds